Defining mechanisms of microvilli biogenesis using direct visualization

By

Isabella Marie Gaeta

Dissertation

Submitted to the Faculty of the

Graduate School of Vanderbilt University

in partial fulfillment of the requirements

for the degree of

DOCTOR OF PHILOSOPHY

in

Cell and Developmental Biology

May 12th 2023

Nashville, TN

Alissa M. Weaver, MD, Ph.D.

Robert J. Coffey, MD

Cynthia A. Reinhart-King, Ph.D.

Jason A. MacGurn, Ph.D.

Matthew J. Tyska, Ph.D

DEDICATION

For all those who dream of continued education

ACKNOWLEDGEMENTS

I would first like to acknowledge my mentor, Dr. Matthew Tyska, for his sound guidance, incredibly abundant patience, and truly infectious enthusiasm for cell biology. Through the inevitable ups and downs of graduate school, Matt has taught me to maintain a sense of calm, working against my innate inclination for panic in stressful situations. Matt displays unwavering support for his students and has advocated for and encouraged me every step of the way. I have eagerly taken notes throughout my graduate career to one day emulate his gracious and rigorous leadership style.

I would also like to thank all my lab mates, past (Meagan, Meredith, Leslie, Julia, Bo, and Colbie) and present (Rocio, Julissa, Angelo, Suli, Kianna, Jen, Gill, Olivia, Caroline, Deanna, and Aaron) who set the standard for rigorous science, aesthetically beautiful data presentation, and being overall wonderful co-workers. You have made the day-to-day graduate school experience so enjoyable and have been incredible pillars of support and encouragement.

In addition to the excellent training I have received at Vanderbilt, I would like to acknowledge my first laboratory mentor, Dr. Joel Swanson, at the University of Michigan Medical School, as well as all the amazing Swanson lab members who first taught me how to perform bench science. My experience in the Swanson lab opened my eyes to the exciting world of research, sparked my love for visualizing cells through live cell microscopy, and made me feel like I belonged in the laboratory. I truly feel that first

summer in the lab changed the trajectory of my life and career goals, opening incredible opportunities for learning, meeting new people, and ultimately leading me to pursue graduate training.

I have been exceptionally lucky to have friends from many walks of life, from my early days in grade school through graduate school. These friendships have enriched my life in so many ways. To my friends Alyssa, Emily, and Margaret, who I have known since my days at St. Francis, aside from all the laughs we have had, I always cherish our contemplative conversations, dreaming of our future lives and wrestling with life's big questions. To my University friends Tara and Uma, your friendship brightened my world in college, and your support and pursuit of your amazing goals is inspiring. To Julia, who I met serendipitously at orientation and has been a light in my life ever since. To my friends from graduate school — my yoga and brunch crew Brenna and Jordan, long-lost college friend Danielle, dart buddy Jessica, IGPal turned bestie Veronica, always down to dance partner Caye, and to Gill, Catie, Adri and Ryan who adopted me into their friend group — thank you for being a part of my fondest memories during my time in graduate school.

Finally, I want to thank my incredibly supportive family. Mom and Dad, you provided me the freedom and encouragement to pursue my interests and instilled in me a drive to continue growing and improve myself every day. To my sister Gabby, who would have thought the kid who said her work was "good enough" would end up in graduate school

and not the A++ student? I also want to acknowledge my extended family; my aunts, uncles, and cousins who always check in on me. I love you all so much.

TABLE OF CONTENTS

LIST OF FIGURES

LIST OF ABBREVIATIONS

ADP	adenosine diphosphate
APC	adenomatous polyposis coli
ATP	adenosine triphosphate
CL4	LLC-PK1-CL4 cells
COBL	cordon-bleu
CP	capping protein
EGFR	epidermal growth factor receptor
Ena	enabled
EPS8	epidermal growth factor pathway substrate 8
FH	formin homology
HPA	human protein atlas
IRTKS	insulin receptor tyrosine kinase substrate
JMY	junction-mediating and regulatory-protein
KD	knockdown
KO	knockout
Lmod	leiomodin
Mena	mouse enabled
PH	pleckstrin homology
PI	phosphatidylinositol
PI(3,4,5)P3	phosphatidylinositol (3,4,5)-trisphosphate
PI(4,5)P2	phosphatidylinositol (4,5)-bisphosphate

PRR	proline-rich region
SD	standard deviation
SEM	scanning electron microscopy
SIM	structured illumination microscopy
TEM	transmission electron microscopy
UtrCH	utrophin calponin homology domain
VASP	vasodilator-stimulated protein
W4	Ls174T-W4 cells
WT	wild type
ZO-1	zonula occludins-1

CHAPTER I

INTRODUCTION

Cell morphology

As the fundamental unit of life, cells take on different shapes for survival, performance of specialized functions, and sensation of the environment. Indeed, diversity in cell morphology is apparent in all domains of life. For instance, bacteria display a range of morphologies, from spherical to rod and helical shaped, which help confer fitness advantages depending on the environmental context (Yang et al., 2016). Additionally, in multicellular eukaryotic organisms, individual cells have evolved to take on morphologies which enable specialized functions. For example, immune cells survey tissues through crawling and forming extensions to uptake invading microbes and cellular debris (Fritz-Laylin et al., 2017). Neuronal cells take on long, branching morphologies, in some cases spanning nearly the entire length of an organism, allowing for the transport of electrochemical signals that enable long range nerve function (Allen et al., 1982). Another particularly striking example of specialized cell morphology is found in eukaryotic epithelial tissues. Forming the barrier between the outside and inside world, epithelial cells display a polarized morphology, organized in an apical-basolateral fashion. This unique morphology is typified by the presence of fingerlike protrusions that decorate the apical surface of the cell, called microvilli, which allow epithelial cells to perform absorptive and mechanosensory functions (Granger and Baker, 1950).

As cell shape is critical for proper cell function, aberrant morphologies can result in issues such as immunodeficiency, neurodegeneration, gastric disease, and even deafness. Thus, elucidating the molecular mechanisms that underlie normal cell morphology is crucial for understanding disease states in which it is compromised. At the fundamental level, cell morphology is dictated by the cytoskeleton and its associated proteins. Collectively, the cytoskeleton is comprised of three major components, the actin cytoskeleton, the microtubule cytoskeleton, and the intermediate filament network. This introduction will focus on the actin cytoskeleton and its role in the assembly of parallel actin-based protrusions. First, examples of parallel actin-based protrusions will be discussed. This will be followed by an overview of actin biochemistry and regulatory factors that promote the assembly of parallel actin-based protrusions, with special consideration given to proteins hypothesized to regulate actin filament elongation. The overarching goal of this introduction is to provide context for our studies in which we describe how cells both spatially and temporally organize molecules to promote microvillus growth, advancing our understanding of protrusion formation and apical morphogenesis.

Parallel actin-based protrusions

Parallel actin-based protrusions are morphological structures that are evolutionarily conserved through the eukaryotic lineage. It is thought that filopodia—generalized actin supported protrusions that extend from the cell periphery—evolved first, while apical surface protrusions such as microvilli and stereocilia evolved later in animal cells and choanoflagellates, and are thought to be a defining feature of animal

cell evolution (Sebe-Pedros et al., 2013). The key similarity between actin-based fingerlike protrusions is that they are supported by parallel bundles of actin filaments. This contrasts with the dense meshwork of branched actin filaments that make up the sheet-like lamellipodium and pseudopods at the leading edge of the cells (Fritz-Laylin et al., 2017). This difference in parallel versus branched network architecture holds implications for understanding molecular makeup and biogenesis of parallel actin-based protrusions. Additionally, electron microscopy has revealed that all three protrusions contain an electron dense plaque at their distal tips (Mooseker and Tilney, 1975a; Rzadzinska et al., 2004; Svitkina et al., 2003). This density is comprised of proteins believed to contribute to actin filament elongation. Thus, although some molecular details differ between filopodia, microvilli and stereocilia, it is hypothesized that their assemblies may follow similar general mechanisms of actin assembly, including filament nucleation, elongation, bundling, plasma membrane encapsulation and crosslinking. We will introduce three types of parallel actin-based protrusions, with later sections detailing specific molecular components.

Filopodia

Filopodia are actin bundle supported protrusions that are formed in a variety of cell types, allowing for cellular motility and sensation of the local environment. For instance, filopodia are found at the edge of crawling cells to enable migration, which has implications for both normal development and cancer metastasis (Arjonen et al., 2011). Additionally, filopodia are important for neuronal growth cone motility (Dent and Gertler,

2003). Filopodia are dynamic structures that grow and retract from the plasma membrane and can range in length from (~500 nm to 10 µm) (Svitkina et al., 2003).

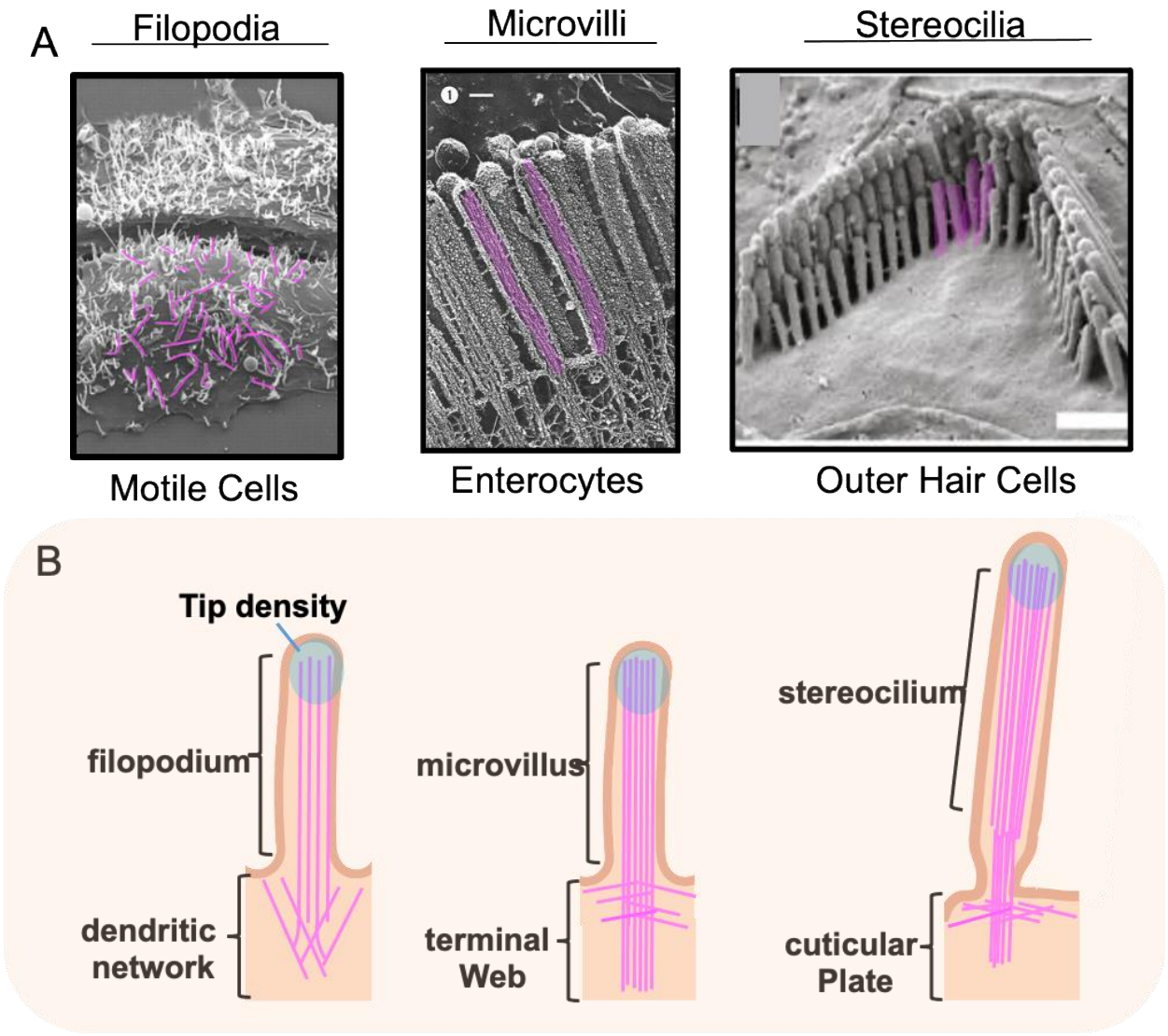

Figure 1-1. Types of parallel-actin based protrusions. (A) Scanning electron microscope images of cells displaying filopodia, microvilli and stereocilia (L-R). Protrusions are outlined in magenta. Images adapted from (Bohil et al., 2006; Hirokawa et al., 1982; McGrath et al., 2017). (B) cartoon schematics of actin organization (L-R) in filopodia, microvilli and stereocilia. Filopodia may be partially derived from the dendritic actin network, while microvilli and stereocilia are rooted in the terminal web and cuticular plate respectively. Schematic created using BioRender.

Notably, filopodia are supported by a core bundle of ~10-30 actin filaments, with addition of new actin monomers thought to produce the necessary force for membrane

deformation (Mogilner and Rubinstein, 2005; Peskin et al., 1993). For filopodia, two mechanisms of initiation have been proposed, known as the “convergent elongation” and “tip nucleation” models (Yang and Svitkina, 2011). Convergent elongation posits that filopodia actin filaments originate from the Arp2/3 nucleated dendritic network. During dendritic network formation, barbed ends are quickly capped by capping protein (CP). However, convergent elongation proposes that a subset of filaments become “privileged”, in that they are protected from capping protein by tip complex proteins such as ENA/VASP and formins, which promote filament elongation by protecting barbed ends from capping protein and incorporation new actin monomers (Svitkina et al., 2003). These privileged barbed ends then collide with one another at the leading edge, cluster together, and are subsequently bundled by fascin (Svitkina et al., 2003). The tip nucleation model states that filopodia are initiated by formins, which possess both nucleation and elongation activities (Yang and Svitkina, 2011). In this model, formins first cluster at the plasma membrane, leading to the nucleation and processive elongation of filaments. It should be noted that these models of filopodia initiation are not necessarily mutually exclusive and may explain multiple mechanisms of filopodia actin bundle assembly (Yang and Svitkina, 2011).

Microvilli

Microvilli are distinct from filopodia in that they are found at the apical surface of polarized epithelial cells. Though common to nearly all epithelial cells, perhaps the most striking and well-studied examples of microvilli are those found on the surface of the intestinal and renal proximal tubule epithelium. In the intestine, microvilli collectively

form the densely packed “brush border” which significantly increases the absorptive surface area and provides a mechanical barrier between microbes that inhabit the luminal space and the underlying tissues (Helander and Fandriks, 2014). The intestinal epithelium undergoes turnover every 3-5 days, with stem cells in the intestinal crypt repopulating the villus. As such, microvilli in the crypt are continuously undergoing growth and reorganization. These microvilli are highly disorganized and display considerable variations in length (unpublished data). This contrasts with microvilli on the surface of fully differentiated enterocytes which display remarkable uniformity, with ~2000 microvilli per cell, ranging from 1-3 µm in length depending on location in the intestine, with each protrusion containing 20-40 actin filaments per bundle (Mooseker and Tilney, 1975a; Ohta et al., 2012; Pinette et al., 2019). Actin bundles are rooted in the subapical terminal web region, supported by a network of myosin and intermediate filaments (Chinowsky et al., 2020; Hirokawa and Heuser, 1981). In the renal epithelium, cells do not continuously undergo turnover and differentiation. However, damaged renal brush borders can be regenerated within minutes (Chen et al., 1994). Studies outlined in this dissertation take advantage of both intestinal and kidney epithelial models, as they are highly amenable to genetic perturbations and live cell imaging.

Stereocilia

Stereocilia, which are considered “giant” or exaggerated microvilli, are displayed on the apical surface of sensory hair cells in the vertebrate ear. Stereocilia enable mechano-electrical transduction, a specialized process in which mechanical deflection of these protrusions is transmitted to electrical signals that result in hearing, balance, and spatial

orientation (Hudspeth, 1985). In contrast to microvilli, which display uniform lengths in fully differentiated tissues, stereocilia are organized in a graded staircase pattern (Tilney et al., 1992b). Moreover, while microvilli and filopodia contain tens of bundled filaments, stereocilia typically are supported by hundreds of actin bundles per protrusion, with up to 3000 bundles per protrusion in the most extreme examples (McGrath et al., 2017; Tilney et al., 1980). Interestingly, stereocilia are proposed to emerge from microvilli in developing hair cells, in a process whereby a fraction of microvilli grow into stereocilia and another fraction is resorbed (Tilney et al., 1992a). Stereocilia also differ from intestinal and renal microvilli in their stability. While the intestinal epithelium undergoes continuous turnover, fully differentiated hair cells remain for the lifespan of the organism, with little to no regeneration of damaged stereocilia (McGrath et al., 2017).

Actin cytoskeleton

Actin structure and assembly

Monomeric, or globular actin, (G-actin) is a 42 kDa ATP binding protein that assembles end to end into polarized filaments termed filamentous, or F-actin. Mammals encode six actin isoforms, four of which are primarily restricted to muscle and cardiac cells, while two cytoplasmic isoforms, β and γ, show widespread expression (Perrin and Ervasti, 2010). Indeed, β and γ actin are the predominant isoforms that make up intestinal microvilli and stereocilia (Bretscher and Weber, 1978; Perrin et al., 2010). Actin monomers are composed of two domains, α and β, folded into a globular structure, and further divided into four subdomains, S1-S4 (Dominguez and Holmes, 2011; Kabsch et al., 1990); with the ATP nucleotide and Mg^{2+} ion coordinated in the cleft between the α

and β domain fold (Dominguez and Holmes, 2011). To form protrusive structures, actin monomers are assembled into filaments, the polarity of which was initially revealed by myosin subfragment 1 labeling (Mooseker et al., 1982), establishing the nomenclature for the characteristic “barbed” and “pointed” ends. The barbed and pointed ends have unique kinetic properties under physiological conditions, which carry implications for understanding mechanisms for F-actin assembly. For F-actin to polymerize, three actin monomers must join to form a stable nucleus, which constitutes the “lag phase” of actin assembly (Figure 2-2). Once a stable trimer is formed, the filament will begin polymerizing by adding new subunits to the barbed end of the filament. Barbed end growth is more favorable under physiological conditions because the critical concentration—the concentration above which new monomers will be incorporated into the filament— is lower than the pointed end (0.12 µM for ATP-actin at the barbed vs 0.6 µM for ATP actin for pointed end growth) (Pollard, 1986). Once incorporated into the filament, ATP-actin is hydrolyzed to ADP + pi, over a half time of 2 seconds, with the release of inorganic phosphate occurring on the order of minutes (Korn et al., 1987). At steady state, the rate of addition of actin monomers to the barbed end

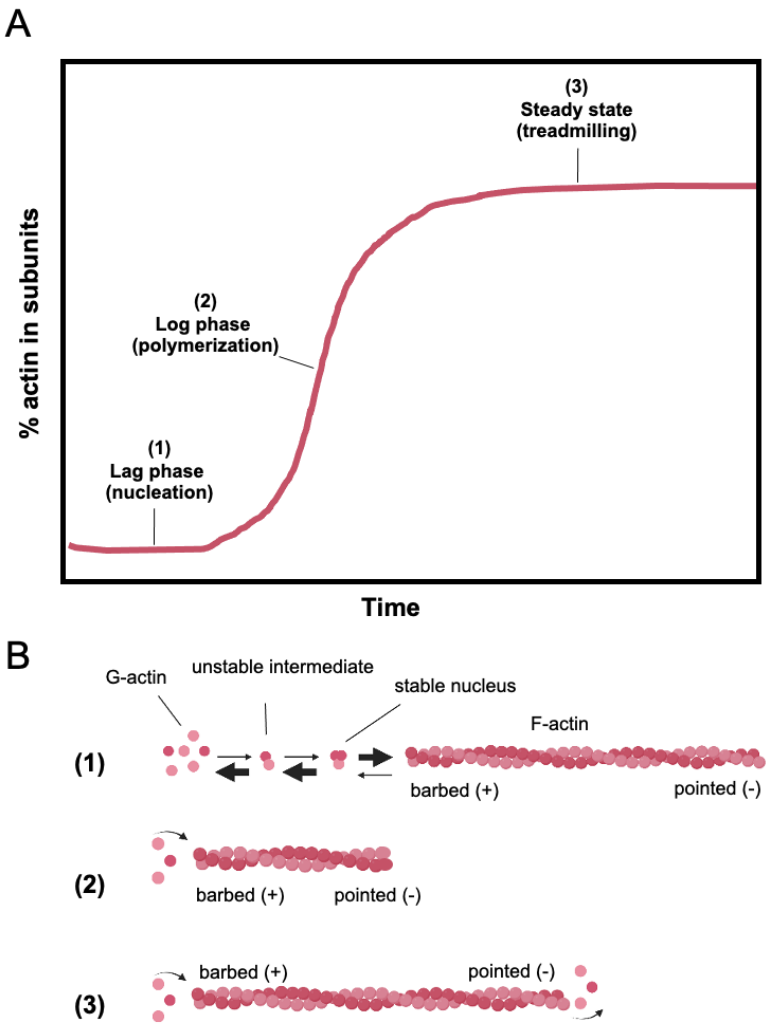

Figure 1-2. Stages of actin assembly. (A) Graph of actin assembly over time under physiological salt conditions, highlighting three main stages of assembly: 1) lag phase in which nucleation takes place, 2) log phase in which the filament grows primarily at its barbed end and 3) steady state treadmilling in which actin monomers are added to the barbed ends and removed at the pointed ends at comparable rates. (B) schematic representation of the three stages highlighted above. Figure Adapted from (Bruce Alberts, 2002); MOLECULAR BIOLOGY OF THE CELL, FOURTH EDITION by Bruce Alberts, et al. Copyright © 2002 by Bruce Alberts, Alexander Johnson, Julian Lewis, Martin Raff, Keith Roberts, and Peter Walter. (c) 1983, 1989, 1994 by Bruce Alberts, Dennis Bray, Julian Lewis, Martin Raff, Keith Roberts, and James D. Watson. Used by permission of W. W. Norton & Company, Inc. Schematic created using BioRender.

is equivalent to the dissociation of monomers at the pointed end, resulting in a net flux of subunits through the filament, in a process known as “treadmilling” (Wegner, 1982). Treadmilling occurs when the concentration of monomeric actin is higher than the critical concentration of the barbed end, but lower than the critical concentration of the pointed end, and subsequently has consequences for the growth, motility, and maintenance of protrusive structures in cells and tissues. For instance, in parallel actin based protrusions like filopodia, microvilli and stereocilia, the barbed—or fast growing end of the actin filament—are oriented toward the distal tip of the protrusion, adjacent to the membrane. Thus, new monomers are incorporated primarily at the tip of the protrusion.

While actin polymerization can occur *in vitro* in the absence of other proteins (Pollard, 1984), cells enlist a variety of actin-associated proteins to regulate filament assembly spatially and temporally within the cell. These proteins can be broadly grouped into several functional categories, including monomer-binding, nucleating, elongating, capping, bundling, and crosslinking, with some proteins facilitating multiple functions. This introduction will provide an overview of the types of actin binding proteins their activities, and how these proteins are involved in the construction of parallel based actin protrusions such as filopodia, microvilli, and stereocilia.

Actin-associated assembly factors

Actin monomer-binding proteins

As actin concentrations in the cell are estimated in the range of ~150 μM (Pollard et al., 2000), much higher than the critical concentrations of both ends of the actin filament, one would suspect the entire pool of actin monomers would be assembled into filaments. However, this is not the case, as cells tightly regulate pools of G- and F-actin. To spatially regulate polymerization competent G-actin and prevent spontaneous polymerization, cells express the actin monomer-binding protein profilin. Profilin catalyzes nucleotide exchange from ADP to ATP actin (Goldschmidt-Clermont et al., 1992), and nucleation and polymerization promoting factors use profilin-actin as the substrate for new monomer incorporation (Ferron et al., 2007; Paul and Pollard, 2008).

Actin nucleating proteins

Arp2/3

As forming a stable actin trimer is an intrinsically slow, concentration dependent process, cells enlist proteins that catalyze nucleation of new actin filaments. Nucleating proteins are instrumental in creating the two modes of actin network organization, branched filament networks and linear filament networks. Branched filament network architecture is controlled by the Arp2/3 complex and its accessory nucleation promoting factors. The Arp2/3 complex is made up of seven total subunits, Arp2 and Arp3, as well as ARPC1, ARPC2, ARPC3, ARPC4 and ARPC5. The Arp2/3 complex nucleates actin filaments on the side of pre-existing actin filaments, creating a new filament at a characteristic 70º angle (Kelleher et al., 1995; Machesky et al., 1994; Mullins et al., 1998). These branched actin networks are involved in formation of structures such as the lamellipodium, and endocytic cups (Firat-Karalar and Welch, 2011).

Formins

In contrast to branched actin networks, linear actin networks are composed of bundles of unbranched, linear actin filaments, such as those found in filopodia, microvilli, and stereocilia. Two major classes of identified linear actin filament nucleators include formins and tandem-monomer-binding nucleators. Formins share the presence of formin homology 1 (FH1) and FH2 domains, which contribute both nucleation and elongation activity. Through dimerization the FH2 domain specifically contributes to actin filament nucleation, forming a ring structure that binds and associates with the barbed end of the actin filament, and is thought to stabilize spontaneously formed dimers and trimers (Chesarone et al., 2010). Formins have been found to promote the nucleation of linear networks in filopodia and the contractile ring, however there is little evidence that formins contribute to the nucleation of linear actin filaments in microvilli and stereocilia (Grega-Larson et al., 2015).

Tandem monomer-binding nucleators

In addition to nucleation of parallel actin bundles through FH2 domains, another class of actin nucleators has been described. Tandem monomer-binding nucleators most typically contain WASP Homology domain-2 (WH2) domains, including Cobl, Spire, Leiomodin (Lmod) and Junction-mediating and regulatory-protein (JMY). Alternatively, adenomatous polyposis coli (APC) potentially mediates nucleation through its basic domain (Okada et al., 2010). WH2 domains are G-actin binding domains typified by an alpha helical structure and the LKKV consensus motif which bind between subdomains 1 and 3 of actin monomers (Chereau et al., 2005; Dominguez, 2016). Cobl is the

proposed nucleator of microvilli actin bundles in Ls174T-W4 (W4) cells (Grega-Larson et al., 2015). However, loss of Cobl in mice and Jeg-3 cell lines does not result in a microvillus length defect (Beer et al., 2020; Wayt and Bretscher, 2014), suggesting separate nucleators or other functions of Cobl could be at play.

Distal tip-targeting proteins

ENA/VASP family proteins

To facilitate actin filament elongation, cells enlist factors to promote incorporation of actin monomers to the barbed ends. First identified in *Drosophila*, enabled (Ena) and its vertebrate related paralogs vasodilator-stimulated phosphoprotein (VASP), mouse Ena (Mena, or ENAH in humans), and Ena-Vasp-like (Evl) associate with actin rich structures such as stress fibers and focal adhesions, and target to the distal tips of filopodia (Faix and Rottner, 2022).

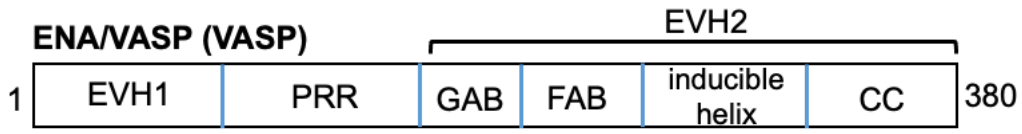

Figure 1-3. Domain diagram of the ENA/VASP protein VASP. EVH1 = ENA/VASP homology 1 domain. PRR = proline-rich region. The ENA/VASP homology 2 domain (EVH2) is composed of the GAB = G-actin binding region. FAB = F-actin binding region, inducible helix and coiled coil (CC) region.

ENA/VASP family proteins share N and C terminal Ena/Vasp homology domains 1 and 2 (EVH1, EVH2) and an intervening proline-rich sequence. In filopodia, the EVH1 domain mediates targeting to filopodial tips (Applewhite et al., 2007) while the EVH2 domain contains WH2 domain related modules that enable binding to both G and F-

actin (GAB and FAB modules, respectively) as well as a tetramerization domain (Bachmann et al., 1999). The EVH2 adjacent proline-rich domain is proposed to recruit profilin-actin, which then binds the GAB and leads to the incorporation of the actin monomer to filament barbed ends (Ferron et al., 2007). *In vitro* TIRF assays indicate VASP directly delivers monomers to filament barbed ends (Breitsprecher et al., 2008). In addition to direct delivery of monomers to filament ends, ENA/VASP proteins promote filament elongation by indirectly antagonizing capping protein (CP) (Barzik et al., 2005; Bear et al., 2002). Thus, protrusion elongation is thought to occur not only through direct addition of monomers, but also through protection of barbed ends from capping protein, which inhibits further polymerization.

Formins

In addition to their nucleation activity, formins also contribute to the elongation of parallel actin filaments by direct addition of actin monomers to barbed ends. After initial filament nucleation, formins processively associate with the barbed ends of actin filaments in an FH2 domain dependent manner (Goode and Eck, 2007). Direct addition of actin monomers is enabled by FH1 domains, which bind polymerization competent profilin-actin, and deliver these monomers to the barbed ends.

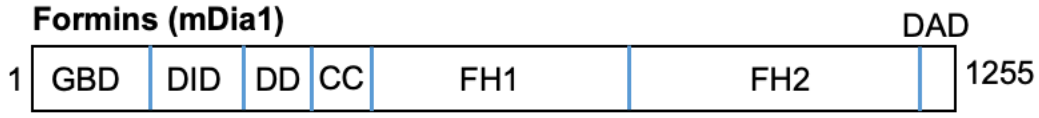

Figure 1-4. Domain diagram of the formin mDia1. GBD = GTPase binding domain. DID = diaphanous inhibitory domain. DD = dimerization domain. CC = coiled coil region. FH 1 = formin homology 1 domain. FH2 = formin homology 2 domain. DAD = diaphanous autoregulatory domain.

Additionally, formins have been shown to significantly increase the rate of actin filament polymerization up to 15x compared to the rate limited by diffusion (Kovar et al., 2006; Romero et al., 2004). Formins have been implicated in the elongation of actin filaments in structures such as the cytokinetic ring, stress fibers and filopodia (Goode and Eck, 2007). Indeed, formins have been shown to processively localize to the tips of filopodia, with their knockdown associated with reduced filopodia formation (Yang et al., 2007). Interestingly, formin dependent polymerization has not been described in microvilli or stereocilia. Pan formin inhibition by small molecular inhibitor SMIFH2 was shown to have no effect on brush border formation in polarized epithelial cells (Grega-Larson et al., 2015). However, this finding should be further investigated as recent studies demonstrated an off target inhibitory effect of SMIFH2 on non-muscle myosin II (NM2) (Nishimura et al., 2021). As inhibition of NM2 isoform NM2C has recently been shown to increase microvilli length (Chinowsky et al., 2020), the SMIFH2 off target inhibition of NM2C could be masking an effect on formin inhibition.

I-BAR domain containing proteins

Parallel actin-based protrusions are formed by deformation of the plasma membrane which in turn encapsulate the underlying actin bundle. The distal tip of parallel actin-based protrusions displays outward, or negative, plasma membrane curvature, which is sensed by Inverse-Bin/Amphiphysin/RVS (I-BAR) domain containing proteins. I-BAR domains are organized in dimerized alpha helices (Lee et al., 2007; Millard et al., 2005), which bind electrostatically to the plasma membrane through positively charged residues (Frost et al., 2009). Several I-BAR domain containing proteins have been identified, including insulin receptor tyrosine kinase substate p53 (IRSP53, also known

as BAIAP2), missing in metastasis (MIM), actin bundling protein with BAIAP2 homology (ABBA), insulin receptor tyrosine kinase (IRTKS, also known as BAIAP2L1) and Pinkbar, (also known as BAIAP2L2). I-BAR domains have been demonstrated to cluster $PI(4,5)P_2$ at membranes as well as induce negative membrane curvature deformation, producing tubular like structures *in vitro* (Mattila et al., 2007; Saarikangas et al., 2009). Specifically, IRPSP53, IRTKS and Pinkbar have been implicated at sites of negative membrane curvature in parallel based actin protrusions.

Figure 1-5. Domain diagram of the IBAR-protein IRTKS. I-BAR = inverse BAR domain. SH3 = src Homology 3 domain. WH2 = WASP homology 2 domain.

These I-BAR proteins share other common domain features including the actin binding WH2 domains that allow linking of the plasma membrane to the underlying actin bundle, as well as SH3 domains that mediate protein-protein interactions (Zhao et al., 2011). IRSP53 is involved in filopodia formation and dendritic spine morphogenesis. During filopodia formation, IRSP53 associates with Cdc42 and EPS8, with binding mediated through its CRIB domain SH3 domain respectively (Disanza et al., 2006). IRTKS was identified as a potential microvillus associated I-BAR protein (McConnell et al., 2011b) with subsequent studies demonstrating IRTKS targets to the distal tips of microvilli and promotes protrusion elongation and directed motility in a WH2 dependent manner (Postema et al., 2018a). The ability of IRTKS to elongate microvilli was also partially dependent on the EPS8, which interacts with the SH3 domain of IRTKS (Postema et al., 2018a). As IRTKS promotes elongation, it has been hypothesized that IRTKS is one of the early factors present at sites of microvilli biogenesis, which will be further explored in

later chapters of this dissertation. Preliminary characterization of IRTKS knockout mice by SEM and TEM did not reveal a dramatic effect on microvillus morphology (unpublished data; Tyska lab). Although this tissue needs to be more thoroughly characterized, lack of an obvious phenotype may be due to compensation by other I-BAR proteins. Moreover, Pinkbar has been shown to target to the distal tips of the two shortest stereocilia rows, with its targeting likely dependent on MYO15A and EPS8, as Pinkbar does not localize to stereocilia tips in MYO15A and EPS8 deficient mice (Carlton et al., 2021). These Pinkbar knockout mice eventually lose their third row stereocilia and exhibit progressive hearing loss. As stereocilia are initially able to grow normally, this suggests Pinkbar is necessary for maintenance of the actin bundle and not growth. However, it is possible that other I-BAR proteins such as IRTKS compensates for Pinkbar at the initial stages of stereocilia morphogenesis, but this question remains to be experimentally tested (Carlton et al., 2021).

Capping Protein

In contrast to proteins that promote elongation of actin filaments, barbed end capping proteins prevent incorporation of new monomers. The most well studied and ubiquitous example is capping protein (CP), which binds to the barbed ends of actin filaments with 1:1 stoichiometry at sub-nanomolar affinity (Wear et al., 2003). CP is a heterodimer composed of α- and β-subunits, and associates with barbed ends through electrostatic and hydrophobic interactions (Yamashita et al., 2003). Specifically, CP binds to an acidic patch between the two terminal barbed end subunits of the filament, as well as the hydrophobic cleft of the most terminal subunit (Edwards et al., 2014). Although CP

effectively shuts down addition of new actin monomers to the barbed ends, loss of capping protein decreases cell motility and dendritic network formation and is an essential component in the reconstitution of actin-based motility on functionalized beads, along with Arp2/3, profilin and ADF/cofilin (Akin and Mullins, 2008; Hug et al., 1995; Vignjevic et al., 2003). These observations stand in contrast to the predicted loss of function phenotype, whereby inhibition of capping protein would lead to uncontrolled filament elongation. Two hypothesis have been proposed to explain the promotion of dendritic network formation by capping protein: the funneling hypothesis and monomer-gating hypothesis. The funneling hypothesis states that capping protein caps fast growing barbed ends, effectively increasing the local concentration of actin monomers, and thus "funneling" these monomers to uncapped barbed ends, driving faster polymerization (Carlier and Pantaloni, 1997). The monomer-gating hypothesis was proposed in direct response, after *in vitro* bead motility assays indicated increasing concentrations of capping protein is not associated with increasing actin monomer concentration, free barbed ends or the rate of polymerization (Akin and Mullins, 2008). This hypothesis posits that free barbed ends are in competition with the Arp2/3 complex for addition of new monomers, namely by WH2 domain containing proteins. Barbed end capping is thereby proposed to promote nucleation by the Arp2/3 complex, creating a more branched network architecture.

For the formation of parallel actin-based protrusions, studies show inhibiting capping protein does promote filopodia elongation (Mejillano et al., 2004), and that several elongation factors promote addition of new actin monomers by indirectly inhibiting CP

(Edwards et al., 2014). While barbed ends must indeed be uncapped for new actin monomer to incorporate, this does not necessarily preclude capping protein from functioning in the formation of parallel actin-based protrusions. Further investigation demonstrated that knockdown of capping protein does increase the overall density of filopodia and F-actin concentration, although filopodia were shorter on average (Mejillano et al., 2004; Sinnar et al., 2014). These filopodia showed decreased rates of protrusion, and a greater fraction of time in a "paused" state (Sinnar et al., 2014) indicating capping protein plays a role in regulating normal filopodial dynamics. Studies in a hair cell specific CP mouse knockout model showed that stereocilia initially grow normally, but are eventually lost over the course of development (Avenarius et al., 2017). This loss is typified by concomitant narrowing and shortening of the stereocilia, suggesting CP plays a role in stabilizing actin filaments during the widening of stereocilia. Studies of CP function in microvilli formation are limited; CP has been shown to be present in microvilli fractions using bulk methods (McConnell et al., 2011b; Schafer et al., 1992), however localization of CP by immunofluorescence and expression of tagged constructs has been difficult to reproduce (unpublished data and personal communications). Thus, although CP functions to effectively halt actin filament elongation, it plays important roles in regulating protrusion formation and morphology.

EPS8

Another protein with proposed roles in filament capping and bundling is epidermal growth factor pathway substrate 8 (EPS8). As its name suggests, EPS8 was first identified as a downstream effector of epidermal growth factor receptor (EGFR) (Fazioli et al., 1993). In addition to its direct binding to EGFR, subsequent studies identified

EPS8 as an actin binding protein with implications for intestinal morphogenesis (Castagnino et al., 1995; Croce et al., 2004). Additionally, three EPS8-like proteins have since been identified, EPS8L1, EPS8L2 and EPS8L3, which share 27-42% sequence identity to EPS8 (Offenhauser et al., 2004).

Figure 1-6. Domain diagram of EPS8. PTB = phosphotyrosine binding domain, PRR = proline-rich region, SH3 domain, AB = actin binding effector region.

EPS8 is perhaps the best studied member of its family proteins and is a 97 kDa protein comprised of a phosphotyrosine binding domain (PTB, previous studies have also annotated this feature as a split PH domain (Maa et al., 2001)) proline-rich regions, a Src-homology 3 (SH3) domain, and a c-terminal effector region (Kishan et al., 1997; Scita et al., 2001). The PTB domain of EPS8 shows sequence similarity to the dab-like PTB family proteins (Uhlik et al., 2005), which have been shown to bind PI(4,5)P2. Although EPS8 has not been directly implicated in lipid binding, this domain structure suggests it could have membrane binding potential. SH3 domains are a common mode of protein-protein interaction, which interact directly with proline-rich PXXP motif (Kurochkina and Guha, 2013). The EPS8 SH3 domain has been shown to bind non-canonical PXXDY motifs in proteins including RN-tre and Abi1 (Biesova et al., 1997; Matoskova et al., 1996; Mongiovi et al., 1999). Additionally, the SH3 domain of EPS8 has been shown to mediate its dimerization (Kishan et al., 1997).

The c-terminal effector region of EPS8 has been shown to interact directly with both G and F-actin *in vitro* and experiments have suggested this region contains barbed end capping and actin bundling activity (Disanza et al., 2004; Hertzog et al., 2010; Scita et al., 2001). In terms of capping activity, the isolated c-terminal region (AAs 648-822) binds the barbed ends of actin filaments with ~15 nM affinity (Disanza et al., 2004). However, full length EPS8 is not able to cap barbed ends, suggesting autoinhibition *in vitro* (Disanza et al., 2004). Additionally, the isolated c-terminal region was effective in reconstituting motility in the absence of CP, suggesting the c-terminus of EPS8 can contribute capping activity needed to promote polymerization of actin filaments *in vitro* (Disanza et al., 2004; Hertzog et al., 2010). Furthermore, EPS8 binding to actin has been structurally modeled (Hertzog et al., 2010), with actin binding mediated by five amphipathic alpha helices (H1-H5). Specifically, capping is mediated by hydrophobic contacts in the H1 helix, which bind between subdomain 1 and subdomain 3 of the terminal barbed end actin monomer (Hertzog et al., 2010). Mutation of hydrophobic residues V689 and L693 to hydrophilic aspartic acid abrogated barbed end binding *in vitro* (Hertzog et al., 2010), as well as reconstitution of actin networks on bead motility assays. EPS8 bundling activity has been attributed to residues that reside in the globular H2-H5 helix (LNKDE 757-761), and is dependent on dimerization, with mutation of LNK757-759AAA abrogating bundling activity as assayed by actin co-sedimentation (Hertzog et al., 2010).

Actin-bundling proteins

As actin filaments elongate in fingerlike protrusions, they are crosslinked together, forming a core bundle of filaments. This crosslinking is facilitated by actin bundling

proteins, which bind along the length of F-actin, linking adjacent filaments to one another. Multiple actin-binding domains have been implicated in the bundling of filaments, with filament spacing dependent on crosslinker diameter (Castaneda et al., 2021). Filopodia are primarily bundled by fascin (Vignjevic et al., 2006), while microvilli are bundled by villin (VIL), plastin-1 (PLS-1, also known as fimbrin) espin (ESPN) and MISP (Bartles et al., 1998; Bretscher and Weber, 1979a; Bretscher and Weber, 1980; Morales et al., 2022) . Additionally, stereocilia are bundled by fascin, PLS-1, ESPN and XIRP2 (Francis et al., 2015; Roy and Perrin, 2018; Sekerkova et al., 2011; Taylor et al., 2015). Microvilli specific actin bundling proteins diverse domain architectures, with actin-binding mediated by gelsolin like domains (VIL), calponin homology (CH) domains (fimbrin), and an actin bundling motif (ESPN) (Crawley et al., 2014a). MISP is a largely disordered protein, and specific motifs that mediate its bundling activity have not yet been described (Morales et al., 2022). These proteins also display distinct spatial localization along microvilli actin bundles, with ESPN localizing along nearly the entire length of the bundle, VIL localizing along the upper 2/3rds of the bundle, and PLS-1 and MISP restricted to the rootlet ends (Crawley et al., 2014a; Morales et al., 2022).

Membrane-cytoskeleton linkers

Ezrin

Not only are filaments crosslinked to one another, but core actin bundles are physically linked to the overlying plasma membrane. In microvilli, these interactions are facilitated by the ezrin-radixin-moesin (ERM) protein ezrin, along with Myosin 1a and Myosin 6. First identified in microvilli, ezrin is a 80 kDa protein that contains a 4.1-ezrin-radixinn-moesin (FERM) domain, which enables lipid-protein interactions, an alpha helical

domain, and C-terminal domain (CTD) which facilitates actin-binding (Algrain et al., 1993; Bretscher, 1983; Li et al., 2007; Pearson et al., 2000; Turunen et al., 1994). Ezrin takes on an auto inhibited conformation until it is activated by phosphorylation and $PI(4,5)P_2$ at the apical plasma membrane. Binding of ERM proteins to $PI(4,5)P_2$ induces a conformational change that allows the CTD to bind actin, with phosphorylation inhibiting folding into the inactive state (Fievet et al., 2004). Ezrin knockout in mice results in shortened microvilli (Saotome et al., 2004), and inhibition of phosphocycling results in microvillus loss (Viswanatha et al., 2012).

Myosin-1a

Myosin-1a is a single headed, class I myosin that demonstrates restricted expression to the intestinal tract and is the most abundant class I myosin in the brush border (McConnell et al., 2011b; Skowron et al., 1998; Skowron and Mooseker, 1999). Myosin-1a mediates actin-binding through its motor domain, and peripherally interacts with the membrane using its tail homology 1 (TH1) domain (Hayden et al., 1990; Mazerik and Tyska, 2012). Examination of intestinal brush borders in mice lacking myosin-1a reveals extensive membrane undulations and loss of characteristic lateral bridges observed by TEM compared to wildtype mice (Tyska et al., 2005), suggesting that Myosin 1-a functions to crosslink the plasma membrane to the underlying actin core.

Myosin-6

In addition to myosin 1-a, myosin-6 is another motor protein that mediates membrane-cytoskeleton linking in the brush border. Myosin-6 is the only minus-end directed

myosin, which is congruent with its localization to the terminal web region of the intestinal brush border (Hegan et al., 2012; Wells et al., 1999). There, myosin-6 is implicated in endocytosis, which occurs at basal inter-microvilli plasma membrane sites (Ameen and Apodaca, 2007). Myosin-6 null mice exhibit lifting of plasma membrane from the cytoskeleton at these sites, implicating its function in membrane-cytoskeleton linking, (Hegan et al., 2012). The exact mechanism of myosin-6 membrane cytoskeleton linking is unclear however, as sequence features that mediate direct plasma membrane binding have not been identified (Crawley et al., 2014a).

Distal tip complex

As alluded to above, previous studies identified several factors that are enriched at the distal tips and may reside in the electron dense complex. This complex is of particular interest to the study of protrusion biogenesis, as it embeds the barbed ends of actin filaments – the active site of new monomer addition – and is therefore thought to regulate filament growth (Figure 1-7).

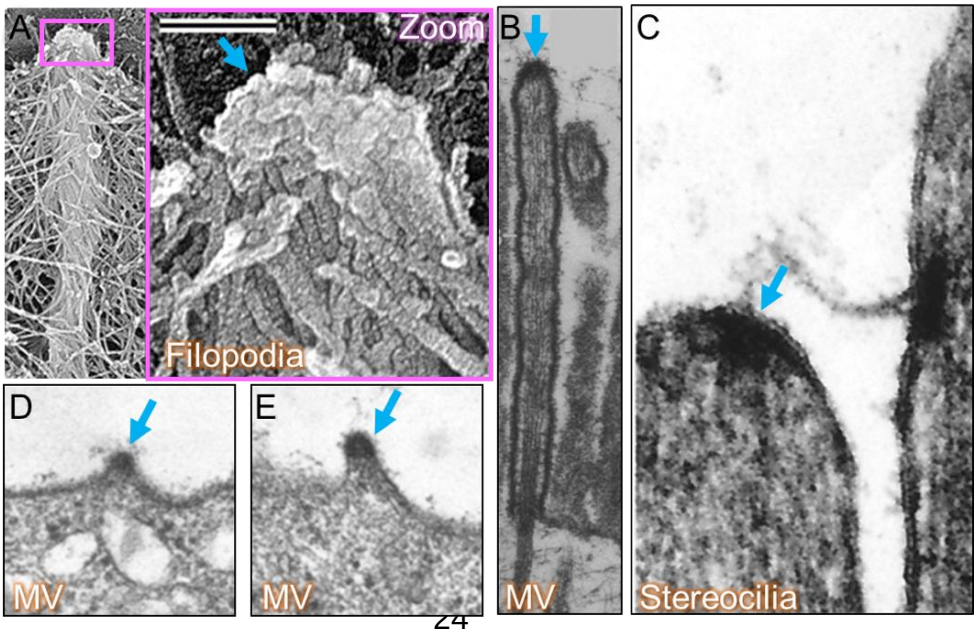

Figure 1-7. Electron micrographs of distal tip complexes. in A) Filopodia, pink box denotes zoom; B) mature intestinal microvilli C) hair cell stereocilia, D & E) nascent microvilli that have undergone re-growth. Arrows highlight distal tip complexes. Images adapted from (Kachar et al., 2000; Mooseker and Tilney, 1975a; Svitkina et al., 2003; Tilney and Cardell, 1970).

There is a great deal of evidence that indicates myosin motors and tip-linking adhesion complexes function in the organization of finger-like surface features. These factors are essential for cargo transport, maintenance, and structural stability of protrusions. For instance, MYO10 is enriched at filopodial tips (Berg and Cheney, 2002), whereas MYO15 (Belyantseva et al., 2003), MYO3A (Salles et al., 2009) and MYO7A (Grati and Kachar, 2011) accumulate at stereocilia tips and the upper tip link densities, and MYO7B exhibits robust tip targeting in microvilli (Weck et al., 2016). In both stereocilia and microvilli, transmembrane adhesion molecules are delivered to the tip compartment by these unconventional myosins, to form tip-linking complexes that physically connect adjacent protrusions. In stereocilia, CDH23 and PCDH15 form *trans* heterophilic adhesion complexes (Kazmierczak et al., 2007), whereas microvilli are linked by a complex composed of CDHR2 and CHDR5 (Crawley et al., 2014a).

Additionally, other distal tip targeting proteins, as discussed in the above sections, directly bind actin filament barbed ends and are thus positioned to control filament length and subsequently the growth of protrusions. In filopodia, molecules that promote barbed end elongation include ENA/VASP family proteins and formins, which likely function by antagonizing Capping Protein and/or by promoting direct addition of new

profilin-actin monomers to filament barbed-ends (Bear et al., 2002; Breitsprecher and Goode, 2013; Ferron et al., 2007). In stereocilia, a tip enriched complex containing WHIRLIN, EPS8, and MYO15A promote elongation (Manor et al., 2011b). Additionally, the barbed end binder CP drives widening of stereocilia, and this function may be aided by its interaction with TWINFILIN-2 (Avenarius et al., 2017). The EPS8 family member EPS8L2 is also enriched at the distal tips of stereocilia, and loss of this protein affects stereocilia length and results in gradual deafness (Furness et al., 2013). In microvilli, tip enriched actin-binding proteins EPS8 and the I-BAR protein IRTKS promote protrusion elongation (Postema et al., 2018a). Additionally, EPS8L1a localizes to the distal tips of microvilli and interacts with EZRIN, and co-expression of EZRIN with either EPS8L1a or EPS8 disrupts microvillus morphology (Zwaenepoel et al., 2012). These barbed end binding proteins are of interest when considering protrusion biogenesis at its earliest stages – the moments after actin nucleus formation – when the filament begins to elongate, and will be explored further in subsequent chapters.

Summary

Parallel actin-based protrusions are morphological features that enable a range of cellular activities including motility, nutrient absorption, and mechanosensation. Thus, studying how protrusions assemble at the molecular level contributes to our understanding of disease states in which proper cell morphology is compromised. The studies outlined in this dissertation focus on the biogenesis of microvilli and are the first to characterize the growth of these protrusions with molecular and temporal detail. Knowledge of microvillus ultrastructure greatly informed our investigation – particularly the distal tip complex – which has long been hypothesized to promote microvillus

growth due to its association with the barbed ends of actin filaments (Mooseker and Tilney, 1975a). We thus begin our characterization of microvilli biogenesis through the study of EPS8, which has been shown to target specifically to the distal tips of microvilli and is implicated in protrusion elongation. We show that EPS8 marks sites of microvillus growth in punctate, diffraction-limited spots and that mutations in the actin-binding region affect puncta formation and protrusion elongation. Moreover, we propose a framework for microvilli biogenesis in that growth occurs through two general mechanisms: *de novo* growth, in which microvilli F-actin bundles emerge spontaneously at the cell surface, and "daughter growth" whereby microvilli grow from pre-existing protrusions. In addition to growth of these structures, we find that microvilli also undergo collapse, whereby the nascent bundle loses membrane wrapping and depolymerizes. We implicate other known resident microvilli proteins in the growth process, including IRTKS and Ezrin, allowing us to build a temporal framework of protein recruitment during microvilli biogenesis. Thus, we hope future work will build on this established framework, such as understanding the role of the proposed microvilli nucleator COBL and its binding partner PACSIN-2 during microvilli biogenesis as well as lipid and small GTPase signaling during this process.

We further build upon our characterization of microvilli biogenesis by taking advantage of EPS8 – which we established marks early sites of growth and displays remarkable specificity to the distal tips of microvilli (Gaeta et al., 2021a) – as an anchor in a biotin proximity labeling assay to probe for new molecules involved in microvillus growth. Through these studies we identified a previously uncharacterized protein, KIAA1671 as

a new member of the apical brush border. Using a combination of live and fixed cell imaging, we find that KIAA1671 associates with actin positive structures, as well as EPS8 during both *de novo* and daughter microvillus growth. These studies emphasize the utility proximity labeling in combination with live cell imaging to gain new insights into protrusion biogenesis. Future studies should focus on the specific mechanisms of KIAA1671 function and further describe its nature of association with actin and EPS8. In all, the studies outlined in this dissertation establish a model for directly visualizing microvilli biogenesis and provide valuable insight into our molecular and temporal understanding of how microvilli are assembled at the apical cell surface.

CHAPTER II

MATERIALS AND METHODS

Cell culture

LLC-PK1-CL4 (porcine kidney proximal tubule) and OK (opossum kidney, ATCC CRL-1849) and B16F1 melanoma cells were cultured in DMEM with high glucose and 2 mM L-glutamine supplemented with 10% fetal bovine serum (FBS) and 1% glutamine. CACO-2_{BBE} cells (human colonic adenocarcinoma, ATCC CRL-2102) were cultured in DMEM with high glucose and 2 mM L-glutamine supplemented with 20% FBS and 1% glutamine. Ls174T-W4 cells (female human colon epithelial cells) were cultured in DMEM with high glucose and 2 mM L-glutamine supplemented with 10% tetracycline-free FBS, 1% glutamine, G-418 (1 mg/ml), blasticidin (10 µg/ml), and phleomycin (20 µg/ml). All cultures were maintained at 37°C with 5% CO_2.

Cloning and constructs

pLVX-mCherry-ESPN encoding a tagged form of human espin-2B was used for all experiments except in Figures 3-1 B-C and Figure 3-6 B, which instead used mCherry-ESPN encoding a tagged form of rat espin-2B. EGFP-EPS8, and EGFP-IRTKS were described previously (Meenderink et al., 2019; Postema et al., 2018b), whereas EZR-EGFP was a gift from Dr. Stephen Shaw (NIH)(Hao et al., 2009). The full length EGFP-EPS8 construct used for most experiments described herein contained two amino acid substitutions in the C-terminus (E818D and S820C) and made use of the stop codon in the plasmid backbone ~15 amino acids downstream of the native stop. All other EPS8 constructs are based on the sequence accession AAH30010.1 except for the indicated

mutations or truncations. EGFP-EPS8 1-648 (primers 5'→3' forward ATGAATGGTCATATTTCTAATCATCCC; 5'→3' reverse TTATGACACAGGAACAGGTGCTGG) and EGFP-EPS8 649-822 (primers 5'→3' forward AAGGTCCCAGCAAATATAACACGTCA; 5'→3' reverse TTAGTGACTGCTTCCTTCATCAAAAGATTCC) constructs were generated by PCR, topo-cloned into the pCR8 entry vector (Invitrogen), and then shuttled into a gateway adapted EGFP-C1-GW vector via the LR recombination reaction. Point mutagenesis was performed on a pCR8-EPS8 template, and then shuttled into EGFP-C1-GW vector to create EGFP-EPS8 V690D L694D (primers 5'→3' forward GAAATCTCAGATGGAGGAAGACCAAGATGAAGACATCCACAGACTGACCATTG; 5'→3' reverse CAATGGTCAGTCTGTGGATGTCTTCATCTTGGTCTTCCTCCATCTGAGATTTC) and EGFP-EPS8 LNK758-760AAA (primers 5'→3' forward GGTGCACAACTTTTCTCTGCCGCTGCGGATGAACTGAGGACAGTCTGCCC; 5'→3' reverse GGGCAGACTGTCCTCAGTTCATCCGCAGCGGCAGAGAAAAGTTGTGCACC). To create pLVX-mCherry-βactin, mCherry-βactin was generated by PCR using primers (5'→3' forward TAAGCAGAATTCGCCACCATGGTGAGCAAGG; 5'→3' reverse TAAGCAGGGCCCCTAGAAGCATTTGCGGTGGACGA) and ligated into the pLVX-puro backbone (Takara) after digestion of the backbone and insert with EcoRI and ApaI.

An empty vector pLVX-MCS-puro construct was created by digesting the pLVX-AcGFP vector (Takara) with NdeI and XhoI. The region of the CMV promoter that was cut

during this process was re-ligated, with the region amplified via PCR using primers 5'→3' forward CCCCCGCCCATTGACGTCAATAATGACG and 5'→3' reverse TAAGCACTCGAGGGTGGCGACCGGTAGAT creating the vector pLVX-MCS-puro. BioID2-HA and 13xLinker-BioID2-HA sequences were amplified via PCR flanked with XhoI and ApaI cut sites 5'→3' forward CCCCCGCCCATTGACGTCAATAATGACG and 5'→3' reverse TAAGCACTCGAGGGTGGCGACCGGTAGAT. These PCR products were digested and inserted into the pLVX-MCS-puro vector to create pLVX-MCS-BioID2 and pLVX-MCS-13xLinker-BioID2. The pLVX-myc-BioID2 vector was created via Gibson assembly, using PCR to amplify the insert sequence 5'→3' forward GGATCTACCGGTCGCCACCCAGACCCAAGCTGGCTAGC, 5'→3' reverse GATCCGGTGGATCCCGGGCCTCGAGGCTGATCAGCGGTTTAAAC and inserted into the pLVX-MCS-puro backbone digested with XhoI and ApaI using the Gibson assembly master mix (NEB). Full length human EPS8 was amplified via PCR using primers 5'→3' forward TAAGCACTCGAGGCCACCATGAATGGTCATATTTCTAATCATCC and 5'→3' reverse TAAGCAGAATTCGTGACTGCTTCCTTCATCAAAAGATTCC inserted into the pLVX-MCS-BioID2-HA and pLVX-MCS-13xLinker-BioID2-HA via restriction digest with XhoI and EcoRI. The EGFP-KIAA1671 plasmid was purchased from Genscript, encoding ORF clone accession number NM_001145206.1, tagged with GFP derivative GFP(S65T). pHalo-C1-KIAA1671 was generated using by PCR using primers 5'→3' forward ACCATGGCCACGCGG and 5'→3' reverse TCAAACTTGGTTCTCATAAAGACTTTGCCT, topo cloned into the pCR8 vector, and then shuttled into the pHalo-C1-GW vector. Full length human EPS8 was generated via PCR using primers 5'→3' forward ATGAATGGTCATATTTCTAATCATCCC and 5'→3'

reverse TTAGTGACTGCTTCCTTCATCAAAAGATTCC topo cloned into the EGFP-C1-GW vector. All constructs were verified by sequencing.

Stable cell line generation and transient transfection

Stable cell line generation: To create cells stably expressing two fluorescent proteins, LLC-PK1-CL4 were first transiently transfected with EGFP tagged constructs and subsequently selected with 1 mg/mL G418 for approximately two to four weeks (EGFP-EPS8, EGFP-IRTKS, EGFP-EPS8LNKAAA, EGFP-EPS8 V690D L694D, EGFP-KIAA1671). Cells were then transduced with lentivirus expressing pLVX-mCherry-ESPN or pLVX-mCherry-β-actin to make the double stable cell line. Lentivirus was generated using either HEK293T or HEK293FT cells co-transfected with pLVX-mCherry-ESPN or pLVX-mCherry- β-actin, and psPAX2 and pMD2.G using Lipofectamine2000 (ThermoFisher), according to the manufacturer's instructions. Media was changed 16 hrs after transfection, and virus was collected 72 and 96 hrs after transfection and concentrated using Lenti-X concentrator (Clontech). Cells were then transduced with virus after growing to 75% confluency and supplemented with 10 µg/mL polybrene. Media was changed one day after transduction and cells were placed under selection with puromycin (10 µg/mL concentration) 72 hrs after transduction. Established double stable cell lines were maintained in 1 mg/mL G418 and 10 µg/mL concentration puromycin. Cells expressing mCherry-ESPN were used previously (Meenderink et al., 2019) and were created by transient transfection with pmCherry-ESPN selected with 1 mg/mL G418, sorted, and maintained in selection with 1 mg/mL G418.

To create W4 BioID2 and stable cells, target cells were transduced with lentivirus expressing pLVX-EPS8-BioID2-HA, pLVX-EPS8-13xLinker-BioID2-HA, or pLVX-myc-BioID2. Lentivirus was generated using HEK293FT cells co-transfected with pLVX-EPS8-BioID2-HA, pLVX-EPS8-13xLinker-BioID2-HA, pLVX-myc-BioID2, or pLVX-mCherry-ESPN and psPAX2 and pMD2.G using Lipofectamine2000 (ThermoFisher), according to the manufacturer's instructions. Media was changed 16 hrs after transfection, and virus was collected 72 and 96 hrs after transfection and concentrated using Lenti-X concentrator (Clontech). Cells were then transduced with virus after growing to 75% confluency and supplemented with 10 µg/mL polybrene. Media was changed one day after transduction and cells were placed under selection with puromycin (10 µg/mL concentration) 72 hrs after transduction.

Transient transfection: W4 cells were seeded in 6 well plates and transfected at ~60% confluency, using Lipofectamine2000 according to manufacturer's instructions. The following day, cells were re-plated on acid-washed glass coverslips and induced to form brush borders using 1 µg/ml doxycycline for 16 hr before fixation.

B16F1 melanoma cells were transiently transfected with EGFP-KIAA1671 and mCherry-UtrCH using Lipofectamine2000 according to the manufacturer's instructions. The next day, cells were plated onto plasma cleaned 35 mm glass bottom dishes coated with 50 µg/mL laminin, allowed to adhere for at least 3 hr, and then imaged. CL4 cells stably expressing EGFP-EPS8 and mCherry-ESPN with were transiently transfected with Halo-KIAA1671 using Lipofectamine 2000 according to the manufacturer's instructions. After 4 hr, cells were plated onto plasma cleaned 35 mm glass bottom dishes (Cellvis,

D35-20-1.5-N) and imaged the following day at subconfluency. For labeling of Halo tagged constructs, cells were incubated for 1 hr in JFX-646 dye (Janelia Farms, diluted 1:1000 in CL4 media). Briefly rinsed with PBS and then imaged in CL4 media.

Immunofluorescent staining

Cultured cells: Cells were rinsed 1x in prewarmed PBS and fixed by incubating in prewarmed 4% paraformaldehyde for 15 min at 37°C. Cells were then rinsed 3x for 5 min with PBS and permeabilized in 0.1% Triton X-100 for 15 min at RT. Cells were then rinsed with PBS 3x for 5 min and then blocked in 5% BSA for 1 hr at 37° C. Following blocking, cells were briefly rinsed 1x with PBS, and incubated with 1° antibodies for 1 hr at 37° C (mouse anti-EPS8, BD Transduction Laboratories 610144 1:400; Chicken IgY anti-GFP, GFP-1020 Aves Labs 1:200). Cells were then rinsed 4x for 5 min with PBS and incubated with 2° antibodies (Goat anti-mouse Alexa Fluor 488 F(ab')2 fragment, Invitrogen A11017, 1:1000 dilution; Goat anti-mouse Alexa Fluor 568 F(ab')2 fragment A11019, 1:1000 or Goat-anti chicken Alexa Fluor 488 IgG (H+L), Invitrogen A11039, 1:1000 dilution) and Alexa-Fluor 568 Phalloidin (Invitrogen A12380) or Alexa-Fluor 488 Phalloidin (Invitrogen Ref A12379) at 1:200 dilution for 30 min at RT. Following 2° antibody incubation, cells were rinsed 4x for 5 min in PBS and mounted on glass slides using ProLong Gold antifade reagent (Life Technologies). anti-HA rabbit, Invitrogen H6908; anti-myc rabbit; Abcam ab9106) or Alexa Fluor-488 conjugated streptavidin (Invitrogen S32354) all at 1:1000 dilution.

Tissue: Paraffin-embedded tissue sections of mouse WT small intestinal swiss rolls and kidney sections were deparaffinized using HistoClear solution (Fisher) and rehydrated in a descending graded ethanol series (100%, 95%, 90%, 70%, 50%) and rinsed with PBS 3x for 5 min. Slides were then subject to an antigen retrieval step consisting of boiling for 1 hr in a solution of 10 mM Tris (pH 9.0) and 0.5 mM ethylene glycol-bis(β-aminoethyl ether)-*N*,*N*,*N*′,*N*′-tetraacetic acid (EGTA). Slides were then washed in PBS 3x and blocked with 5% normal goat serum (NGS) ON at 4°C. After blocking, slides were briefly rinsed with PBS and stained ON at 4° C with antibodies (mouse anti-EPS8, BD Transduction Laboratories Cat#610144, 1:200; rabbit anti-Villin 1:50, Santa Cruz Cat# SC28283, rabbit anti-KIAA1671, Invitrogen, PA5-53737; mouse anti-Villin, Santa Cruz, sc-66022 1:50) in 1% NGS in PBS. After being washed with PBS four times, samples were incubated with secondary antibodies (Goat anti-mouse Alexa Fluor 488 F(ab')2 fragment, 1:1000; anti-Rabbit H+L Alexa Fluor 568 1:1000 A11011) in 1% NGS in PBS for 2 hr at RT. Slides were then washed 4x with PBS, dehydrated in an ascending ethanol series (50%, 70%, 90%, 95% ,100%), and mounted using ProLong Gold Antifade reagent (Life Technologies).

Drug treatment

Wild-type W4 cells were treated with 1 μg/ml doxycycline for 16 hr prior to cytochalasin D treatment to induce brush border formation. Cells were then treated with 500 nM cytochalasin D or an equivalent volume of DMSO diluted in W4 media for 30 min. Cells were then fixed in 4% paraformaldehyde and stored at 4° C in 1x PBS prior to staining.

Live cell membrane labeling

CL4 cells were incubated with a 1.5x concentration of CellMask-DeepRed plasma membrane dye (Molecular Probes) in Fluorobrite Medium (Gibco) supplemented with 10% FBS and 1% L-glutamine for 10 min at 37° C. Cells were subsequently imaged in supplemented Fluoroborite Medium to minimize background fluorescence.

Microscopy

Light microscopy: Laser scanning confocal microscopy was performed using a Nikon A1R or A1 equipped with 488 and 561 nm excitation lines, and 100x/1.49 NA TIRF, 40x/1.3 NA oil, and 25x/1.05 NA silicon immersion objectives. Structured Illumination Microscopy was performed using a Nikon N-SIM equipped with and Andor DU-897 EMCCD camera, four excitation lines (405, 488, 561, and 647 nm), and a 100x/1.49 NA TIRF objective. All images were reconstructed using Nikon Elements software with matching reconstruction parameters. Spinning disk confocal microscopy was performed using a Nikon Ti2 inverted light microscope equipped with a Yokogawa CSU-X1 spinning disk head, a Photometrics Prime 95B sCMOS or Hamamatsu Fusion BT sCMOS camera, 488 nm and 561 nm excitation lasers, and a 100x/1.49 NA TIRF objective. Cells were maintained in a stage top incubator at 37° C with 5% CO2 (Tokai Hit). In order to capture microvillus growth and collapse events, subconfluent to recently confluent CL4 cells plated on plasma cleaned 35 mm glass bottom dishes (CellVis) were imaged at 30 sec intervals for 30 min in CL4 media. CL4 cells expressing EGFP-EPS8 and mCherry-β-actin were plated on plasma cleaned 35-mm glass bottom dishes

coated with 50 µg/mL laminin to minimize cell lifting during the acquisition. Z stacks of ~3 - 5µm were collected depending on cell thickness and sampled using a 0.18 µm step size with a triggered NIDAQ piezo Z stage. Image acquisition was performed using Nikon Elements software. Movies with intensities compared across conditions were collected using matching laser power and exposure times**.**

Electron microscopy: All scanning electron microscopy (SEM) reagents were purchased from Electron Microscopy Sciences. To prepare samples for EM, cells were plated on glass coverslips and washed once with warm SEM buffer (0.1M HEPES, pH 7.3) supplemented with 2 mM $CaCl_2$, then sequentially fixed for 1 hr at RT with 2.5% glutaraldehyde and 4% paraformaldehyde in SEM buffer supplemented with 2 mM $CaCl_2$, washed with SEM buffer, incubated in 1% tannic acid in SEM buffer for 1 hr, washed with ddH_2O, incubated with 1% OsO4 in ddH_2O for 1 hr, washed with ddH_2O, incubated with 1% uranyl acetate in ddH_2O for 30 min, then washed with ddH_2O. Samples were dehydrated in a graded ethanol series. After dehydration, SEM samples were then dried using critical point drying and mounted on aluminum stubs and coated with gold/palladium using a sputter coater. SEM imaging was performed using Quanta 250 Environmental-SEM operated in high vacuum mode with an accelerating voltage of 5–10 kV.

Biotin proximity labeling pull down and mass spectrometry

W4 cells stably transduced with pLVX-EPS8-BioID2, pLVX-EPS8-13xLBioID2 or pLVX-myc-BioID2 were grown to ~80% confluency in T-175 flasks and incubated for 48 hr in biotin depleted media before induction with doxycycline. 50 µM was added to cell

culture media after 8 hrs of induction with doxycycline, and induced cells were incubated overnight. The following pulldown protocol was drawn largely from (Roux et al., 2018). Cells were rinsed 2x in DPBS and pelleted at 200 x *g* for 5 min. Pelleted cells were resuspended in room temperature Lysis Buffer (8 M Urea, 50 mM Tris-HCl, 1 mM DTT and 1x Halt Protease Inhibitor, pH 7.4). Triton X-100 was added to make a final v/v of 1%, and suspension was mixed by trituration and placed on ice. Samples were then lysed with a 27 ½ gauge needle attached to a 1 mL syringe 6x each and diluted with prechilled lysis buffer to favor affinity capture (Roux et al., 2018). Samples were then spun at 16,500 x *g* for 10 min at 4° C. Supernatant was added to equilibrated streptavidin sepharose high performance beads (GE healthcare) and rotated overnight at 4° C. Beads were then pelleted at 1000 x *g* and resuspended in 1mL Wash Buffer (8 M Urea, 50 mM Tris-HCl, pH 7.4) 4x and resuspended in 1 mL Wash Buffer. 10% of beads were saved for western blot with the other 90% resuspended in 1 mM Biotin + 50 mM NH_4HCO_3 in preparation for mass spectrometry analysis. Mass spectrometry was performed through the Vanderbilt Mass spectrometry core. Briefly, to the bead slurry, 50 ul of 8 M urea 100 mM tris-HCl pH 8.0 was added, disulfide bonds were reduced using TCEP, and alyklated to prevent reformation with iodoacetimde. Slurry was further diluted using 300 ul of 100 mM tris-HCL pH 8.0, 5 ug of sequencing grade trypsin was added and allowed to digest overnight at 37 degrees. 5 ul of the resulting peptides were analyzed by data dependent LC-MS/MS. Briefly, peptides were autosampled onto a 200 mm by 0.1 mm (Jupiter 3 micron, 300A), self-packed analytical column coupled directly to an LTQ linear ion trap mass spectrometer (ThermoFisher) using a nanoelectrospray source and resolved using an aqueous to organic gradient. Both the

intact masses (MS) and fragmentation patters (MS/MS) of the peptides were collected in a data dependent manner utilizing dynamic exclusion to maximize depth of coverage. Resulting peptide MS/MS spectral data were searched against the canonical human protein database (Uniprot), to which common contaminants and reversed version of each protein, using SEQUEST (https://link.springer.com/article/10.1016/1044-0305(94)80016-2). Peptide spectral matches were collated, filtered, and compared using Scaffold (Proteome Software).

Quantification and statistical analysis

Time series analysis of microvillus growth: Events were analyzed manually using tools in FIJI. All measurements were performed on z-projected images deconvolved using the Richardson-Lucy algorithm with 20 iterations in Nikon Elements Software. For EGFP and mCherry co-expressing cells, t = 0 was defined as -3 frames (1.5 min) before the appearance of the EGFP signal. A circular ROI was used to measure the mean EGFP or Halo signal, and the same ROI was then used to track the mCherry signal (ESPN or βactin) of the distal to middle region of the growing microvillus. ROIs of approximately the same size were used for all growth events. For cells expressing mCherry-ESPN only, t = 0 was defined as -3 frames (1.5 min) before the appearance of the mCherry signal, with a circular ROI used to measure the distal to middle region of the growing microvillus. For *de novo* growth, events were excluded if they held less than 3 frames (1.5 min) before the appearance of the EGFP signal, if the microvillus collapsed before reaching steady state growth, if a single bundle immediately gave rise to multiple microvilli, or if significant overlap with adjacent microvilli confounded our

analysis. Using Prism 10 (GraphPad), mean intensity values were first normalized to account for intensity differences between microvilli, with the smallest value equal to 0 and the largest value equal to 1. Normalized values were then averaged and plotted with SD. Photobleaching corrections were not included in the analysis, as there was < 5-10% loss of signal over 10 min with EGFP and mCherry tagged probes.

Percent of ESPN positive bundles with EPS8 puncta: Nikon Elements using “Define Threshold” to segment ESPN positive bundles and “Spot Detection” to detect puncta. The total numbers of ESPN bundles and EPS8 puncta were measured and the “Having” function was used to determine the fraction of ESPN positive bundles with overlapping with EPS8 signal.

EGFP-EPS8 puncta intensities: Nikon Elements using the “Spot Detection” function on the first frame of each time-lapse movie using a cell shaped ROI. Histograms of 16-bit intensities were generated using Prism 10 (Graphpad).

EGFP-EPS8 puncta lifetime*:* Nikon Elements using the “Spot Detection” to detect puncta and “Track Binaries” to track puncta intensities and durations. Mean puncta intensities were then binned into two categories - events lasting < 7 min vs. those lasting ≥ 7min - then plotted using Prism 10 (Graphpad).

Distal tip:cytosol ratios: Intensity measurements were performed in FIJI using SIM images. Images were acquired using matching laser power and exposure times within

experiments. For EGFP-tagged proteins, images were excluded from analysis if raw EGFP intensities were < ~2000 gray values or > ~10,000 gray values – within this range EGFP-EPS8 recapitulated normal EPS8 localization. The EGFP or AlexaFluor488 signal was manually thresholded in each cell, and a rectangular ROI was drawn to measure the mean intensity at the tips of microvilli and in the cytoplasm, excluding the nuclear region. The same ROI area was used within a single cellular measurement, but not necessarily between cells, as to account for variation in cell size and shape.

Microvillus growth rate: The length of the microvillus was measured in FIJI starting at the first frame of detectable coalesced mCherry-ESPN signal ($Length_{initial}$) and then either the last frame of the movie, or the last frame with the microvillus mostly parallel to the cell surface ($Length_{final}$). Events were excluded if the microvillus was mostly perpendicular to the cell surface, or if the growth event lasted less than 3.5 minutes. The growth rate was then calculated using $(Length_{final} – Length_{initial})/(Time_{final}-Time_{initial})$, with individual growth rates represented in the plot.

Initial mean growth intensities: Values were extracted from time series analysis of microvillus growth events. The initial mean intensity is defined as the background subtracted mean intensity of the first frame of detectable EGFP signal (t = 2 min for time series analysis).

Time series analysis of microvillus collapse: Events were measured manually in FIJI. All measurements were performed on z-projected images deconvolved using the

Richardson-Lucy algorithm in Nikon Elements software as described above. For intensity and length measurements defining microvillus collapse, t = 0 is defined as -10 frames before the characteristic drop in EGFP intensity (EGFP-EPS8, EGFP-IRTKS or EZR-GFP), unless specified in figure legends. A circular ROI was drawn to track the EGFP signal at the distal tips of microvilli. This same ROI was then used to measure CellMask-DeepRed intensity, when applicable. Circular ROIs of approximately the same size were used on all events. To measure lengths, a linear ROI was drawn to measure the change in microvilli length over time. Mean intensity values and lengths were first normalized and then averaged using Prism 10 (GraphPad), and plotted with SD. As individual collapse intensity and length traces varied on the timescale of a few minutes, some complementary montage examples may include timepoints outside of the plotted data range. However, plotted averages represent data normalized to the maximum time shown. Photobleaching corrections were not included in the analysis, as there was only ~5-10% loss of signal over 10 min with EGFP and mCherry tagged probes.

Mother/daughter growth event analysis: SEM images were analyzed in FIJI by counting the total number of microvilli using the multipoint tool. Microvilli were scored as mother/daughter structures if they were physically connected or were in orientations consistent with recently separated microvilli (within ~100 nm), with each individual microvillus counted separately. 1,963 total microvilli from four cells were analyzed. The number of mother/daughter growth events was then calculated as a fraction of the total number of microvilli.

Statistical analysis: Statistical testing was performed in Prism 10 (GraphPad), by first running a D'Agostino and Pearson test to determine normality, and then a Mann-Whitney test or an unpaired t-test for pairwise comparison (Fig 1H, Fig S2G) or ANOVA with Kruskal-Wallis to compare more than two conditions (Figs. S3 C-E). For all figures, error bars are SD. Exact n values and their definitions are reported in figure legends.

Line scan analysis: To perform line scan analysis, lines were drawn along the axis of microvilli or linear actin features on maximum intensity projected images in FIJI. Line width was set for the following, tissue: 1, W4 cells: 30, B16F1 cells: 5, CL4 microvilli 4-5. For intestinal tissue, line scan analysis was conducted on 100x images, while a 40x image is represented in the figure (2A). The length and intensity axis were then normalized from 0 to 1, combined and fit to a Gaussian where appropriate (GraphPad Prism). Residual plots were calculated from the difference between raw EGFP-KIAA1671 intensity signals and plotted over the normalized length.

Fraction of overlap: To calculate the fraction of overlap between the KIAA1671 and phalloidin signal in the cytoplasm of W4 cells, an 5x5 µm2 area was cropped and individual channels were manually thresholded in Nikon Elements. A binary layer 'AND' was created to measure the pixel area of overlapping pixel intensities between the 488 and 561 nm channels. To calculate the fraction of overlap, the 'AND' area fraction was divided by the total KIAA1671 area fraction.

Trajectory Analysis: Using Nikon elements “spot detection” to detect puncta and “track binaries” to measure XY trajectories, a subset of puncta from 5x5 μm2 area or a single representative de novo growth event was tracked over a period indicated in the figure legends. XY coordinates were then plotted in GraphPad Prism.

Comparison of UtrCH + and UtrCH - EGFP-KIAA1671 marked puncta: Using Nikon elements “spot detection” to detect puncta, binary layers of EGFP and mCherry channels were created. The binary “HAVING” function was used to segment EGFP (i.e. KIAA1671) puncta that were associated with mCherry (i.e. UtrCH) puncta. “Track binaries” was then used to measure KIAA puncta intensities over time from a 10 x 10 μm image area. Areas that contained large “droplet like” KIAA1671 signal were excluded from analysis. Values were plotted and statistical difference was evaluated using a Mann-Whitney test in GraphPad Prism.

Intensity correlations: Using Nikon elements “spot detection” EGFP-KIAA1671 and mCherry-UtrCH puncta were detected using maximum intensity projected images. Plots represent all thresholded puncta in all frames of time-lapse movies. Intensities from individual channels were normalized, plotted, and pearson r2 and p values were calculated using GraphPad Prism.

Colocalization colormap: The colocalization heatmap was created using the colocalization colormap plugin in FIJI on cropped maximum intensity projected images.

Local protein alignment: Protein sequences were aligned using EMBOSS Water local alignment https://www.ebi.ac.uk/Tools/psa/ with the BLOSUM62 matrix.

CHAPTER III

DIRECT VISUALIZATION OF MICROVILLI BIOGENESIS

Originally published as:

Gaeta IM, Meenderink LM, Postema MM, Cencer CS, Tyska MJ. Direct visualization of epithelial microvilli biogenesis. Curr Biol. 2021 Jun 21;31(12):2561-2575.e6.

Summary

Microvilli are actin bundle-supported surface protrusions that play essential roles in diverse epithelial functions. To develop our understanding of microvilli biogenesis, we used live imaging to directly visualize protrusion growth at early stages of epithelial differentiation. Time-lapse data revealed that specific factors, including epidermal growth factor pathway substrate 8 (EPS8) and insulin-receptor tyrosine kinase substrate (IRTKS, also known as BAIAP2L1), appear in diffraction-limited puncta at the cell surface and mark future sites of microvillus growth. New core actin bundles elongate from these puncta in parallel with the arrival of ezrin and subsequent plasma membrane encapsulation. In addition to *de novo* growth, we also observed that new microvilli emerge from pre-existing protrusions. Moreover, we found that nascent microvilli can also collapse, characterized first by loss of membrane wrapping and ezrin enrichment,

followed by a sharp decrease in distal tip EPS8 and IRTKS levels, and ultimately disassembly of the core actin bundle itself. These studies are the first to offer a temporally resolved microvillus growth mechanism and highlight factors that participate in this process; they also provide important insights on the growth of apical specializations that will likely apply to diverse epithelial contexts.

Introduction

Actin bundle-supported surface protrusions are one of the defining features of eukaryotic cells, conferring the ability to move and sense the surrounding environment. Examples include filopodia and microvilli, fingerlike protrusions that extend from the leading edge of crawling cells and the apical surface of polarized epithelial cells, respectively. In an evolutionary context, filopodia-like structures predate animal cells (Adl et al., 2012), whereas the evolution of microvilli occurred later, emerging in animal cells and choanoflagellates (Karpov and Leadbeater, 1998; Peña et al., 2016). In higher eukaryotes, microvilli are found on the surface of diverse epithelial cell types, including those from intestine and kidney, where they increase apical surface area for nutrient and filtrate absorption, respectively (Helander and Fandriks, 2014). Additionally, in the sensory epithelium, exaggerated microvilli referred to as stereocilia respond to mechanosensory stimuli that allow for hearing (Schwander et al., 2010). Despite their essential roles in a range of epithelial functions, little is known about the temporal and mechanistic details that govern when or how microvilli grow from the apical surface.

Microvilli ultrastructure is well characterized, with data from transmission electron microscopy (TEM) and biochemical studies spanning nearly six decades. Moreover,

proteomic analyses have revealed a comprehensive list of resident proteins, many of which interact directly with the actin cytoskeleton (McConnell et al., 2011b; Revenu et al., 2012). In transporting epithelia, microvilli extend microns from the cell surface, supported by a core of ~20-40 actin filaments (Mooseker and Tilney, 1975a; Ohta et al., 2012). Actin filaments are bundled in parallel by villin-1 (VIL1), plastin-1 (PLS1, also known as fimbrin), and espin (ESPN) (Bartles et al., 1998; Bretscher and Weber, 1979a; Bretscher and Weber, 1980). This core actin bundle is physically linked to the encapsulating plasma membrane by membrane-cytoskeleton linkers including ezrin (EZR), myosin-1A (MYO1A), and myosin-6 (MYO6) (Berryman et al., 1993; Bretscher, 1983; Hegan et al., 2012; Howe and Mooseker, 1983). Within core bundles, actin filament barbed ends, which represent favorable sites for monomer incorporation, are oriented towards the distal tips (Mooseker and Tilney, 1975a). Core bundle barbed ends are embedded in an electron dense cap, which may be enriched in factors that control the microvilli growth (Mooseker and Tilney, 1975a; Tilney and Cardell, 1970). Electron dense caps are also found at the tips of filopodia and stereocilia (Rzadzinska et al., 2004; Svitkina et al., 2003) suggesting a universal function in protrusion formation.

Although our understanding of molecular factors that control actin polymerization has expanded significantly in recent years, how microvillar growth is initiated at the cell surface remains unclear. Due to its exquisitely specific enrichment at the tips of microvilli, stereocilia and filopodia (Croce et al., 2004; Disanza et al., 2006; Manor et al., 2011a; Postema et al., 2018b), epidermal growth factor pathway substrate 8 (EPS8) is of particular interest as a factor that may initiate and/or drive protrusion growth. EPS8 consists of an N-terminal phosphotyrosine binding (PTB) domain, a central SH3

domain, and C-terminal actin-binding motifs (Disanza et al., 2004; Hertzog et al., 2010). Studies in mouse models showed that loss of EPS8 leads to shortening of both microvilli and stereocilia (Tocchetti et al., 2010; Zampini et al., 2011), suggesting a role in elongating both of these structures. EPS8 is also required for proper apical morphogenesis in *C. elegans* intestine, where genetic ablation leads to gross defects in tissue morphology and lethality if both EPS8 isoforms are lost (Croce et al., 2004). Consistent with these findings, our group recently determined that EPS8 and IRTKS work together to promote elongation of microvilli (Postema et al., 2018b) and directional persistence of motile microvilli early in differentiation (Meenderink et al., 2019). Mechanistically, EPS8 has been assigned both actin capping and bundling functions (Disanza et al., 2004; Hertzog et al., 2010). While its localization at the tips of protrusions is consistent with a potential role in capping barbed ends, this function is at odds with shortened protrusions that result from EPS8 loss-of-function (Postema et al., 2018b; Tocchetti et al., 2010; Zampini et al., 2011). Additionally, tip enrichment is not entirely consistent with a canonical role as a filament bundler, as other bundling proteins that reside in actin cores such as VIL1, PLS1, and ESPN localize along the length of protrusions (Bartles et al., 1998; Bretscher and Weber, 1979b).

Though our understanding of microvillus ultrastructure and resident proteins has expanded in recent years, little is known about how protrusion growth is initiated at the apical surface during epithelial differentiation. To address this knowledge gap, we developed a live imaging assay that enabled us to directly observe the *de novo* growth of individual microvilli on the surface of epithelial cells. Based on its ubiquitous appearance at the tips of microvilli in diverse epithelial tissues and cell culture models,

we tested the idea that EPS8 is involved in the *de novo* growth of microvilli. Consistent with this hypothesis, we observed that EPS8 and its binding partner IRTKS both marked sites of future microvilli growth. EPS8 and IRTKS puncta also remained associated with the distal tips of core actin bundles as these structures elongated. Unexpectedly, we also found that new microvilli commonly emerge from the base of pre-existing protrusions. Finally, we observed that membrane-cytoskeleton linking by ezrin, membrane wrapping, and enrichment of EPS8 and IRTKS are all needed for the survival of nascent microvilli, and that loss of membrane wrapping or tip enriched factors leads to core actin bundle disassembly. These data offer a high resolution molecular and temporal framework for understanding the growth of new microvilli on the apical surface of differentiating epithelial cells.

Results

An approach for visualizing the *de novo* growth of individual microvilli

To define the time-course of molecular events that drive microvillus growth, we first established a live imaging approach. Here, we turned to the LLC-PK1-CL4 (CL4) porcine cell culture model, which we recently used to dissect mechanisms of microvillar motility (Meenderink et al., 2019). These cells provide a powerful model for studying apical morphogenesis, as early in differentiation the surface density of microvilli is sparse enough to allow for observations of individual protrusions. CL4 microvilli also extend from the surface at all angles, which enables their visualization in volume projections generated using spinning disk confocal microscopy and structured illumination microscopy (SIM) (Figure 3-1A, 3-2A). To capture individual growth events,

we imaged sub-confluent or recently confluent CL4 cells at 30 second intervals for 30 minutes. Even under these conditions, quantifying individual growth events was limited to a subset of cells and events. For example, some cells produced few or no *de novo* growth events during the acquisition; in other cells, overlapping structures precluded measurement or events did not meet temporal selection criteria (see Methods). Using mCherry-ESPN (herein referred to as ESPN) as a probe for core actin bundles, we measured maximum projected intensities in the distal half of the growing microvillus. Normalized ESPN intensity increased and then plateaued after ~5 min (Figs. 3-1 B and C), demonstrating the core actin bundles that support microvilli are assembled on a timescale of minutes.

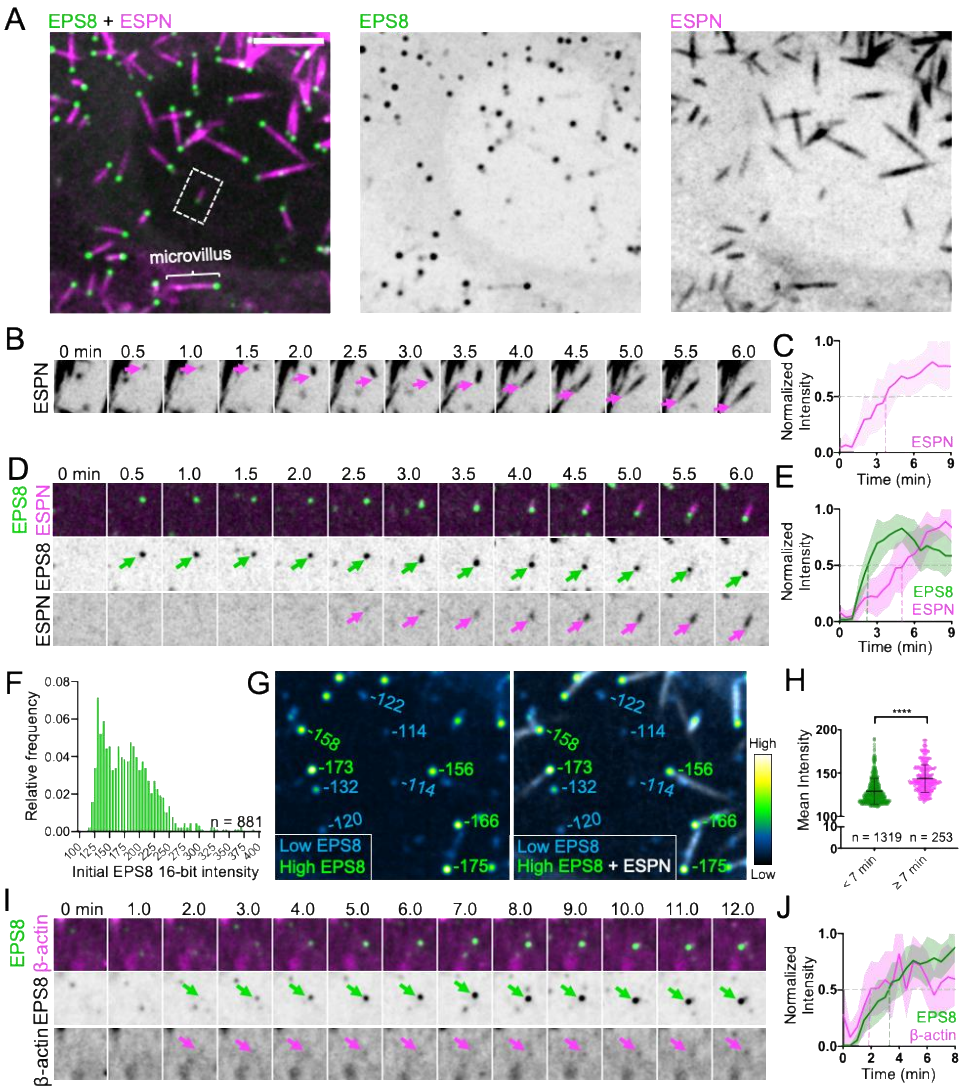

Figure 3-1. Microvilli emerge from discrete EPS8 puncta on the apical surface of CL4 cells. (A) Maximum intensity projection of a CL4 cell displaying microvilli. Core actin bundles are visualized by mCherry-ESPN (magenta) and EGFP-EPS8 (green). Merge (left), EGFP-EPS8 (middle), mCherry-ESPN (right). Scale bar = 5 µm. A single microvillus is denoted with the bracket. Dashed box represents microvillus shown in D. Related to Video S1. (B) Montage of a de novo microvillus growth event from a CL4 cell overexpressing mCherry-ESPN alone; magenta arrows mark the growing end of the core bundle. Box width = 4 µm. (C) Normalized intensity vs. time curve for microvillus growth events in CL4 cells expressing mCherry-ESPN alone; n = 13 events from 9 cells. T = 0 is defined as -3 frames (1.5 min) before the appearance of the mCherry-ESPN signal. (D) Montage of a de novo microvillus growth event from a CL4 cell expressing EGFP-EPS8 and mCherry-ESPN. Arrows denote the presence of EGFP-EPS8 (green) or mCherry-ESPN (magenta) at the growing end of the core bundle. Box width = 4 µm. Related to Video S2. (E) Normalized intensity vs. time curves for microvillus growth events in cells expressing EGFP-EPS8 (green) and mCherry-ESPN (magenta); n = 14

events from 7 cells. (F) EGFP-EPS8 puncta intensity histogram; n = number of puncta from a single representative cell. (G) Left, EGFP-EPS8 puncta pseudocolored by intensity, from the cell shown in A at a single time point. Right, merge of EGFP-EPS8 and mCherry-ESPN signals to differentiate bundle associated and non-bundle associated puncta. Values adjacent to each punctum represent raw deconvolved 16-bit intensity units. Box width = 14 µm. (H) EGFP-EPS8 puncta mean intensity plot with values derived from a single representative cell binned by lifetime (< 7 min or ≥ 7 min); n = number of puncta. ****p<0.0001, Mann-Whitney test. (I) Montage of a de novo microvillus growth event in a CL4 cell expressing EGFP-EPS8 and mCherry-β-actin. Arrows denote the accumulation of EGFP-EPS8 (green) or mCherry-β-actin (magenta). Box width = 4 µm. Related to Video S3. (J) Normalized intensity vs. time curves for CL4 cells expressing EGFP-EPS8 (green) and mCherry-β-actin (magenta): n = 9 growth events from 5 cells. For E and J, t = 0 is defined as -3 frames (1.5 min) before the appearance of the EGFP-EPS8 signal. All images shown are maximum intensity projections. Dashed lines for all normalized intensity vs. time curves indicate point at which curves cross a normalized intensity of 0.5. For all curves, the solid line represents the mean and shading represents SD.

Initiation of microvillus growth coincides with EPS8 enrichment in discrete puncta

EPS8 exhibits striking distal tip localization in diverse cell culture models and tissues, in every case examined by us and others (Figures 3-1A, 3-2, and 3-3)(Croce et al., 2004; Manor et al., 2011a; Postema et al., 2018b; Zwaenepoel et al., 2012). Importantly, EPS8 localizes to the tips of microvilli in intestinal crypt cells as well as crypt-like Ls174T-W4 (W4) cells (Figures 3-2B and 3-3A) suggesting this factor may be involved in early stages of microvilli growth. Moreover, we found that EPS8 distal tip enrichment is reduced in W4 cells treated with the barbed end blocking drug, cytochalasin D (Figures 3-2 E-G). These data suggest that EPS8 binds directly to filament barbed ends and thus, is well positioned to regulate core actin bundle growth. With this in mind, we sought to determine when EPS8 arrives relative to the formation of core bundles as marked by ESPN accumulation. In CL4 cells co-expressing ESPN and EGFP-EPS8 (herein referred to as EPS8), analysis of 1011 ESPN positive bundles from 19 cells

showed 88% were associated with EPS8 puncta, a value that is likely an underestimate due to limitations in core bundle segmentation. Time-lapse imaging revealed that future sites of microvillus growth are marked by the appearance of bright EPS8 puncta (Figure 3-1 D). Based on time series intensity plots, we found that on average ESPN begins to accumulate at the same time as EPS8 at these sites, albeit at a much slower rate (Figure 3-1E). Analysis of initial EPS8 puncta intensities revealed distributions that were at least bimodal (Figure 3-1F). In general, we found that the brightest EPS8 puncta were associated with ESPN positive actin bundles, whereas dimmer puncta were not bundle associated (Figure 3-1G, green vs. blue values, respectively). Moreover, analysis of 16,921 EPS8 puncta from 14 cells revealed that puncta with lifetimes ≥ 7 min — the approximate duration of microvillus maturation (Figure 3-1E) — had significantly higher mean intensities than puncta with duration times < 7 min (Figure 3-1H). Together these data suggest EPS8 puncta likely undergo maturation, accumulating to a threshold level of EPS8 before they can support the elongation of microvilli.

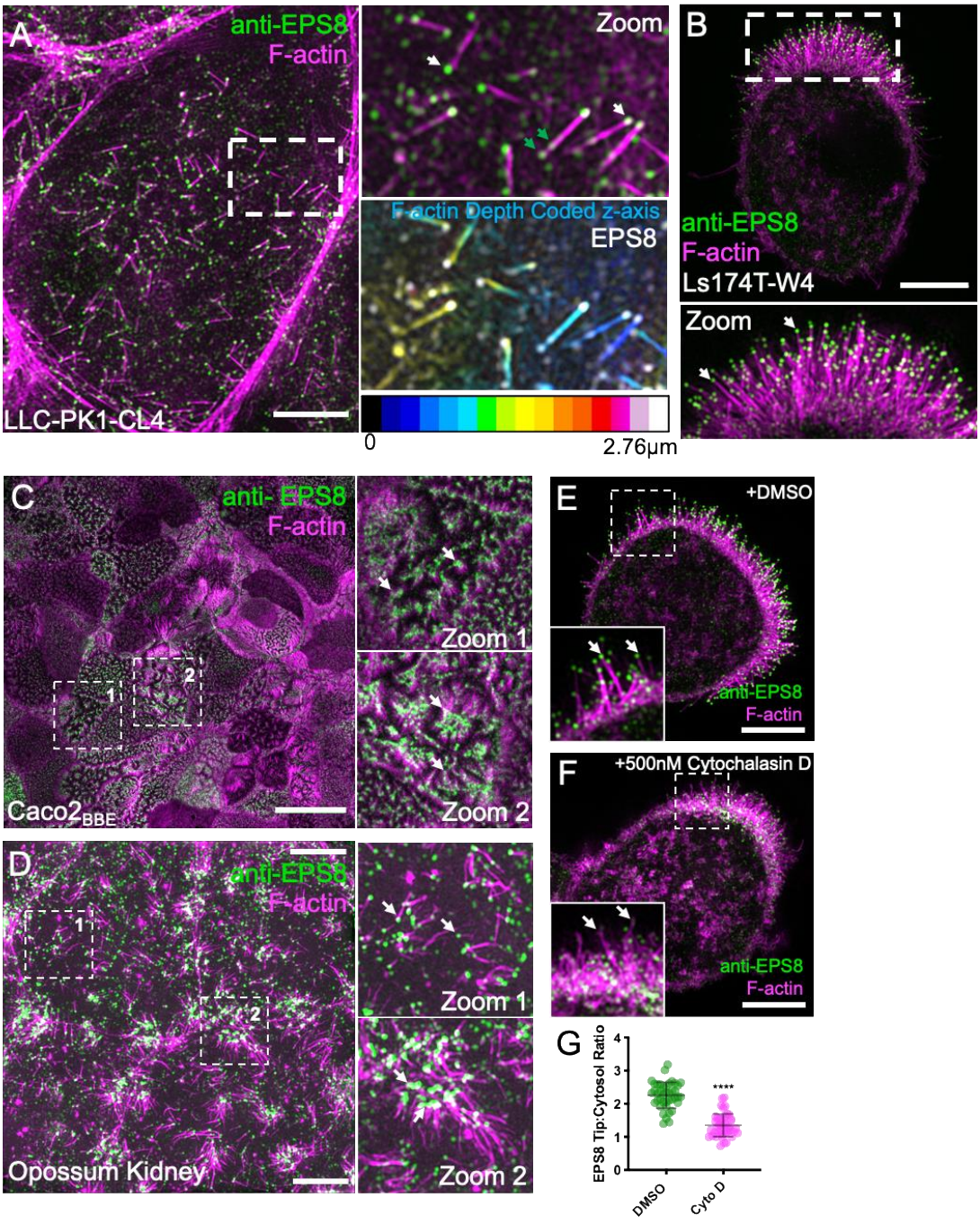

Figure 3-2. EPS8 localizes to the tips of microvilli in cell culture models. (A) Representative CL4 cell from an early stage of differentiation stained with an anti-EPS8 antibody and phalloidin to mark F-actin. Scale bar = 5µm. Zoom panels highlight individual microvilli and depth coding in the z plane. White arrows denote tip targeted EPS8. Occasionally, we see EPS8 localize along the side of the microvillus actin bundle (green arrows). (B) Representative image of W4 cell stained with an anti-EPS8 antibody and phalloidin. Arrows in zoom panel highlight EPS8 at the tips of microvilli. Scale bar = 5µm. (C) CACO-2BBE cells at day 3 post confluency stained for EPS8 and phalloidin.

Scale bar = 25μm. Zoom panels highlight EPS8 at the tips of microvilli. (D) Opossum kidney (OK) cells at day 2 post confluency stained for EPS8 and phalloidin. Scale bar = 5μm. Zoom panels highlight EPS8 at the tips of microvilli.

(E) W4 cell treated with DMSO and stained for with an anti-EPS8 antibody and phalloidin. Dashed box indicates zoom, and arrows highlight EPS8 at the tips of microvilli. (F) W4 cell treated with 500nM cytochalasin D for 30 minutes and stained with an anti-EPS8 antibody and phalloidin. Dashed box indicates zoom and arrows highlight the de-enrichment of EPS8 from tips of microvilli. (G) Quantification of EPS8 tip enrichment for cells represented in E&F. ****p<0.0001 using an unpaired t-test. N = 41 DMSO treated cells and n = 43 cytochalasin D treated cells from 3 independent experiments. Error bars indicate mean ± SD. Images in A, B, D, E & F were acquired using structured illumination microscopy, image in C was acquired using confocal microscopy. All images are maximum intensity z projections.

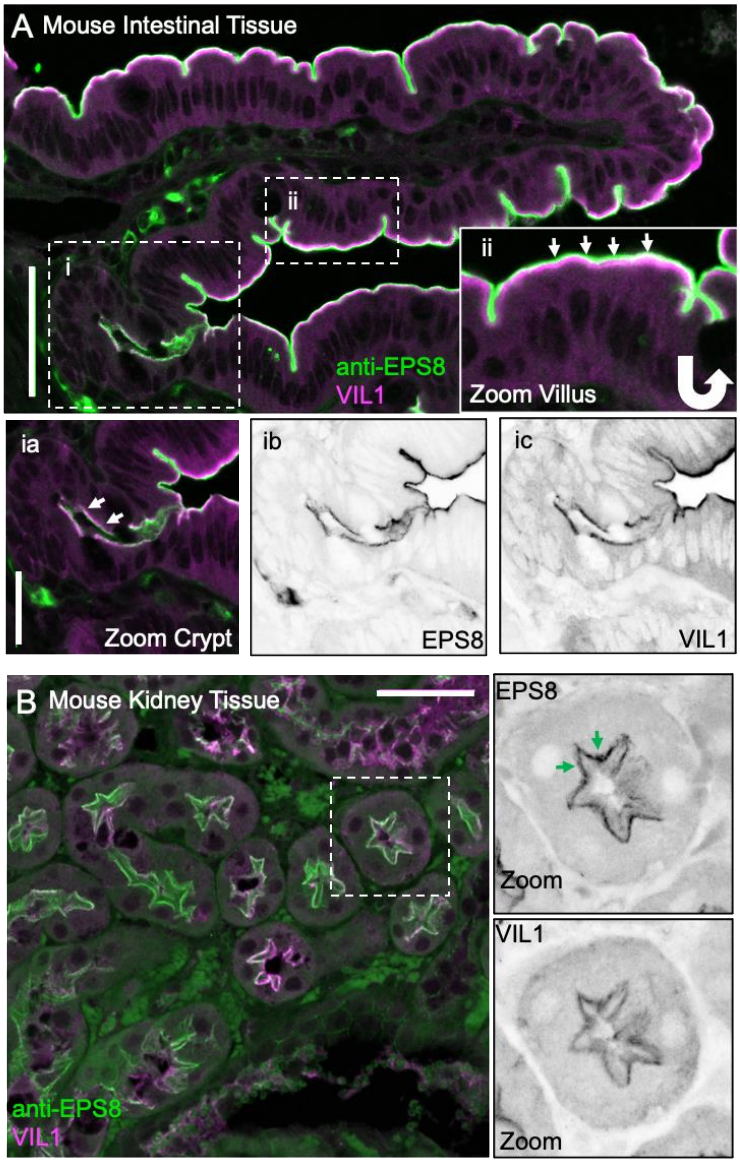

Figure 3-3. EPS8 localizes to the apical surface of mouse intestinal and kidney tissue. (A) Representative image of paraffin embedded mouse intestinal tissue stained for endogenous EPS8 and the microvilli actin bundle marker villin. Scale bar = 50μm. Zoom boxes from i indicate the crypt compartment and ii indicates the villus. Arrows in ii and ia denote tip localization of EPS8. Scale bar for ia = 25μm. Images in A are from a single optical section acquired using confocal microscopy. (B) Representative images of paraffin embedded mouse kidney tissue stained for endogenous EPS8 and villin. Dashed box indicates zoom. Green arrows indicate EPS8 enrichment at the apical domain of kidney tubules. Scale bar = 50μm. Images in B are maximum intensity projections acquired using confocal microscopy.

Although live cell probes that specifically report on the localization of G-actin are not available, co-expression of mCherry-β-actin (labeling G- and F-actin pools) with EPS8 revealed that microvillus growth events were preceded by the coalescence of β-actin signal, which coincided with the appearance of EPS8 puncta (Figure 3-1 I and J). In combination, these findings lead us to conclude that EPS8 puncta mark sites of microvillus growth and incorporate β-actin before actin core bundle elongation begins.

Mutation of actin binding residues impairs EPS8 puncta formation

As specific residues near the C-terminus of EPS8 (a.a. 649-822) have been implicated in actin binding (Hertzog et al., 2010), we sought to determine if these motifs are important for EPS8 enrichment in puncta that associate with nascent microvilli (Figure 3-4). To this end, we examined the behavior of two EPS8 variants with mutations in these C-terminal motifs: V690D/L694D, which is expected to exhibit defective filament capping activity, and LNK758-760AAA (referred to herein as LNK:AAA), which is predicted to lack filament bundling activity (Hertzog et al., 2010) (Figure 3-5). Using a tip targeting assay in W4 cells as we previously described (Grega-Larson et al., 2015; Postema et al., 2018b), both of

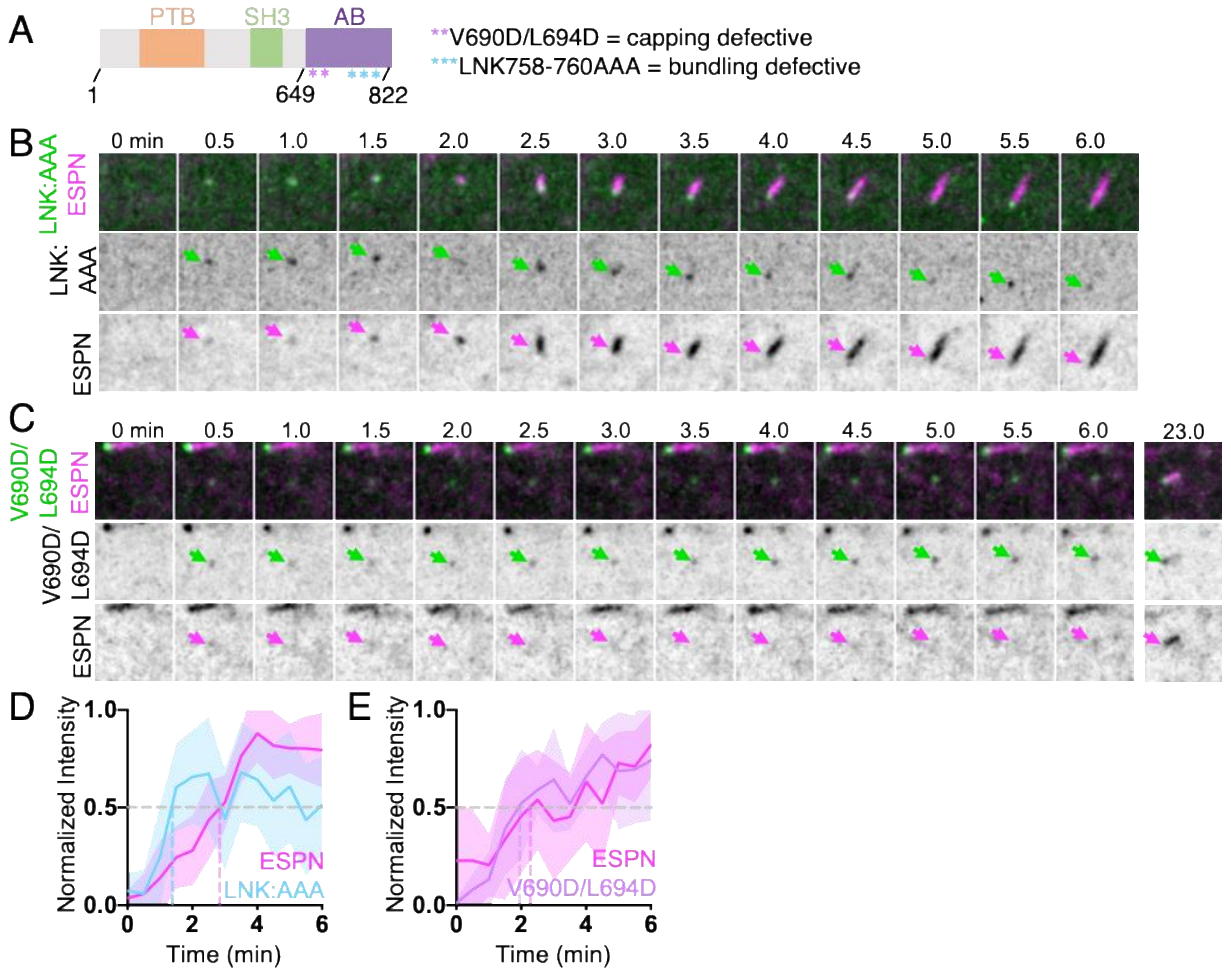

Figure 3-4. EPS8 actin binding mutants disrupt EPS8 puncta formation and core bundle growth. (A) Domain diagram of human EPS8. PTB = phosphotyrosine binding domain, SH3 = src-homology 3 domain, AB = actin binding domain. Asterisks represent point mutations in the residues shown. (B) Montage of a de novo microvillus growth event in a CL4 cell expressing EGFP-EPS8 LNK758-760AAA (LNK:AAA) and mCherry-ESPN. Arrows denote the accumulation of EGFP-EPS8 LNK:AAA (green) or mCherry-ESPN (magenta). Box width = 4 µm. (C) Montage of a de novo microvillus growth event in cell expressing EGFP-EPS8 V690D/L694D and mCherry-ESPN. Arrows denote the accumulation of EGFP-EPS8 V690D/L694D (green) or mCherry-ESPN (magenta). Box width = 4 µm. (D) Normalized intensity vs. time curve for microvillus growth events in cells expressing EGFP-EPS8 LNK:AAA (light blue) and mCherry-ESPN (magenta); n = 11 events from 5 cells. (E) Normalized intensity vs. time curves for microvillus growth events in cells expressing EGFP-EPS8 V690D/L694D (lavender) and mCherry-ESPN (magenta); n = 9 events from 4 cells. For D and E, t = 0 is defined as -3 frames (1.5 min) before the appearance of the EGFP-EPS8 LNK:AAA or EGFP-EPS8 V690D L694D signal. All images shown are maximum intensity projections. For all normalized intensity vs. time curves, dashed lines indicate when curves cross a normalized intensity of 0.5. For all curves, the solid line represents the mean and shading represents SD.

these variants demonstrated distal tip enrichment relative to GFP only control, albeit reduced compared to WT EPS8 (Figures 3-5 B,C). Additionally, we found that expression of an EPS8 mutant completely lacking the C-terminal actin binding region (EPS8 1-648) still retained some distal tip targeting activity, while expression of the C-terminal actin binding region alone (EPS8 649-822) did not. This suggests actin binding activity of EPS8 is necessary but not sufficient for robust distal tip targeting. To determine if mutations in the EPS8 actin binding motif impact the dynamics of microvilli growth, we co-expressed the EPS8-LNK:AAA or EPS8-V690D/L694D mutants with ESPN in CL4 cells (Figure 3-4). Although appearance of EPS8-LNK:AAA generally preceded ESPN accumulation, its signal exhibited pronounced intensity fluctuations during the imaging time course (Figures 3-4 B,D). Moreover, while the appearance of EPS8-V690D/L694D coincided with a diffuse cloud of ESPN, coalescence of this signal into a linear structure was delayed, in some instances occurring several minutes after the initial appearance of ESPN (Figure 3-4 C,E). Cells expressing EPS8-V690D/L694D exhibited significantly slower microvillus growth rates (0.07 ± 0.03 μm/min) compared to that of cells expressing ESPN alone (0.15± 0.07 μm/min). In contrast, growth rates in cells expressing WT EPS8 (0.12 ± 0.05 μm/min) and EPS8-LNK:AAA (0.21 ± 0.14 μm/min) were not statistically different from cells expressing ESPN alone (Figure 3-5 D). Finally, EPS8-LNK:AAA exhibited significantly decreased initial mean intensities (measured in the first frame of detectable punctate EGFP signal) compared to EPS8 (Figure 3-5 E). Together these fixed and live cell data suggest that the LNK758-760 and V690/L694 actin binding motifs promote the formation of EPS8 puncta and subsequent efficient assembly of core bundles

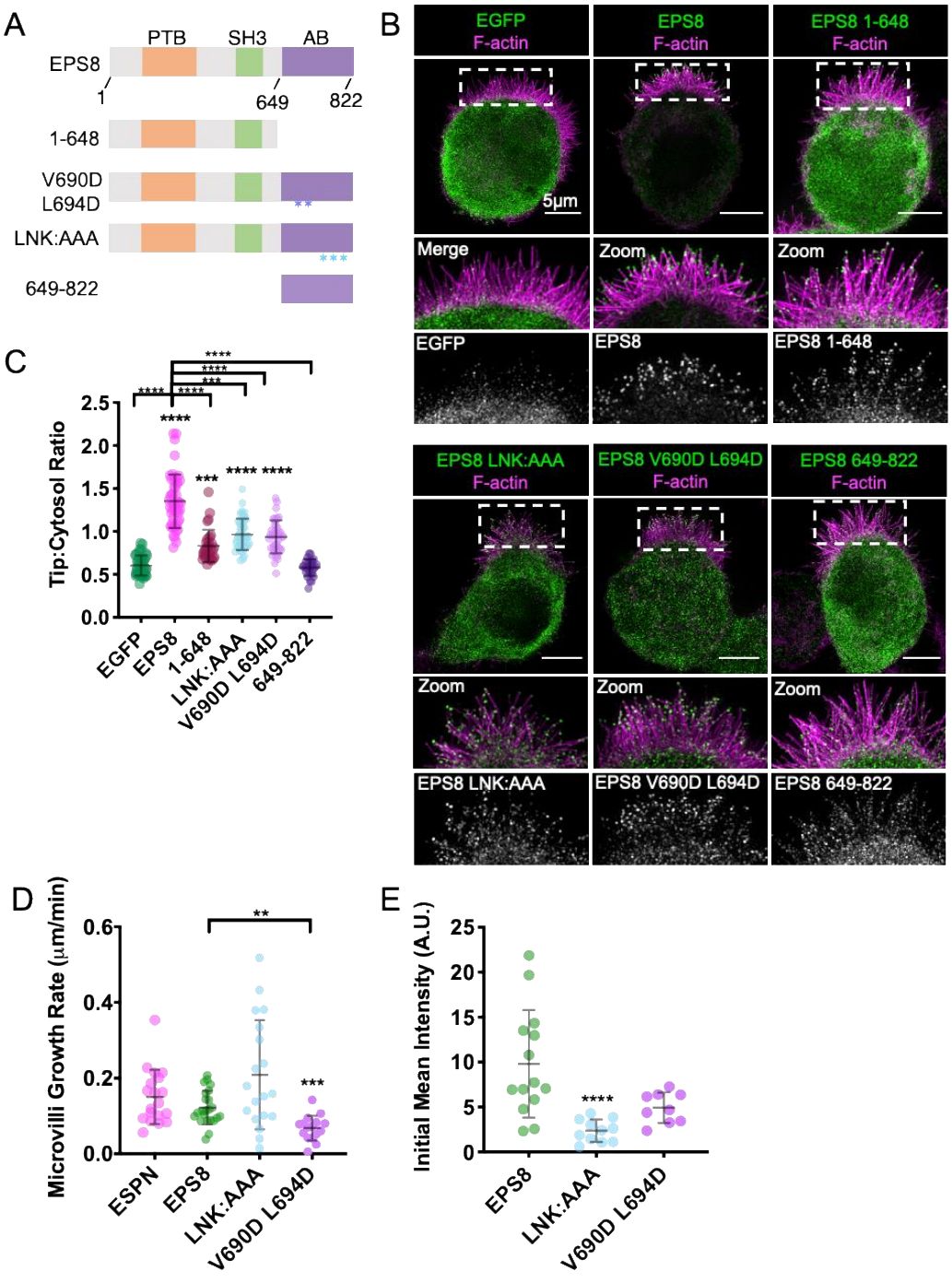

Figure 3-5. EPS8 mutants affect EPS8 puncta formation and microvillus growth. (A) EPS8 domain diagram. PTB = Phosphotyrosine Binding Domain, SH3 = Src-Homology 3, AB = Actin Binding. Putative capping and bundling point defective mutations are denoted by asterisks. (B) Representative images of EGFP only control and EGFP-EPS8 overexpression mutants in W4 cells imaged by SIM, displayed as maximum intensity projections. Dashed boxes indicate zoom and highlight protein localization in microvilli in merged and EGFP channels. F-actin is visualized by

phalloidin. Images are not matched for brightness and contrast to show precise localization detail. (C) Quantification of tip to cytosol ratios of cells shown in B. Using ANOVA with Kruskal-Wallis, ****p<0.0001, ***p=0.0008, compared to EGFP only control. Bracketed asterisks use ANOVA with Kruskal-Wallis compared to EGFP-EPS8 ****p<0.0001, ***p=0.0004. EGFP n = 41 cells; EPS8 n = 48 cells; 1-648 n = 30 cells; V690D L694D n = 40 cells; LNK:AAA n = 43 cells; 649-822 n = 27 cells. Error bars indicate mean ± SD. Cells from all conditions are from least three independent transfections. (D) Quantification of microvillus growth rate. Using ANOVA with Kruskal-Wallis, ***p=0.0004 compared to ESPN only control. Bracketed asterisks use ANOVA with Kruskal-Wallis compared to EGFP-EPS8 ***p=0.0045. ESPN n = 19 growth events, IRTKS n = 19 growth events, EPS8 n = 23 growth events, LNK:AAA n=19 growth events, V690D L694D n = 16 growth events. Error bars indicate mean ± SD. Each data point represents a single de novo microvillus growth event (E) Initial Mean Intensity values, signifying background subtracted 16-bit intensity from the first frame of detectable EGFP signal for each condition. Each data point represents a single de novo microvillus growth event, corresponding to data shown in Figure1 E (EPS8), Figure2 D (LNK:AAA), and Figure2 E (V690D L694D). Using ANOVA with Kruskal-Wallis, ****p<0.0001 compared to EPS8. EPS8 n = 14, LNK:AAA n = 11, and V690D L694D n = 9 growth events. Error bars indicate mean ± SD

Nascent microvilli also emerge from pre-existing protrusions

In contrast to *de novo* growth events, we unexpectedly observed that microvilli grow from pre-existing microvilli. In these cases, a nascent “mother” microvillus gave rise to one or more “daughter” microvilli (Figure 3-6 A, M = mother, D = daughter). New daughter core bundles grew at angles to the pre-existing mother, giving rise to a structure with a branched or forked appearance (see 3 min time point, Figure 3-6 A). Daughter microvilli typically emerged from the base or the side of an existing mother bundle, and 3D volume rendering of these structures confirmed that daughters are initially physically linked to their mothers (Figure 3-10 A). New daughter bundles eventually separated from mother bundles to become individualized protrusions (5 min time point, Figure 3-6 A). Using SEM, we also observed branched microvilli on the apical surface of CL4 cells expressing ESPN (Figure 3-6 B), suggesting that branched core bundles are in fact wrapped in plasma membrane. From SEM images, we

estimated that ~25% of all microvilli appeared physically connected in a branched structure (Figure 3-6 B, zoom 1) or oriented relative to a neighboring protrusion at an angle consistent with a branched structure (Figure 3-6 B, zoom 2). Given that daughter microvilli separate from their mothers after their initial growth, 25% likely marks a lower bound for the fraction of total microvilli that are generated using this mechanism.

In cells co-expressing EPS8 and ESPN, the growth of daughter microvilli was marked by small dim puncta of EPS8 that traveled retrograde from the distal tip of an existing mother to a site near its base (Figure 3-6 C). Consistent with this observation, we also noted dim EPS8 puncta localized to the base of microvilli in fixed CL4 cells stained for endogenous EPS8 (Figure 3-2 A, top zoom, green arrows). By specifically tracking the fate of the EPS8 puncta that emerged during these events, we determined that daughter core bundles, in turn, serve as new mothers that give rise to new daughters, propagating the cycle of biogenesis (Figure 3-6 D). Interestingly, the intensity of EPS8 at the distal tip of a microvillus dropped following the appearance of dim retrograde traveling puncta (compare pre vs. post, Figure 3-6 E). Intensity analysis of distal tip vs. retrograde traveling EPS8 puncta revealed that the EPS8 signal that gives rise to daughter microvilli appears at the expense of EPS8 signal at the distal tip (Figure 3-6 E, Zoom). Based on these data, we propose that formation of daughter microvilli from pre-existing mothers represents a distinct mechanism from *de novo* growth, which takes advantage of assembly factors such as EPS8 that are enriched in the vicinity of pre-existing structures.

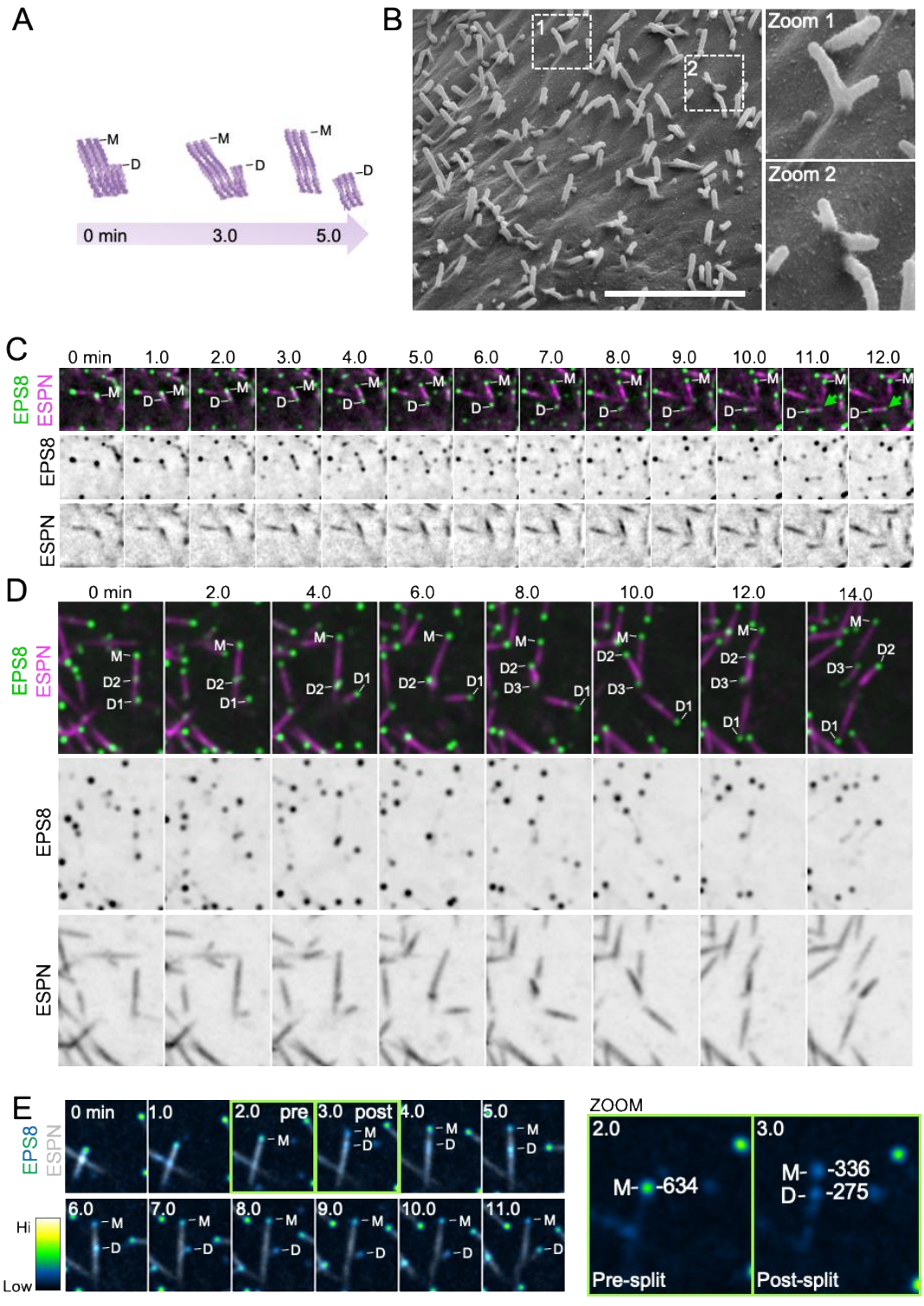
A
M
D
0 min
3.0
5.0
B
1
2
Zoom 1
Zoom 2
C
0 min
1.0
2.0
3.0
4.0
5.0
6.0
7.0
8.0
9.0
10.0
11.0
12.0
EPS8
ESPN
D
0 min
2.0
4.0
6.0
8.0
10.0
12.0
14.0
M
D2
D1
D3
E
0 min
1.0
2.0 pre
3.0 post
4.0
5.0
6.0
7.0
8.0
9.0
10.0
11.0
Hi
Low
ZOOM
2.0
M- -634
3.0
M- -336
D- -275
Pre-split
Post-split

Figure 3-6. New microvilli can grow from pre-existing microvilli. (A) Top, representative montage of a daughter microvillus growing from the base of an existing mother bundle in a CL4 cell expressing mCherry-ESPN. “M” denotes the mother microvillus and “D” denotes the growing daughter. Box width = 6 µm. Bottom, cartoon schematic of mother/daughter growth corresponding to montage above. Related to Figure S4 and Video S4. (B) SEM image of a CL4 cell expressing mCherry-ESPN at an early stage of differentiation. Zoom 1 highlights a branched mother/daughter structure whereas zoom 2 likely shows core bundles that may still be physically coupled beneath the plasma membrane. Scale bar = 4 µm. (C) Representative montage of a daughter microvillus growing from the base of an existing mother bundle in cells expressing EGFP-EPS8 and mCherry-Espin. “M” denotes EPS8 at the tip of the mother microvillus and “D” denotes EPS8 which will eventually mark the tip of a growing daughter microvillus. Green arrow highlights an EPS8 punctum forming at the base of the daughter bundle. Box width = 6 µm. (D) Representative montage of a mother microvillus in a CL4 cell expressing EGFP-EPS8 and mCherry-ESPN giving rise to multiple daughter microvilli from the base of the mother bundle. “M” denotes EPS8 at the tip of the mother microvillus and “D1-3” denote EPS8 puncta at the tips of growing daughters. Box width = 6.6 µm. (E) Montage of a daughter microvillus growth event (left) with EGFP-EPS8 pseudocolored by intensity. Green boxes highlight pre- and post-split frames. The corresponding quantification of EGFP-EPS8 integrated 16-bit intensity pre- and post-splitting of EPS8 tip punctum is highlighted in the zoom panels to the right. Note that the total post-split integrated intensity is nearly equal to the pre-split integrated intensity. Box width = 5.6 µm. All images shown are maximum intensity projections.

IRTKS is also enriched in puncta that give rise to new microvilli

Previous work from our group implicated IRTKS as a binding partner of EPS8 and demonstrated that these proteins work together to promote the elongation of microvilli (Postema et al., 2018b). IRTKS possesses both membrane and actin binding motifs through its I-BAR and WH2 domains, respectively, and localizes to the tips of nascent microvilli in the crypts of intestinal organoids and W4 cells in culture (Postema et al., 2018b; Zhao et al., 2011). Based on these properties, we sought to determine if IRTKS, like EPS8, accumulates in the puncta that give rise to microvilli. EGFP-IRTKS (herein referred to as IRTKS) exhibited enrichment in discrete puncta at the tips of existing microvilli, and also demonstrated some lateral localization (Figure 3-7 A), as shown

previously (Meenderink et al., 2019). Like EPS8, IRTKS marked sites of microvilli growth (Figure 3-7 B, Video S5). Based on time series intensity plots, we found that on average ESPN begins to accumulate at the same time as IRTKS at these sites, albeit at a slower rate (Figure 3-7 D). The growth of daughter microvilli was also marked by small dim IRTKS puncta that were laterally associated with pre-existing mother core bundles (Figure 3-7 C). Thus, EPS8 binding partner IRTKS also accumulates in diffraction limited puncta that eventually give rise to new microvilli.

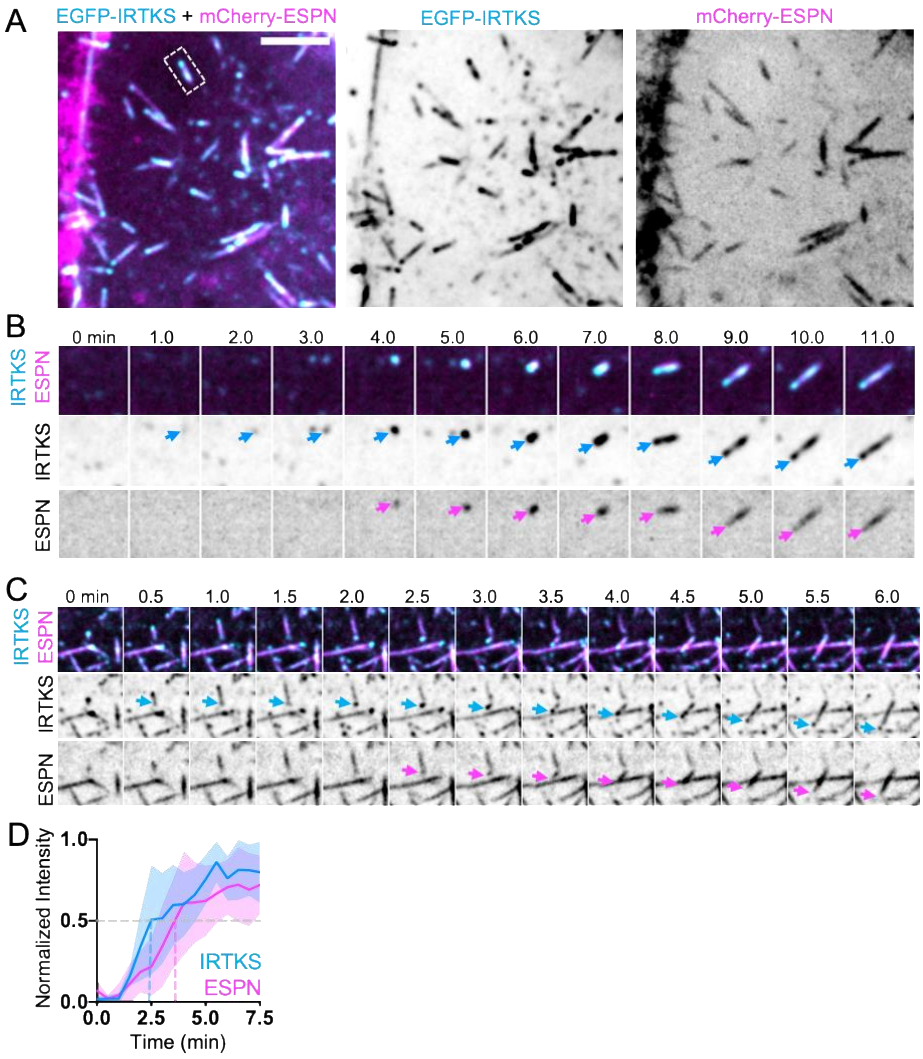

Figure 3-7. IRTKS is enriched in puncta that give rise to new microvilli. (A) Maximum intensity projection of a CL4 cell expressing mCherry-ESPN (magenta) and EGFP-IRTKS (cyan). Merge (left), EGFP-IRTKS (middle), mCherry-ESPN (right). Dashed box indicates microvillus shown in B. Scale bar = 5 µm. (B) Montage of a de novo microvillus growth event in a cell expressing EGFP-IRTKS and mCherry-ESPN. Arrows denote the presence of EGFP-IRTKS (cyan) or mCherry-ESPN (magenta). Box width = 4 µm. Related to Video S5 (C) Montage of daughter microvillus growing from pre-existing mother bundle in a cell expressing EGFP-IRTKS and mCherry-ESPN. Arrows denote EGFP-IRTKS (cyan) and mCherry-ESPN (magenta) of the daughter microvillus. Box width = 6 µm. (D) Normalized intensity vs. time curve of CL4 cells expressing EGFP-IRTKS and mCherry-ESPN; n = 9 events from 4 cells. T = 0 is defined as -3 frames (1.5 min) before the appearance of the EGFP-IRTKS signal. All images shown are maximum intensity projections. Dashed lines indicate point at which curves cross a normalized intensity of 0.5. For all curves, the solid line represents the mean and shading represents SD.

Core actin bundle elongation coincides with plasma membrane wrapping

As microvilli are plasma membrane wrapped protrusions, and because IRTKS directly interacts with the membrane through its I-BAR domain (Saarikangas et al., 2009), we sought to determine the timing of membrane wrapping relative to the formation of IRTKS puncta and the subsequent growth of core bundles. To test whether enrichment of IRTKS precedes membrane encapsulation, we incubated cells co-expressing IRTKS and ESPN with the live cell plasma membrane label CellMask-DeepRed (herein referred to as CellMask) (Figure 3-8 A and D). Individual microvilli typically exhibited CellMask enrichment at the distal end, which we interpreted as membrane encapsulation (Figure 3-8 F). During *de novo* growth events, IRTKS enriched in puncta prior to the accumulation of ESPN and CellMask, which both increased in parallel (Figures 3-8 A and D). Additionally, we found that daughter microvilli also become wrapped in membrane (Figure 3-8 B), which is consistent with the branched microvilli observed in SEM images (Figure 3-6 B). We next asked if membrane wrapping during microvillus growth was driven by the accumulation of membrane-actin linker proteins

(Pelaseyed and Bretscher, 2018). Here, we focused on the Ezrin-Radixin-Moesin (ERM) family protein EZR, which is known to stabilize microvilli (Pelaseyed and Bretscher, 2018). Live imaging revealed that EZR-EGFP (herein referred to as EZR) and ESPN accumulated in parallel during microvillus growth (Figures 3-8 C and E). Together, these data suggest that core bundle formation and membrane wrapping driven by EZR are parallel events in microvillus growth, which follow the appearance of EPS8 and IRTKS puncta at the apical surface.

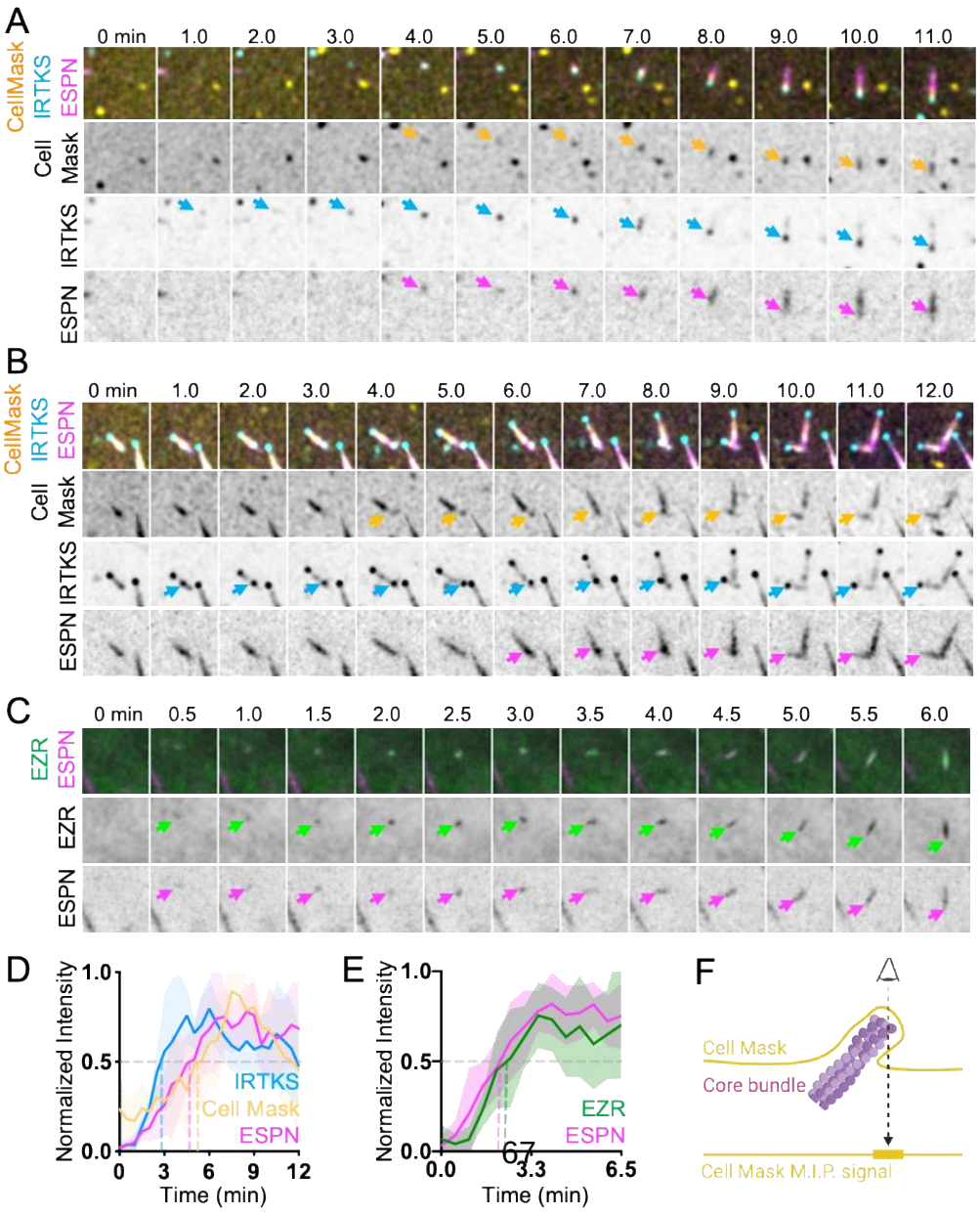

Figure 3-8. Membrane encapsulation occurs in parallel with core bundle formation. (A) Montage of de novo microvillus growth event in a CL4 cell expressing EGFP-IRTKS and mCherry-ESPN and stained with CellMask-DeepRed to mark the plasma membrane. Arrows denote the onset of membrane wrapping visualized by CellMask-DeepRed (yellow), or the presence of EGFP-IRTKS (cyan) and mCherry-ESPN (magenta). Box width = 4 µm. (B) Representative montage of daughter microvillus formation in a cell expressing EGFP-IRTKS and mCherry-ESPN and stained with CellMask-DeepRed. Arrows denote the onset of membrane wrapping as visualized by CellMask-DeepRed (yellow), or the presence of EGFP-IRTKS (cyan) and mCherry-ESPN (magenta) of the daughter microvillus. Related to Video S6. (C) Montage of a de novo microvillus growth event in a CL4 cell expressing EZR-GFP and mCherry-ESPN. Arrows denote the presence of EZR-GFP (green) or mCherry-ESPN (magenta). Box width = 4 µm. Related to Video S7. (D) Normalized intensity curves of cells expressing EGFP-IRTKS and mCherry-ESPN and stained with CellMask-DeepRed corresponding to montage in A; n = 6 growth events from 3 cells. (E) Normalized intensity curves of cells expressing EZR-GFP and mCherry-ESPN corresponding to montage in C; n = 11 growth events from 8 cells. (F) Schematic representation of a microvillus stained with cell mask and the resulting maximum intensity projected signal. All images shown are maximum intensity projections. Dashed lines for normalized intensity curves indicate point at which curves cross a normalized intensity of 0.5. For all curves, the solid line represents the mean and shading represents SD. For D and E, t = 0 is defined as -3 frames (1.5 min) before the appearance of the EGFP-IRTKS or EZR-EGFP signal.

Loss of membrane wrapping and tip targeted factors destabilizes core actin bundles

Analysis of our time-lapse data revealed that a subset of nascent microvilli collapsed, characterized by loss of ESPN signal and associated factors (Figure 3-9). Interestingly, collapse events were preceded by loss of EPS8 puncta from the distal tips (Figure 3-9 A and C), which was immediately followed by a decrease in core bundle length (Figure 3-9 A and C). We also observed instances where core bundles appeared to “break”; in these cases, the core bundle remnant that maintained distal tip enriched EPS8 persisted, whereas the newer core bundle fragment that lacked EPS8 signal quickly collapsed (Figure 3-10 B). Additionally, we found that remnants of collapsed bundles were occasionally used as substrate for growth of one or more daughter microvilli

(Figure 3-10 C). We observed the same general pattern with cells co-expressing IRTKS and ESPN, whereby loss of punctate IRTKS signal was followed by a decrease in microvillus length (Figures 3-9 B and D). These results suggest that loss of EPS8 or IRTKS from the distal tip destabilizes nascent microvilli and leads to their collapse.

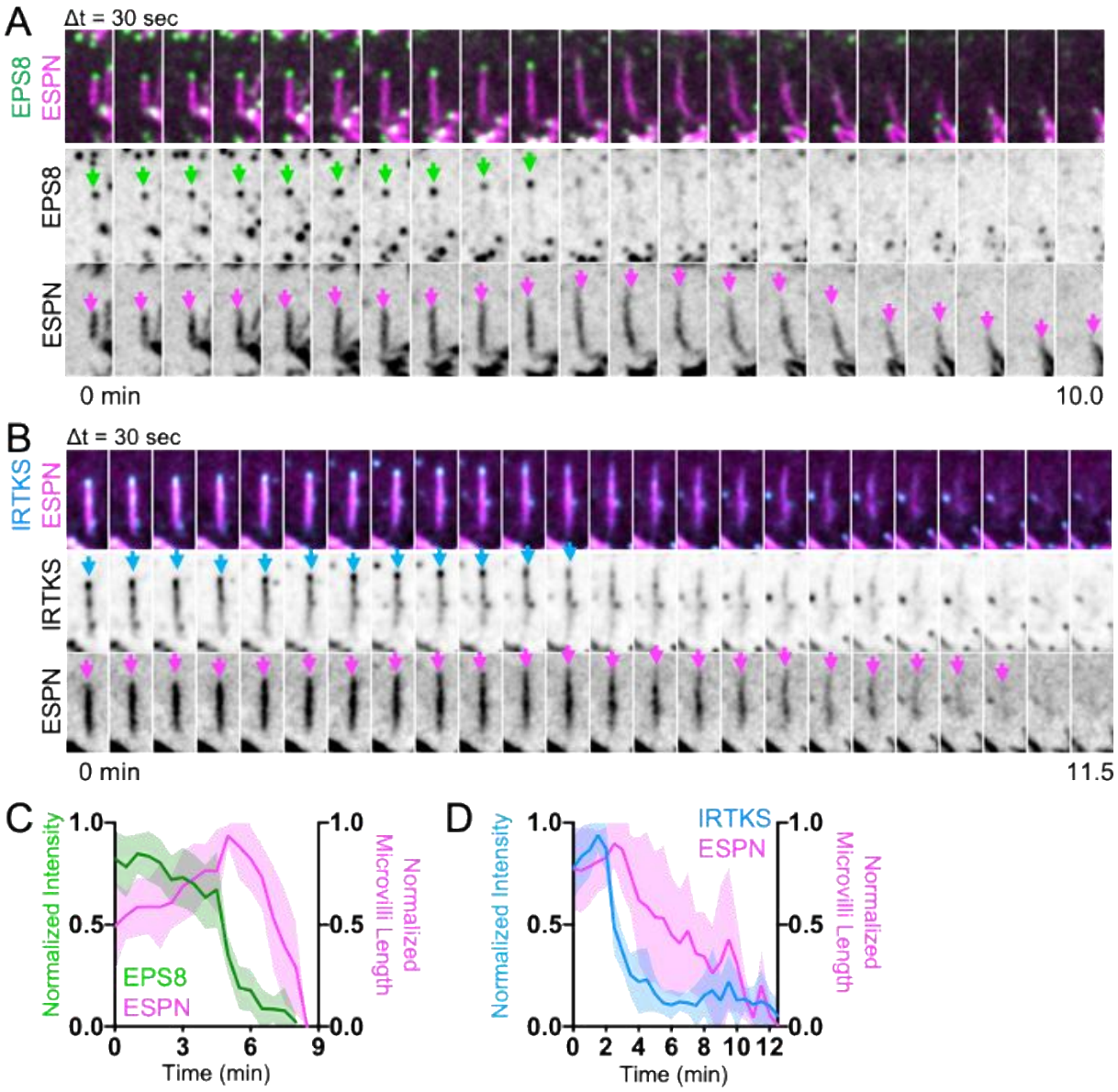

Figure 3-9. Microvilli cannot survive without EPS8 and IRTKS at the tips. (A) Montage of a microvillus collapse event on the surface of a CL4 cell expressing EGFP-EPS8 and mCherry-ESPN. Green arrows denote tip targeted EGFP-EPS8 signal, whereas magenta arrows denote the core actin bundle. Box width = 2.5 μm. Related to

Video S8. See also Figure S4. (B) Montage of microvillus collapse event in a cell expressing EGFP-IRTKS and mCherry-ESPN. Cyan arrows denote tip targeted EGFP-IRTKS signal. Magenta arrows denote the core actin bundle. Box width = 2.5 μm. (C) Quantification of EGFP-EPS8 intensity and microvilli length vs. time during microvillus collapse; n = 10 events from 6 cells. (D) Quantification of EGFP-IRTKS intensity and microvilli length vs. time during microvillus collapse; this plot was created by averaging traces of varying lengths ranging in duration from 4.5 - 12.5 min (IRTKS) and 4.5 - 12.5 min (ESPN); n = 12 events from 5 cells. For C, t = 0 is defined as -10 frames (5 min) before the drop in EGFP-EPS8 intensity from the tips of microvilli, whereas for D, t = 0 is defined as -5 frames (2.5 min) before the drop in EGFP-IRTKS intensity from the tips of microvilli. All images are represented as maximum intensity projections. For all curves, the solid line represents the mean and shading represents SD.

These observations prompted us to investigate upstream events that could potentially lead to loss of tip targeted factors and subsequent microvillus collapse. As IRTKS and EPS8 are enriched at the interface between membrane and core bundle, we again used CellMask to visualize the plasma membrane during collapse events. Interestingly, we found that CellMask enrichment, which we interpret as protruding membrane, is lost prior to collapse (Figure 3-11 A-D). Loss of CellMask signal was followed by loss of punctate IRTKS signal and a subsequent decrease in microvillus length as marked by ESPN (Figures 3-11 A andC, 3-10 D). Next, we determined if loss of membrane encapsulation

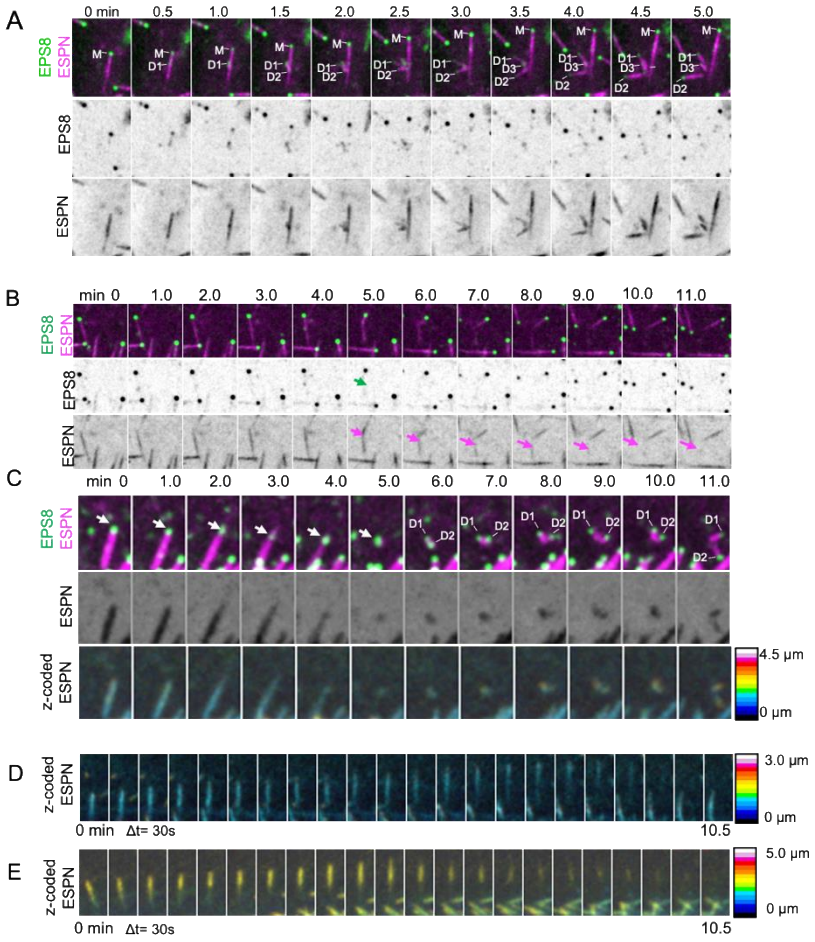

Figure 3-10. Daughter microvilli actin bundles are derived from the mother microvillus, and z visualization of collapsing microvilli actin bundles. (A) Representative montage of multiple daughter microvilli growing from the side of a mother microvillus in a CL4 cell expressing EGFP-EPS8 and mCherry-ESPN. “M” denotes EPS8 at the tip of the mother microvillus and “D1-3” denote EPS8 at the tip of the growing daughter microvilli. Box width = 6 µm. Related to Video S4 (B) Representative montage of a microvillus bundle breaking, and the proximal end undergoing collapse (magenta arrows) in a CL4 cell expressing EGFP-EPS8 and mCherry-ESPN. Note the lack of a significant concentration of EPS8 at the tip of the collapsing bundle (green arrow). Box width = 6.6 µm. (C) Representative montage of a CL4 cell expressing EGFP-EPS8 and mCherry-ESPN wherein a microvillus undergoes collapse, and new daughter microvilli grow from remnants of EPS8 puncta and ESPN. Arrows denote EPS8 at the tip of the collapsing bundle, while D1 and D2 denote EPS8 at the tips of daughter bundles 1 and 2. Z-coded ESPN is included to show the core bundle does not drift out of plane. Box width = 3µm. (D) Z-coding of the mCherry-ESPN channel in a CL4 cell also expressing EGFP-IRTKS and stained with CellMask-DeepRed, demonstrating the bundle does not drift out of frame. Related to Figure 7A. Box width = 2.5µm. (E) Z-coding of the mCherry-ESPN channel in a CL4 also expressing EGFP-EZR and stained with CellMask-DeepRed, demonstrating the bundle does not drift out of frame. Related to Figure 7B. Box width = 2.5µm.

was linked to a loss of EZR signal from nascent microvilli. Indeed, CellMask and EZR signals decreased in parallel, before a measurable decrease in microvillus length as marked by ESPN (Figures 3-11 B and D, 3-10 E). These results suggest that microvilli cannot survive without membrane wrapping, loss of which is paralleled by loss of membrane-cytoskeleton linking, followed by loss of distal tip factors, and ultimately collapse of the core bundle. These findings also reveal that early in epithelial differentiation nascent microvilli undergo cycles of growth and collapse, which likely offer a degree of plasticity during the complex process of apical morphogenesis.

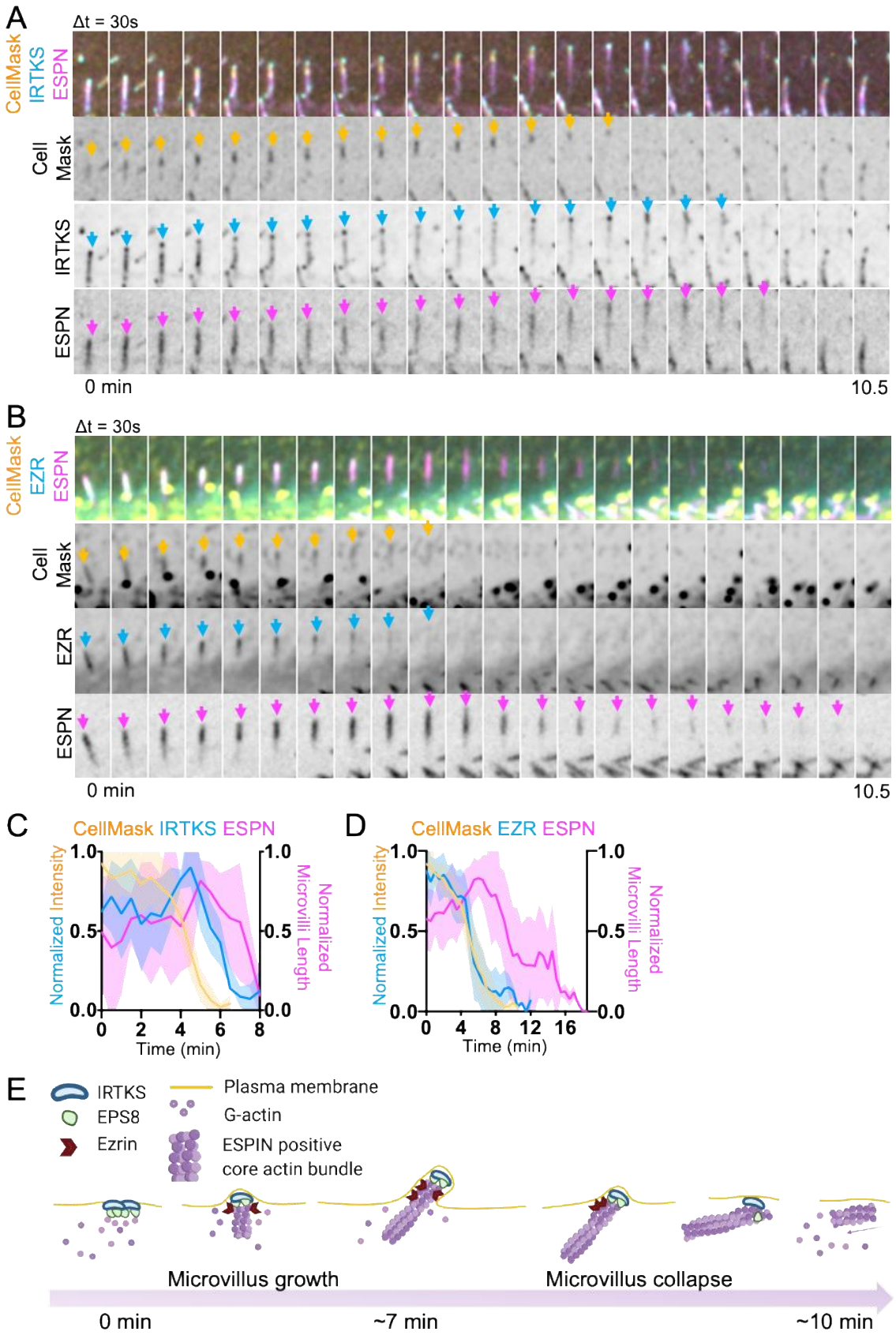
A
Δt = 30s
CellMask IRTKS ESPN
Cell Mask
IRTKS
ESPN
0 min
10.5
B
Δt = 30s
CellMask EZR ESPN
Cell Mask
EZR
ESPN
0 min
10.5
C
CellMask IRTKS ESPN
Normalized Intensity
Normalized Microvilli Length
1.0
0.5
0.0
0 2 4 6 8
Time (min)
D
CellMask EZR ESPN
Normalized Intensity
Normalized Microvilli Length
1.0
0.5
0.0
0 4 8 12 16
Time (min)
E
IRTKS
EPS8
Ezrin
Plasma membrane
G-actin
ESPIN positive core actin bundle
Microvillus growth
Microvillus collapse
0 min
~7 min
~10 min

Figure 3-11. Membrane encapsulation is essential for microvillus survival. (A) Montage of a microvillus collapse event in a cell expressing EGFP-IRTKS and mCherry-ESPN, stained with CellMask-DeepRed. Box width = 2.5 μm. Related to Video S9. See also Figure S4D. (B) Montage of a microvillus collapse event in a cell expressing EZR-EGFP and mCherry-ESPN, stained with CellMask-DeepRed. Box width = 2.5 μm. Related to Video S10. See also Figure S4E. (C) Quantification of EGFP-IRTKS and CellMask-DeepRed intensity and microvilli length as represented in A; n = 4 events from 4 cells. (D) Quantification of EZR-EGFP and CellMask-DeepRed intensity and microvilli length vs. time. This plot was created by averaging traces of varying lengths ranging in duration from 6.5 - 12 min (EZR), 6 - 10.5 min (Cell Mask) and 7.5 - 18.5 min (ESPN); n = 15 events from 10 cells. For C and D, t = 0 is defined as -10 frames (5 min) before the drop in EGFP-IRTKS or EZR-EGFP intensity at the tips of microvilli. All images are represented as maximum intensity projections. For all curves, the solid line represents the mean and shading represents SD. (E) Model of de novo microvillus growth and collapse. Formation of EPS8 and IRTKS pucta coincide with local enrichment of G-actin followed by assembly of ESPN positive core actin bundles, recruitment of EZR, and plasma membrane protrusion. The process of de novo growth occurs on the scale of ~7 minutes. During microvillus collapse, nascent bundles lose membrane wrapping and enrichment of EZR in parallel, which in turn leads to loss of EPS8 and IRTKS, and subsequent collapse of the ESPN positive core actin bundle. The process of collapse also occurs on the scale of minutes. Model was created using BioRender.

Discussion

Here we employed a live imaging approach to define a time-course for the recruitment of factors that drive the growth and stabilization of new microvilli. Using CL4 cells as an epithelial model system, our goal was to capture the earliest events underlying biogenesis of these protrusions. The resulting spatially and temporally resolved datasets allow us to stage the appearance of a core set of microvillar components including G-actin, tip enriched actin regulatory factors, filament bundling proteins, membrane-cytoskeleton linkers and the plasma membrane during this dynamic process (Figure 3-11 E). The growth of a new microvillus takes place over the course of several minutes, similar to the timeframe reported for microvilli in Xenopus kidney epithelial A6 cells (Gorelik et al., 2003). The earliest events that we were able to detect in this process are the enrichment of distal tip factors, EPS8 and IRTKS, in diffraction limited

puncta at the apical surface. EPS8 enrichment is also accompanied by a moderate accumulation of G-actin. The tip enrichment of EPS8 is at least partially driven by binding to actin, as mutations in actin binding residues interfered with puncta formation and EPS8 puncta not associated with actin bundles typically exhibited lower intensities. Furthermore, mutation of the V690 and L694 residues resulted in delayed core bundle formation and decreased growth rates suggesting direct involvement of EPS8 in the growth of these structures. On average, ESPN begins to accumulate with the appearance of EPS8/IRTKS puncta, although at a slower rate. Simultaneous enrichment of ESPN with the CellMask membrane probe and membrane-actin linker EZR suggests that actin core bundles are assembled in close proximity to the apical surface, where they are quickly or immediately encapsulated in plasma membrane. The time course of molecular recruitment described here provides a framework for understanding how cells control the growth of surface features and may also apply to other finger-like protrusions such as stereocilia.

Because the appearance of EPS8 and IRTKS puncta preceded the formation of microvilli observed in our assays, it is tempting to speculate that these factors are components of the electron dense tip complex, which has long been proposed to function in initiating growth and thus, regulating protrusion numbers (Tilney and Cardell, 1970). However, it also remains possible that other as-of-yet unidentified factors function upstream of EPS8 and IRTKS, to drive their accumulation at the plasma membrane and specify sites of growth. This latter possibility is consistent with previous studies showing that protrusion numbers are not significantly reduced in EPS8 loss-of-function models (Croce et al., 2004; Postema et al., 2018b; Zampini et al., 2011).

In addition to *de novo* microvillus growth events, we also observed the formation of daughter microvilli from pre-existing mother protrusions. Formation of a new daughter core bundle was preceded by enrichment of EPS8 and IRTKS at the site of lateral growth from the mother. Relative to *de novo* assembly, such mother/daughter growth might be energetically favorable as materials for growing a new microvillus, such as distal tip factors and G-actin/F-actin, are enriched near pre-existing protrusions. In combination with *de novo* growth, mother/daughter growth might allow epithelial cells to quickly populate their apical surface with microvilli. This would be advantageous in the intestinal epithelium, where cells rapidly increase the number of microvilli as they migrate from stem cell containing crypts on to the villus (Specian and Neutra, 1981; van Dongen et al., 1976). The mother/daughter growth mechanism initially gives rise to structures with a forked appearance, and these are strikingly reminiscent of the “forked microvilli” captured during recovery from hydrostatic pressure effacement (Tilney and Cardell, 1970). Remarkably, the authors noted electron dense plaques on the lateral surface of the newly formed core bundles, which were hypothesized to represent material that promotes the growth of new microvilli. One intriguing possibility is that the lateral plaques observed by Tilney and Cardell represent protein complexes that contain EPS8 and IRTKS, which would be consistent with our live time-lapse data. Moreover, given that Tilney and Cardell used intestinal epithelial samples from salamander and the observations we report here focused on cells derived from porcine kidney, the mother/daughter growth mechanism is likely conserved across species and tissue types.

Interestingly, not all nascent microvilli survive, and a notable fraction of the protrusions observed in our time-lapse datasets collapsed during the period of observation, consistent with previous observations using scanning ion conductance microscopy in *Xenopus* kidney epithelial A6 cells (Gorelik et al., 2003) (Figure 7E). Collapse of a microvillus is predicted by loss of plasma membrane wrapping, which occurs in parallel with decreased membrane-cytoskeleton linking by EZR. Loss of membrane encapsulation is followed by loss of tip targeted EPS8 and IRTKS, which in turn is ultimately followed by collapse of the core actin bundle. This implies that in order to survive, core bundles must remain at least partially encapsulated by the plasma membrane. What leads to the loss of membrane-actin linking and membrane wrapping is not clear. As our time-lapse observations take place at the earliest stages of apical surface maturation, one possibility is that the cells are not yet expressing the factors needed to stabilize microvilli at high levels. This would be consistent with previous studies showing that a number of microvillus resident proteins gradually accumulate during the time course of differentiation (Crawley et al., 2014b; Heintzelman and Mooseker, 1990). An interesting example is provided by tip-targeted protocadherins, CDHR5 and CDHR2, which drive adherence between neighboring protrusions, and in turn might drive a mechanical capture mechanism that permits the long-term survival of new microvilli, as we proposed previously (Meenderink et al., 2019).

While this study offers a temporally resolved molecular framework for understanding the growth of new microvilli, important questions remain unanswered. One question of longstanding interest pertains to mechanisms that control the number of actin filaments per core bundle. Microvilli in mature transporting epithelia exhibit a

highly stereotyped number of actin filaments (~20-40) per core bundle (Mooseker and Tilney, 1975a; Ohta et al., 2012), suggesting that cells enlist mechanisms to count bundle components. One attractive hypothesis is that proteins in the distal tip complex control filament numbers (Tilney and Cardell, 1970). If EPS8 does interact directly with filament barbed ends, the number of EPS8 molecules per tip puncta might be linked to the number of actin filaments per core bundle. Because the transfection-based studies described here rely on exogenous marker expression to label growing protrusions, our data do not allow us to define the absolute stoichiometry of EPS8 in tip targeted puncta. Future studies might address such questions by combining epithelial cell culture models expressing endogenously tagged molecules of interest with the methods for visualizing microvillus growth we introduce in this work.

Another important unanswered question asks how distal tip enriched factors are initially recruited to the plasma membrane. Epithelial cells are characterized by polarized separation of phosphatidylinositols, with phosphatidylinositol 4,5 bisphosphate ($PI[4,5]P_2$) and phosphatidylinositol 3,4 bisphosphate ($PI[3,4]P_2$) enriched at the apical surface and phosphatidyl inositol 3,4,5-trisphosphate ($PI[3,4,5]P_3$) enriched basolaterally (Gassama-Diagne et al., 2006; Martin-Belmonte et al., 2007; Roman-Fernandez et al., 2018). Although the emergence of EPS8 and IRTKS puncta appears to be stochastic in nature, the local enrichment of signaling lipids such as $PI[4,5]P_2$, could be involved in recruitment of these factors. Both EPS8 and IRTKS contain structural motifs that make this a reasonable possibility. For instance, the EPS8 PTB domain shares sequence similarity with the PTB domain of Dab1, which has been shown to bind $PI[4,5]P_2$ (Uhlik et al., 2005). Similarly, other proteins of the I-BAR family

such as MTSS1 (also known as MIM) and IRSP53 (also known as BAIAP2), have also been shown to directly bind PI[4,5]P_2 (Mattila et al., 2007; Saarikangas et al., 2009). Future time-resolved studies must focus on defining the nature of EPS8 interactions with membrane lipids and determining whether localization of EPS8 and IRTKS is controlled by specific lipid species.

In summary, this study is the first to capture the molecular details of microvilli biogenesis using a live imaging approach. The resulting time-lapse datasets allow us to construct a temporal framework for key factors involved in microvillus growth and offer insight into the nature of apical surface dynamics at early timepoints in epithelial differentiation. These results also hold implications for understanding the assembly and dynamics of related actin supported protrusions. For example, classic ultrastructural studies of early stage chick embryos revealed that the formation of stereocilia is preceded by the growth of microvilli (Tilney et al., 1992a). A fraction of these microvilli are resorbed, and the remaining protrusions are believed to mature into stereocilia arranged in the characteristic staircase pattern. The collapse dynamics we report here may offer a mechanism to explain microvillar resorption during sensory epithelium differentiation.

CHAPTER IV

BioID2 screening identifies KIAA1671 as an EPS8 proximal factor that marks sites of microvillus growth

Abstract

Microvilli are defining morphological features of the apical surface in diverse epithelial tissues. To develop our understanding of microvilli biogenesis, we used a biotin proximity labeling approach to uncover new molecules enriched near EPS8, a well-studied marker of the microvillus distal tip compartment. Mass spectrometry of biotinylated hits identified KIAA1671, a large (~200 kDa), disordered, and previously uncharacterized protein. Based on immunofluorescent staining and expression of fluorescent protein tagged constructs, we found KIAA1671 localizes to the base of the brush border in native intestinal tissue and polarized epithelial cell culture models, as well as dynamic actin-rich structures in unpolarized, non-epithelial cell types. Live imaging also revealed that during the early stages of microvillar growth, KIAA1671 colocalizes with EPS8 in diffraction-limited puncta. However, once elongation of the core bundle begins, these two factors separate, with EPS8 tracking the distal end and KIAA1671 remaining behind at the base of the structure. These results suggest KIAA1671 cooperates with EPS8 and potentially other assembly factors to initiate growth of microvilli on the apical surface. These findings offer new details on how transporting epithelial cells build the brush border and may inform our understanding of how apical specializations are assembled in other epithelial contexts.

Introduction

Microvilli are actin-bundle supported protrusions that decorate the apical surface of diverse epithelial cell types, imparting these tissues with specialized functions ranging from solute uptake to mechanosensation. In the case of transporting epithelia, microvilli are organized into densely packed arrays that maximize apical plasma membrane holding capacity and thus the functional surface area available for interacting with the luminal space. Known as “brush borders”, these critical solute transporting organelles drive nutrient uptake in the intestinal tract and filtrate absorption in the kidney tubule (Helander and Fandriks, 2014; Welling and Welling, 1975). Exaggerated microvilli known as stereocilia also play central roles in the mechanosensory function of the cochlea and vestibular epithelial systems (McGrath et al., 2017). Though microvilli and similar fingerlike protrusions have evolved to function broadly in physiology, our understanding of mechanisms that control the assembly of these structures during differentiation remains limited. The goal of this study was to identity new proteins that are well positioned to drive the growth of microvilli during the maturation of transporting epithelial cells.

Ultrastructural studies dating back several decades were the first to provide key details on microvillus architecture (Granger and Baker, 1950). An individual microvillus extends a micron or more from the apical surface, supported by a core bundle of 20-40 actin filaments that are bundled in parallel (Mooseker and Tilney, 1975a; Ohta et al., 2012). All filaments within the core bundle are oriented with their barbed ends – the preferred site of new actin monomer incorporation – out into the distal tip, whereas the pointed

ends extend down into the sub-apical cytoplasm and are anchored in a filamentous network known as the terminal web (Mooseker and Tilney, 1975b). Subsequent biochemical studies revealed that actin filaments within the core are bundled through the action of villin-1 (VIL1), plastin-1 (PLS1, also known as fimbrin), espin (ESPN) and most recently characterized, mitotic spindle positioning (MISP) (Bartles et al., 1998; Bretscher and Weber, 1979a; Bretscher and Weber, 1980; Morales et al., 2022). Additionally, core actin bundles are linked to the overlying plasma membrane by the ezrin-radixin-moesin (ERM) family protein ezrin (EZR), myosin-1a (MYO1A), and myosin-6 (MYO6)(Berryman et al., 1993; Bretscher, 1983; Hegan et al., 2012; Howe and Mooseker, 1983), which collectively provide long-term structural stability and prevent individual protrusions from fusing with their neighbors (Casaletto et al., 2011; Hegan et al., 2012; Tyska et al., 2005).

Long-standing hypotheses on how microvilli form during differentiation were inspired by TEM images that revealed an electron dense plaque at the distal ends of these protrusions (Mooseker and Tilney, 1975a); similar features were eventually found at the distal ends of stereocilia and filopodia as well (Rzadzinska et al., 2004; Svitkina et al., 2003). Situated between the plasma membrane and the barbed ends of core bundle actin filaments, factors in this complex would be well positioned to regulate actin monomer incorporation and thus, protrusion growth (Mooseker and Tilney, 1975b; Tilney and Cardell, 1970). Consistent with this proposal, proteins that localize to the distal tip compartment have been implicated in protrusion elongation in several investigations. In the context of microvilli, one example is Brain-Specific Angiogenesis

Inhibitor 1-Associated Protein 2-Like Protein 1 (BAIAP2L1, also known as insulin receptor tyrosine kinase substrate) (Postema et al., 2018b). In addition to its N-terminal I-BAR domain, BAIAP2L1 contains a central SH3 domain, and a WH2 domain that binds to actin (Millard et al., 2007; Postema et al., 2018b; Yamagishi et al., 2004). In live cells, BAIAP2L1 tracks the ends of growing protrusions and knockdown of BAIAP2L1 in human intestinal epithelial cells results in shorter microvilli, suggesting a function in protrusion elongation under normal conditions (Postema et al., 2018b).

Epidermal growth factor receptor pathway substrate 8 (EPS8) is another tip localized factor that stands out based on its remarkably specific enrichment at the distal ends of microvilli, stereocilia and filopodia (Avenarius et al., 2017; Chou et al., 2014; Croce et al., 2004; Manor et al., 2011a; Postema et al., 2018b; Zampini et al., 2011; Zwaenepoel et al., 2012). EPS8 contains an N-terminal phosphotyrosine binding domain (PTB), a src-homology 3 (SH3) binding domain, proline-rich regions that interacts with BAIAP2L1, and a C-terminal actin binding “effector region” (Disanza et al., 2004; Hertzog et al., 2010; Mongiovi et al., 1999; Uhlik et al., 2005). Motifs in the actin binding region of EPS8 exhibit both filament bundling and capping activity *in vitro* (Hertzog et al., 2010), and studies in live cells indicate that these motifs do hold direct barbed end binding activity (Gaeta et al., 2021a). However, EPS8 loss-of-function experiments in a range of animal and cell culture models uniformly lead to shorter protrusions, suggesting that this factor promotes elongation rather than capping under normal conditions (Manor et al., 2011a; Tocchetti et al., 2010; Zampini et al., 2011). Additional data in favor of this proposal comes from recent studies of microvilli biogenesis, which

showed that new core actin bundles grow *de novo* and as “daughters” from the sides of pre-existing “mother” protrusions; in both cases, new bundles emerge from puncta marked by EPS8 and BAIAP2L1, which remain enriched on the distal ends of actively growing protrusions (Gaeta et al., 2021a). Finally, mutations in EPS8 that disrupt actin binding also impair the formation of EPS8 puncta, core bundle formation, and microvillar motility observed in these live imaging assays (Gaeta et al., 2021a; Meenderink et al., 2019).

Given the exquisitely specific tip localization of EPS8 and the mounting evidence of its involvement in protrusion elongation, we leveraged this factor to screen for new distal tip residents that might also hold the potential for controlling microvillar growth. Proteomic studies of isolated brush borders have contributed rich datasets on the molecular composition of the apical actin cytoskeleton, although conventional mudPIT approaches lack spatial resolution (McConnell et al., 2011a; Revenu et al., 2012; Yoshida et al., 2016). One promising method for defining local proteomes involves proximity labeling, which takes advantage of modified *E. coli* biotin ligases that non-specifically biotinylate surrounding proteins (Kim et al., 2016; Roux et al., 2012). By anchoring such a ligase to a protein of interest, neighboring proteins can be biotinylated, isolated, and then identified using mass spectrometry. As an example, biotin proximity labeling using the modified enzyme TurboID was recently used to identify proteins at the apical non centrosomal microtubule organizing center in the intestine of *C. elegans* (Sanchez et al., 2021).

In this study, we used EPS8 to spatially anchor the BioID2 biotin ligase (Kim et al., 2016) at the distal tips of microvilli in human intestinal epithelial cell lines. This strategy allowed us to identify the uncharacterized protein KIAA1671 as a new resident of brush border microvilli. KIAA1671 localizes to the base of the brush border in native intestinal tissue and polarized epithelial cell culture models, and dynamic actin-rich structures in non-epithelial cell types. In timelapse observations of microvilli biogenesis, we found that KIAA1671 localizes to sites of both *de novo* and daughter core bundle growth. We also observed that KIAA1671 initially colocalizes with EPS8 in diffraction-limited puncta, although once growth of a core bundle begins, these two factors separate with EPS8 tracking the elongating distal end and KIAA1671 remaining behind at the base of the structure. Collectively, these results suggest that KIAA1671 might cooperate with EPS8 and potentially other core bundle assembly factors to initiate the growth of new microvilli on the apical surface. These results highlight the utility of proximity labeling for identifying features of local proteomes, even when spatial proximity is transient. These findings might also hold implications for understanding how apical specializations are assembled in other epithelial contexts.

Results and Discussion

A BioID2 screen reveals new EPS8 proximal factors

To search for new distal tip residents that might function in microvilli biogenesis, we expressed variants of EPS8 tagged with the biotin ligase BioID2, in the Ls174T-W4 (W4) human intestinal epithelial cell line to enable biotin proximity labeling of EPS8 labeled microvilli tips. W4 cells were engineered to activate the STRADα/LKB1 pathway when treated with doxycycline, which in turn leads to polarity establishment and brush border formation (Baas et al., 2004). W4 cells stably expressing EPS8-S-BioID2 (S = short linker, predicted labeling radius ~10 nm), EPS8-L-BioID2 (L = long linker, predicted labeling radius ~25 nm) (Kim et al., 2014; Kim et al., 2016) or myc-BioID2 as an unanchored negative control, were incubated in biotin depleted media for ~48 hrs before induction of brush border formation and supplementation with 50 μM biotin overnight. The next day, tagged proteins were collected by streptavidin pulldown and then subject to mass spectrometry for identification (Figures 4-1 A and B). As EPS8 targets to the distal ends of microvilli, we expected that cells expressing BioID2 tagged EPS8 constructs would demonstrate higher levels of biotin incorporation in the brush border relative to cells expressing the myc-BioID2 control. Indeed, cells expressing the EPS8-S-BioID2 and EPS8-L-BioID2 constructs revealed extensive biotinylation in the brush border compared to controls, as detected by streptavidin staining (Figure 4-1 C). Western blotting for biotinylated proteins in whole cell lysates using a fluorescent streptavidin conjugate also confirmed biotin incorporation in all samples (Figure 4-1 D). Biotinylated proteins in these samples were subsequently captured by streptavidin

pulldown and then identified using mass spectrometry, which revealed over 280 hits across all three samples, 56 of which were unique to the EPS8-S-BioID2 and EPS8-L-BioID2 conditions. One of the most striking hits was the uncharacterized protein KIAA1671, which demonstrated elevated total spectral counts in EPS8-S-BioID2 and EPS8-L-BioID2 samples (Figure 4-1 E and F).

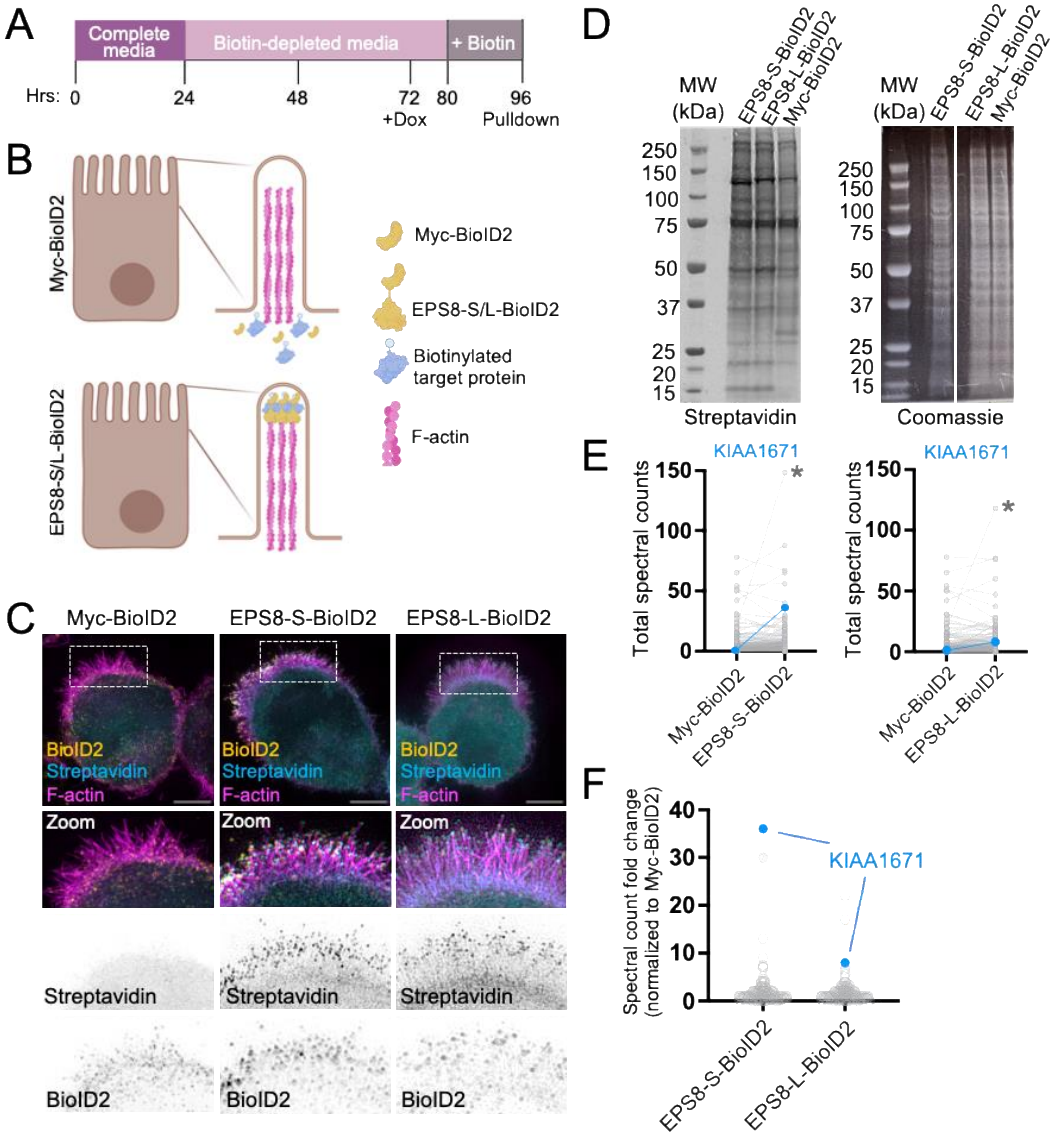

Figure 4-1. Utilizing biotin proximity labeling to probe for molecules involved in microvilli biogenesis. (A) Schematic timeline of W4 induction and biotin supplementation before streptavidin pulldown. Schematic created using BioRender. (B) Schematic representation of a W4 cell expressing the myc-BioID2 construct and EPS8-S/L-BioID2 constructs. Upon addition of 50 µM biotin to cell culture media overnight, the BioID2 construct will promiscuously biotinylate proteins within a ~10-25 nm radius. (C) Representative cells expressing either the myc-BioID2 control, EPS8-BioID2-HA or EPS8-13xL-BioID2-HA constructs (cyan) and stained with streptavin-488 (yellow) and phalloidin (magenta) to determine the extent of biotinylation in the brush border of W4 cells. (D) Biotinylated proteins from EPS8-S-BioID2-HA, EPS8-L-BioID2-HA or myc-BioID2 samples separated by SDS page and detected with a fluorescent streptavidin conjugate (left). Coomassie staining of previously stated samples to confirm equal total protein input for pulldown (right). (E) Plots comparing total spectral counts between proteins detected in myc-BioID2 vs EPS8-s-BioID2 or EPS8-L-BioID2 samples. Asterisks indicate enrichment of EPS8-S/L-BioID2 protein in samples (F) Fold enrichment of EPS8-S-BioID2 and EPS8-L-BioID2 samples over myc-BioID2 control. All images are displayed as maximum intensity projections.

Identification of KIAA1671 as a new resident of the brush border actin cytoskeleton

To explore the utility of the hits derived from our EPS8-anchored BioID2 screen, we decided to focus validation studies on the uncharacterized, KIAA1671 (1806 a.a., ~196 kDa). Although KIAA1671 was previously identified in large scale genomic and proteomic studies (Huttlin et al., 2017), its biological roles remain entirely unstudied. *In silico* domain analysis using IUPRED2A (Erdos and Dosztanyi, 2020; Meszaros et al., 2018) suggests KIAA1671 is largely disordered (Figure 4-2 A and B), although a tankyrase binding domain is annotated near the C-terminus.

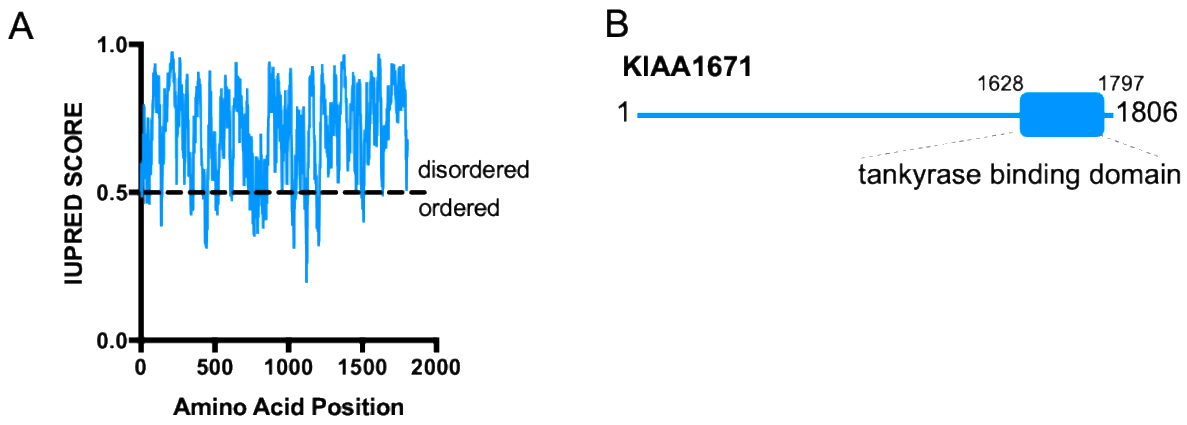

Figure 4-2. KIAA1671 sequence disorder prediction and domain diagram. (A) Prediction of sequence disorder using IUPRED2A. IUPRED scores over 0.5 predict disorder while values under 0.5 predict ordered residues. (B) Domain diagram of KIAA1671 highlighting its annotated tankyrase binding domain.

Further validation by immunofluorescence and construct expression revealed that KIAA1671 robustly targets to F-actin rich networks (Figure 4-3). In mouse small intestinal tissue, endogenous KIAA1671 localizes to the sub-apical compartment in villus enterocytes, where the rootlet ends of microvilli embed in the terminal web (Figure 4-3 A and C). We also noted apical staining of KIAA1671 in intestinal crypts (Figure 4-3 A, zoom 2). W4 cells also exhibited apical enrichment of EGFP-KIAA1671 (Figure 4-3 B, zoom1, and 4-3 C), and in this context a subpopulation of EGFP-KIAA1671 also localized to F-actin rich structures in the cytoplasm (Figure 4-3 B, zoom 2). Quantifying the fraction of overlap between the EGFP-KIAA1671 and phalloidin-568 signals in the cytoplasm of W4 cells revealed that the majority (66%) of total cytoplasmic EGFP-KIAA1671 signal merged with F-actin (Figure 4-3 D). Taken together, these results confirm that KIAA1671 is a *bona fide* resident of the brush border actin cytoskeleton in polarized epithelial cells.

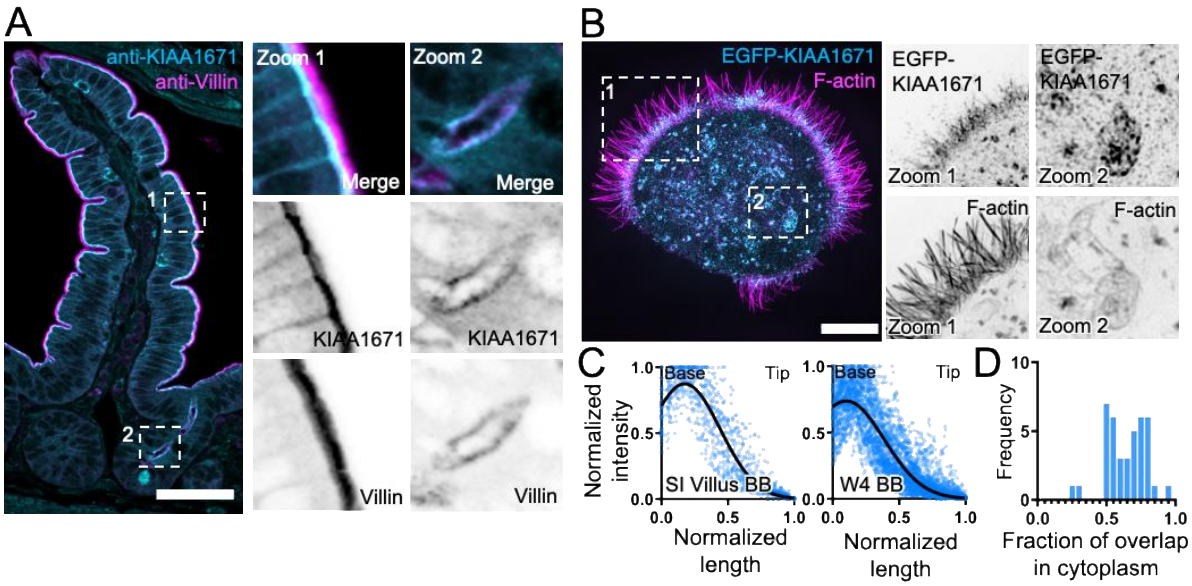

Figure 4-3. KIAA1671 is an uncharacterized protein that targets to the brush border cytoskeleton. (A) A paraffin embedded mouse small intestinal tissue section stained with anti-KIAA1671 (cyan) and anti-Villin (magenta) antibodies. Zoom 1 highlights apical staining on the villus, while Zoom 2 highlights apical staining in intestinal crypts. Scale bar = 50 µm (B) Representative W4 cell expressing an EGFP-KIAA1671 construct (cyan) and stained with phalloidin to mark F-actin (magenta). Zoom 1 highlights KIAA1671 at the base of the brush border, while Zoom 2 highlights KIAA1671 localization in the cytoplasm. (C) Line scans measuring anti-KIAA1671 (left) or EGFP-KIAA1671 (right) at the apical surface of intestinal tissue and W4 cells respectively. n = 63 line scans of villus intestinal tissue from one independent staining; n = 40 line scans of W4 brush borders from three independent experiments. (D) Quantification of the fraction of overlap between KIAA1671 and F-actin. Bars indicate the fraction of total KIAA1671 signal that overlaps with F-actin signal, n = 40 cells from three independent experiments. All images are displayed as maximum intensity projections.

KIAA1671 associates with dynamic F-actin networks in non-polarized cells

To determine if the localization of KIAA1671 to F-actin rich structures was unique to the highly specialized actin cytoskeleton found in polarized intestinal epithelial cells, we also expressed EGFP-KIAA1671 in the non-polarizing line B16F1. Transfection experiments revealed that EGFP-KIAA1671 localizes to F-actin positive linear features that labeled with a fluorescently tagged utrophin calponin homology (UtrCH) domain (mCherry-

UtrCH; Figure 3A and B). We also observed a prominent population of cytoplasmic puncta that were KIAA1671 and F-actin positive. Time-lapse imaging of this population using spinning disk confocal microscopy showed that KIAA1671/F-actin containing puncta are motile, suggesting these are sites of active actin polymerization. Analysis of puncta motion over a 45 sec window revealed that the trajectories of KIAA1671 and F-actin signal exhibited significant and sustained spatial overlap through time (Figure 4-4 C and D). Additionally, 2D analysis of KIAA1671 puncta that were associated with F-actin

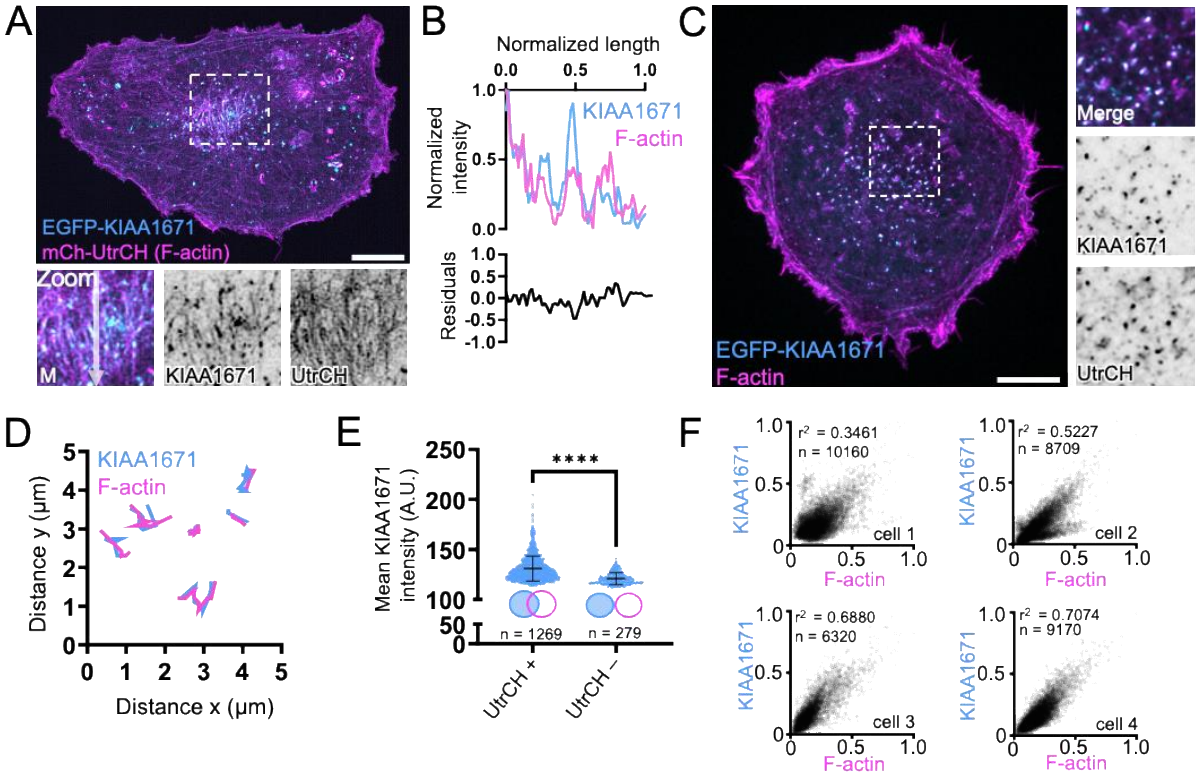

Figure 4-4. KIAA1671 overlaps with dynamic actin rich structures in unpolarized cells. (A) A representative B16F1 cell expressing EGFP-KIAA1671 and mCherry-UtrCH to mark F-actin. Zooms highlight linear actin features. (B) Line scan of linear features as highlighted in A, zoom. Scale bar = 10 μm. (C) B16F1 cell displaying cytoplasmic puncta of EGFP-KIAA1671 and mCherry-UtrCH. Scale bar = 10 μm (D) Representative trajectory analysis of 6 EGFP-KIAA1671 and mCherry-UtrCH puncta as represented in C. Traces measured at 5 sec intervals sampled over a 45 sec time period from a single imaging field. (E) 2D puncta analysis comparing mean EGFP-KIAA1671 intensities of puncta either associated (UtrCH +) or not associated (UtrCH-)

with UtrCH puncta. Plots are representative from a single cell over a 15 min imaging window. **** p<0.0001 using a two tailed Mann-Whitney test, n = 1269 UtrCH + puncta; n = 279 UtrCH – puncta. Plots show mean ± SD (F) 2D intensity correlations of EGFP-KIAA1671 puncta with mCherry-UtrCH from 6 cells over two independent experiments. p values were calculated from a two tailed test. All images are displayed as maximum intensity projections.

signal (Figure 3E, UtrCH +, n = 5,701 representative puncta from a single cell) demonstrated higher mean intensities compared to puncta that were not F-actin associated (Figure 3E, UtrCH - , n = 1,563 representative puncta from a single cell). Consistent with these analyses, when we correlated the intensities of many KIAA1671/F-actin puncta, we found a significant positive relationship between these two signals across multiple cells (Figure 4-4 F). Thus, higher levels of KIAA1671 are associated with higher levels of F-actin. KIAA1671's general colocalization with F-actin rich structures, co-migration with F-actin rich puncta, and positive correlation with F-actin content is suggestive of an actin binding protein that may promote, either directly or indirectly, the accumulation of actin polymer.

KIAA1671 and EPS8 transiently colocalize in puncta during microvilli biogenesis

As alluded to above, KIAA1671 localizes to F-actin networks in diverse contexts, although in the specific case of polarized epithelial cells, it localizes to the rootlet end of the microvillus, which is – paradoxically - the opposite end of the protrusion from where EPS8 resides. Given the significant spatial separation between these compartments (~1 μm or more), how might an EPS8-anchored biotin ligase encounter a protein near the basal ends of microvilli? One potential answer derives from the fact that microvilli are actively growing on the surface of W4 cells during the biotinylation step in our labeling

assay. Considering this point, EPS8 and KIAA1671 might only transiently colocalize at some point during the growth process. To explore this possibility, we turned to live imaging of microvillar biogenesis using the LLC-PK1-CL4 (CL4) cell culture model. We previously used this system to directly visualize the motility and growth of individual microvilli from an *en face* perspective (Gaeta et al., 2021a; Gaeta et al., 2021b; Meenderink et al., 2019). CL4 cells stably expressing EGFP-EPS8 and mCherry-ESPN, were transiently transfected with Halo-KIAA1671 (labeled with JFx646), and then subject to spinning disc confocal microscopy to enable visualization of microvilli biogenesis. Timelapse datasets revealed a population of KIAA1671 and EPS8 that are microvillus associated (Figure 4-5 A) as well as a separate population of colocalized punctate structures that lacked ESPN signal (Figure 4-5 B). Analyzing the motion of KIAA1671 and EPS8 puncta at 30 sec intervals over a period of 30 min revealed overlapping trajectories, suggesting these

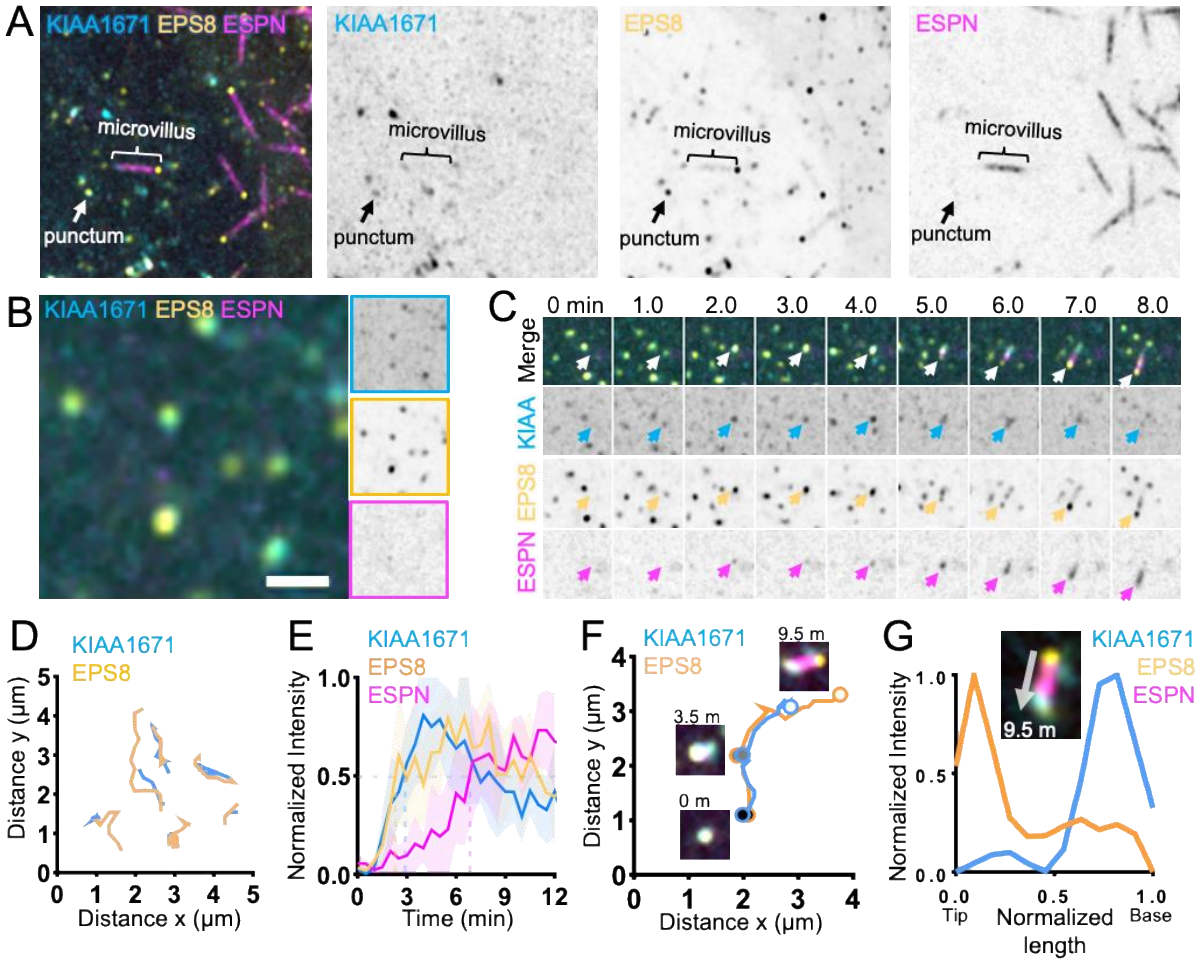

Figure 4-5. KIAA1671 and EPS8 puncta associate then separate during microvillus growth. (A) CL4 cell displaying microvilli as well as cytoplasmic KIAA1671 and EPS8 puncta in cells expressing Halo-KIAA1671, EGFP-EPS8 and mCherry-ESPN. Box width = 15 µm. (B) Representative image of EGFP-EPS8 and Halo-KIAA1671 puncta in CL4 cells. Single channel images are denoted by border outline in corresponding color (right). (C) Montage of a de novo microvillus growth event in a CL4 cell expressing EGFP-KIAA1671 (KIAA, cyan) EGFP-EPS8 (yellow), and mCherry-ESPN (magenta). Box width = 4 µm (D) Trajectory analysis of Halo-KIAA1671 and EGFP-EPS8 puncta as represented in B. Traces are measured at 30 s intervals sampled from a 30 min time period from a single imaging field. (E) Averaged normalized intensity vs. time curves representing 5 de novo microvilli growth events from the imaging experiment shown in C. Solid line represents mean and shaded area represents SD. (F) Trajectory analysis of Halo-KIAA1671 (cyan) and EGFP-EPS8 (yellow) during a de novo microvillus growth event. Large, shaded circles represent indicated timepoints during the trajectory. (G) Image of the 9.5 min timepoint indicated in F (top) with line scan demonstrating separation of the Halo-KIAA1671 and EGFP-EPS8 signals to opposite ends of the microvillus. All images are displayed as maximum intensity projections.

proteins are moving through the cytoplasm in complex (Figure 4-5 B and D). We also observed that KIAA1671 and EPS8 co-accumulate at future sites of *de novo* microvillar growth; in many of these cases, minutes later, ESPN positive actin bundles elongate from these puncta (Figure 4-5 C and E). Notably, as these core bundles elongate, EPS8 and KIAA1671 signals separate, with EPS8 marking the growing distal tip of the microvillus and KIAA1671 remaining behind at the proximal end (Figure 4-5 F and G).

In addition to *de novo* growth, new “daughter” microvilli also grow from pre-existing “mother” protrusions (Gaeta et al., 2021a), generating branched intermediates similar in appearance to the “forked” microvilli observed on the surface of diverse epithelial tissues (Tilney and Cardell, 1970; Zhu et al., 2022). Careful inspection of our timelapse datasets revealed that EGFP-KIAA1671 localizes at the basal end of a mother microvillus (marked by mCherry-ESPN) in the minutes leading up to daughter formation (Figure 4-6 A and B). Previous studies established that EPS8 marks the site of new daughter growth from an established mother (Gaeta et al., 2021a). Consistent with this, KIAA1671 and EPS8 are both found at base of nascent mother protrusion before elongation of a daughter microvillus begins (Figure 4-6 C). Indeed, colocalization map analysis of the 1-minute timepoint in Figure 4-6 A shows that prior to daughter core bundle elongation, KIAA1671 and EPS8 signals exhibit strong colocalization at the base of the microvillus (Figure 4-6 D and E).

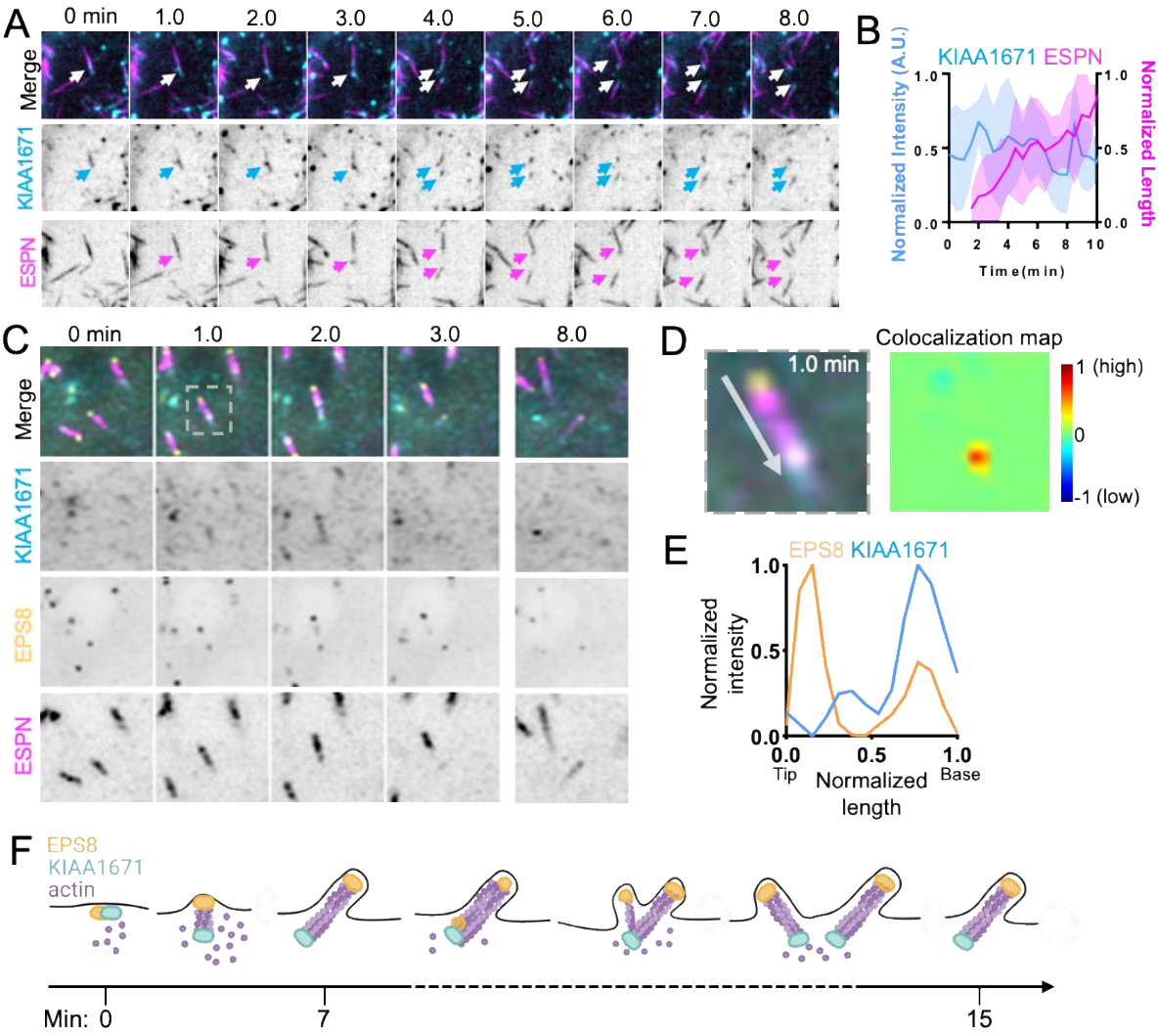

Figure 4-6. KIAA1671 and EPS8 puncta overlap during daughter microvillus growth. (A) Representative montage of daughter microvillus growth event. Box width = 9 µm. (B) Quantification of EGFP-KIAA1671 intensity and microvilli length versus time of daughter growth events. n = 12 daughter growth events from 7 cells over two independent experiments. (C) Montage of a daughter microvillus growth event in CL4 cells expressing Halo-KIAA1671, EGFP-EPS8 and mCherry-ESPN. Box width = 5 µm (D) Zoom of the 1 min timepoint in C (left), with colocalization heat map analysis (right). Warmer colors on heat map represent a higher degree of colocalization, while cooler colors represent a low degree of colocalization. (E) Line scan of zoom shown in D. All images are displayed as maximum intensity projections (F) Schematic of both de novo and daughter microvillus growth illustrating KIAA1671 and EPS8 together at early stages of de novo growth, followed by separation as the microvillus matures. During daughter growth KIAA1671 and EPS8 mark spots of new bundle formation on the mother bundle. As the new daughter bundle grows, EPS8 remains at the distal tip while KIAA1671 stays at the base of the microvillus. Schematic created using BioRender.

Collectively, these timelapse observations show that KIAA1671 and EPS8 transiently colocalize in puncta at the earliest stages of microvillar growth, which provides a likely explanation for the biotinylation of KIAA1671 in our EPS8 anchored proximity labeling screen.

Using a proximity labeling approach, we identified the previously uncharacterized protein KIAA1671 as a *bona fide* resident of the brush border actin cytoskeleton. In native intestinal epithelial cells, KIAA1671 localizes to the base of microvilli in the subapical terminal web, and expression studies in culture models also indicate that this factor localizes to dynamic actin networks independent of the cellular context. However, we were presented with a paradox when we considered the localization of KIAA1671 relative to EPS8, which was used to anchor the BioID2 moiety in our screen. EPS8 localizes to the distal tips while KIAA1671 is found at the base of microvilli, separated by a distance of at least 1 µm, outside the predicted range of proximity labeling (~25 nm using the long linker). We employed live cell imaging to investigate whether the interaction between EPS8 and KIAA1671 might be transient in nature. Indeed, timelapse datasets revealed that EPS8 and KIAA1671 do associate in dynamic puncta with a subset giving rise to microvilli *de novo*. Remarkably, as the core actin bundle begins to elongate, the EPS8 and KIAA1671 signals separate with EPS8 occupying the elongating distal end as expected, and KIAA1671 remaining behind at the base of the protrusion. The end result is a microvillus with EPS8 marking the distal end and KIAA1671 highlighting the rootlet, a distribution consistent with what we observe in fixed intestinal epithelial tissue and cell culture models at steady state. We also observed a

similar pattern of initial transient colocalization followed by spatial separation in instances of mother-daughter growth. Thus, using spatially targeted proteomic screen, we identified a novel factor that may cooperate with EPS8 during the early stages of microvilli biogenesis.

Do our results implicate KIAA1671 as a binding partner of EPS8? Biotin proximity labeling in conjunction with live cell imaging of KIAA1671 and EPS8 during microvilli biogenesis suggest these proteins transiently associate in a complex. However, neither of these techniques imply direct protein-protein interaction, and thus further biochemical characterization is necessary to determine whether EPS8 and KIAA1671 are binding partners. In terms of possible structural mechanisms that could mediate direct binding, EPS8 contains a central SH3 domain which mediate protein:protein interactions by binding to proline-rich sequences in interacting proteins. The SH3 domain of EPS8 binds to PxxDY motifs instead of canonical PxxP motifs (Mongiovi et al., 1999), and primary sequence analysis of KIAA1671 indicates the presence of multiple proline-rich stretches. Such regions are common features of intrinsically disordered proteins (Theillet et al., 2013), presenting a possibility for future studies aimed toward characterizing KIAA1671/EPS8 interactions. Independent of the details of association, our data do indicate that KIAA1671 and EPS8 cooperate early in this process core bundle assembly. Interestingly, transmission electron micrographs of microvillus re-growth events in native tissue revealed electron dense plaques at the apical surface of intestinal cells, which were hypothesized to be microvillus pre-cursors (Tilney and Cardell, 1970). KIAA1671 and EPS8 do colocalize in cytoplasmic puncta that lack

ESPN signal, and it is tempting to speculate that these features correspond to electron dense plaques noted in those classic ultrastructural studies.

How might KIAA1671 impact the dynamics of the actin cytoskeleton? Bioinformatics analysis identified a tankyrase binding protein motif at the C-terminus of KIAA1671. Intriguingly, related tankyrase binding domain containing protein TNKS1BP1 (also known as TAB182) has been shown to associate with actin, and through its C-terminus directly binds the CAPZA2 subunit of heterodimeric capping protein (CP) (Ohishi et al., 2017). Local alignment of KIAA1671 and TNKS1BP1 indicates that its CAPZA2 binding region a.a. 1,543–1,635 displays 32.4% identity and 51% similarity with KIAA1671 a.a. 1617-1711 (Ohishi et al., 2017) (4-7, top) and previous large scale affinity purification proteomic studies also detected an interaction between KIAA1671 and CAPZA2 (Huttlin et al., 2021). What are the functional implications of an interaction with CAPZA2? CP binds to the barbed ends of actin filaments with sub-nanomolar affinity, potently inhibiting incorporation of new monomers (Wear et al., 2003). However, several factors tune CP activity using steric or allosteric mechanisms. Notably, CARMIL family proteins (including CKIP-1, WASHCAP, CD2AP, CapZip and Twinfilin) allosterically reduce CP affinity for the filament barbed end. Direct binding of these proteins to CP is mediated by a capping protein interaction (CPI) motif (Bruck et al., 2006; Hernandez-Valladares et al., 2010; McConnell et al., 2020). Interestingly, local alignment of the CARMIL1 CPI (a.a. 958-1082) indicates weak identity with KIAA1671 a.a. 1013-1137 (4-7, bottom), leading to the intriguing possibility that this factor might hold the potential to regulate CP activity and drive actin polymerization during microvillar growth.

Figure 4-7. Sequence alignments of KIAA1671 with TNKS1BP1 and CARMIL1. Top EMBOSS Water local sequence alignment of human KIAA1671 (NP_001138678.1) and human TNKS1BP1 (Accession NP_203754.2) using a BLOSUM62 matrix. Identical residues are highlighted in magenta, similar residues are highlighted in black, and not similar amino acids are shown in light gray. Bottom EMBOSS Water local sequence alignment of human KIAA1671 (NP_001138678.1) and human CARMIL1 (also known as F-actin-uncapping protein LRRC16A; NP_060110.4) using a BLOSUM62 matrix. The CARMIL annotated CPI consensus motif is highlighted in the red box. Identical residues are highlighted in magenta, similar residues are highlighted in black, and not similar amino acids are shown in light gray.

Additional insight on the function of KIAA1671 might also be derived from its dynamic localization during microvilli growth. As alluded to above, KIAA1671 initially colocalizes with EPS8, but as the nascent core bundle begins to elongate, these two factors separate and become enriched at opposite ends. Such a dynamic pattern is reminiscent of the behavior of the actin nucleator APC and the formin mDia1, as observed *in vitro*

(Breitsprecher et al., 2012). APC and mDia1 initially colocalize in puncta that represent a nucleation complex, but as the associated actin filament begins to elongate, APC remains behind at the pointed end while mDia1 tracks the elongating barbed end (Breitsprecher et al., 2012). In this case, the persistent pointed end localization of APC is a tell-tale sign of its activity as a templating filament nucleator. Although the current level of annotation on KIAA1671 does not point to canonical actin monomer-binding motifs, which would be needed to underpin nucleation activity, this remains an open functional hypothesis that could be tested in future cell biological studies.

CHAPTER V.

FUTURE DIRECTIONS AND CONCLUSION

EPS8 may contain a profilin binding PR region

While EPS8 is implicated in protrusion elongation in both microvilli and stereocilia, its exact mechanism of action remains unclear. *In vitro* data suggests EPS8 possesses both F-actin capping and bundling activity (Disanza et al., 2004; Hertzog et al., 2010), however these functions are at odds with its specific distal tip localization and knockdown phenotype. Canonical F-actin bundling proteins found in microvilli, filopodia and stereocilia such as villin, fimbrin, espin, MISP, and fascin all localize along the length of the protrusion. Additionally, knockdown of a protein that caps the barbed ends of actin filaments to prevent elongation would be predicted to increase filament length, however, loss of EPS8 in both tissue and cell culture contexts leads to shortening of both microvilli and stereocilia (Manor et al., 2011a; Postema et al., 2018b; Tocchetti et al., 2010; Zampini et al., 2011). EPS8 contains proline-rich regions (PRRs) that mediate interactions with SH3 domains of other binding partners, including IRTKS and IRSP53 (Disanza et al., 2006; Postema et al., 2018b). PRRs are also found to mediate binding of profilin actin in molecules that promote actin filament elongation, such as ENA/VASP family proteins and formins (Chang et al., 1997; Ferron et al., 2007; Lambrechts et al., 2000). Interestingly, alignment of EPS8 with VASP, ENAH, EVL and the formin FHOD1 reveal significant overlap in their PRRs (Figure 5-1). Interestingly, the EPS8 PRR overlap with VASP corresponds with the region shown to mediate profilin-actin binding, with the actin monomer being transferred to its GAB module and subsequently

incorporated into the barbed ends (Ferron et al., 2007). Additionally, overlap with FHOD1 corresponds to its FH1 domain, with the FH1 domain implicated in binding profilin actin monomers that are directly and processively incorporated into the barbed ends (Kovar et al., 2006; Paul and Pollard, 2008). This sequence conservation suggests

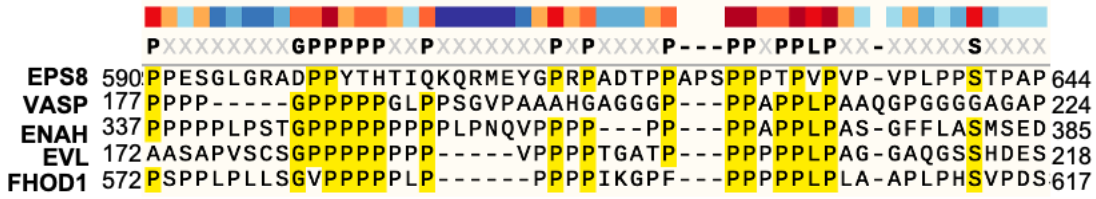

Figure 5-1. Amino acid alignment of EPS8 and ENA/VASP proteins and formin FHOD1. Top heat map shows extent of amino acid identity. Warmer colors = high identity, cooler colors = low identity. For EPS8 these amino acids constitute a PRR adjacent to the AB domain.

the corresponding EPS8 PRR (EPS8 PR4) could be involved in recruitment of profilin-actin monomers. Interestingly, the EPS8 PR4 region is directly adjacent to its c-terminal actin binding domain, as profilin binding regions have been shown to be adjacent to actin binding modules in other proteins (Ferron et al., 2007). Additionally, as previous studies indicate IRTKS elongates microvilli in a WH2 domain dependent manner involving EPS8 (Postema et al., 2018b), it is plausible that EPS8 could promote microvilli actin filament elongation through recruitment of profilin-actin, which can then be incorporated into barbed ends through the IRTKS WH2 domain.

We began our investigation of the EPS8 PR4 region by probing whether EPS8 interacts with profilin through a pulldown assay. EGFP-EPS8 was over expressed in non-epithelial cells and then pulled down with GFP-trap magnetic beads. Samples were

separated by SDS page and then blotted for the presence of profilin-1. Our initial results did not indicate interaction of EPS8 and profilin, due to the absence of a profilin band in the EPS8 + pulldown lane. Further investigation should include a chemical cross-linking step during the pulldown to capture the potential transient, low affinity interaction between EPS8 and profilin.

To begin our cellular investigation into the role of the EPS8 PR4 region in microvilli biogenesis, we overexpressed an EPS8ΔPR4 construct in W4 cells. Preliminary data shows that some cells exhibited distal tip targeting of EPS8ΔPR4 while others did not, with cells exhibiting distal tip targeting showing greater cellular intensities of EGFP-EPS8ΔPR4 on average (Figure 5-2). These results suggest that the PR4 region may partially contribute to distal tip enrichment of EPS8. Whether the lack of proper targeting is due to decreased interaction with profilin remains to be explored, as it is possible EPS8 is binding other tip complex proteins through this PRR.

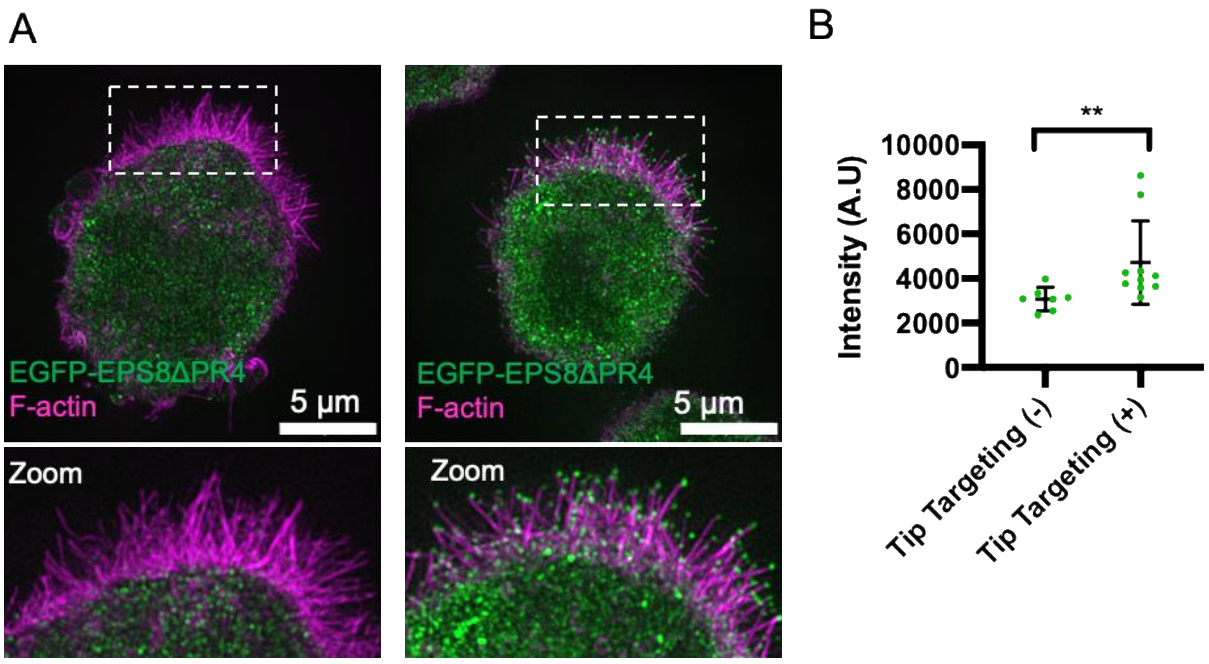

Figure 5-2. Expression of EGFP-EPS8ΔPR4 in W4 cells. (A) Examples of W4 cells expressing EGFP-EPS8ΔPR4 that do not exhibit tip targeting (left) vs cells that exhibit tip targeting (right). (B) Quantification of cytosolic EGFP-EPS8ΔPR4 intensity as a proxy for construct expression level. **p = 0.0031, two tailed t-test.

EPS8 membrane binding potential

Microvilli collapse is typified by loss of membrane wrapping and EPS8/IRTKS at the distal tips of microvilli ((Gaeta et al., 2021a), chapter III). These findings suggest that these proteins are somehow linked to the plasma membrane. IRTKS contains a bona fide membrane binding I-BAR domain, however, whether EPS8 directly binds to membrane has yet to be established, although its localization and sequence features suggest this is a possibility. EPS8 contains a Dab-like PTB domain, with other proteins containing this domain exhibiting direct membrane binding to PIP2 (Uhlik et al., 2005). Understanding whether EPS8 can bind to membrane would inform its functional role as well as its exact targeting mechanism. Structure function studies showed that EPS8 distal tip localization is only partially dependent on actin binding, as an EPS8 mutant lacking its c-terminal actin binding region retains some distal tip localization ((Gaeta et al., 2021a), Figure 3-5), suggesting N-terminal motifs, including its PTB domain may contribute to its distal tip localization. Unpublished data indicates that the region containing the PTB domain (EPS8 1-202) is insufficient for distal tip targeting, however when the N-terminal half of EPS8 was deleted (EPS8 415-822), distal tip targeting was also hindered, with similar results found in stereocilia (Figure 5-3, (Manor et al., 2011a)).

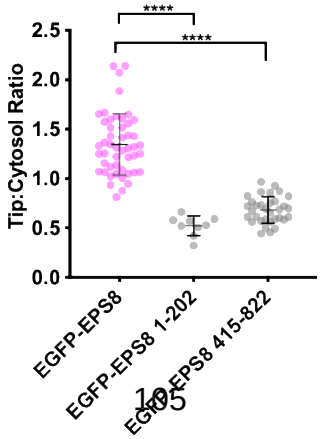

Figure 5-3. Deletion of EPS8 N-terminal residues hinders distal tip targeting. Extent of EPS8 distal tip targeting assessed by EPS8 tip:cytosolic ratios. ****p<0.0001 by Kruskal Wallis. Mutants are compared to WT EPS8 data published in (Gaeta et al., 2021a), and Figure 3-5 B and C.

Thus, further investigation of EPS8 distal tip targeting and membrane binding potential is warranted. To assay for membrane binding, purified EPS8 can be incubated on membrane strips spotted with phosphoinositides and other lipid species (PIP strips, Echelon Biosciences). If membrane binding is detected, EPS8 mutant constructs should be further investigated to determine the domains responsible for membrane binding. We propose assaying the following EPS8 mutant constructs: WT EPS8, EPS8 54-202 (PTB), and EPS8 203-822 (ΔPTB). Incubation of the EPS8 isolated PTB domain or an EPS8 construct lacking the PTB domain would further indicate whether membrane binding can be mediated by this domain. Additionally, these studies in combination with PIP dynamics during microvilli growth will further elucidate the sequence events leading to microvilli biogenesis and give insight as to how cells spatially regulate sites of microvillus growth. We propose below further study of phosphoinositides during microvillus growth and apical morphogenesis.

Phosphoinositides and microvillus growth

Phosphoinositides are minor lipid species which play significant roles in signal transduction, cell polarity and membrane protrusion (Balla, 2013; Falkenburger et al., 2010). Biochemically, phosphoinositides are glycerophospholipids that contain an inositol head group, which can be phosphorylated at hydroxyl groups at the 3,4 and 5

positions of the inositol ring (Falkenburger et al., 2010). Protein binding to different phosphoinositide species thus potentiates signaling from membranes. For instance, generation of distinct phosphoinositides is implicated information of phagocytic and macropinocytic cups, membrane protrusions that require coordination of small GTPases and cytoskeletal factors, as well as in the formation of filopodia (Jacquemet et al., 2019; Swanson, 2014). Additionally, one of the defining features of polarized epithelial cells is the spatial distribution of phosphoinositides, with phosphatidylinositol-3,4,5 trisphosphate (PI(3,4,5)P3) restricted to the basolateral plasma membrane, while phosphatidylinositol-4,5 bisphosphate (PI(4,5)P2) defines the apical membrane (Gassama-Diagne et al., 2006). Indeed, microvilli resident proteins also mediate their interaction with the plasma membrane through phosphatidylinositol binding, including Myosin-1a, Ezrin, IRTKS and potentially EPS8, as discussed previously. Whether local phosphoinositides generation plays a role in the biogenesis of microvilli is less understood. Expression of fluorescent PIP2 sensors allows for live imaging of phosphoinositide dynamics (Halet, 2005). Thus, to begin to understand the role of PIP2 during microvilli biogenesis, we expressed GFP tagged pleckstrin homology (PH) domain of phospholipase C delta (PLCδ), which is a reporter for PI(4,5)P2. Preliminary data suggests EGFP-PLCδ-PH indeed targets to the apical membrane in CL4 cells (Figure 5-4). Additionally, EGFP-PLCδ-PH was detected at sites of both *de novo* and daughter microvillus growth (Figure 5-4), suggesting PI(4,5)P2 may be generated at local sites of protrusion formation. These results should be further validated by expression of the GFP-PLCδ-PH-R40L, a non-targeting mutant, to confirm that EGFP-

PLCδ-PH localization to sites of microvilli biogenesis is specific to its PI(4,5)P2 binding activity.

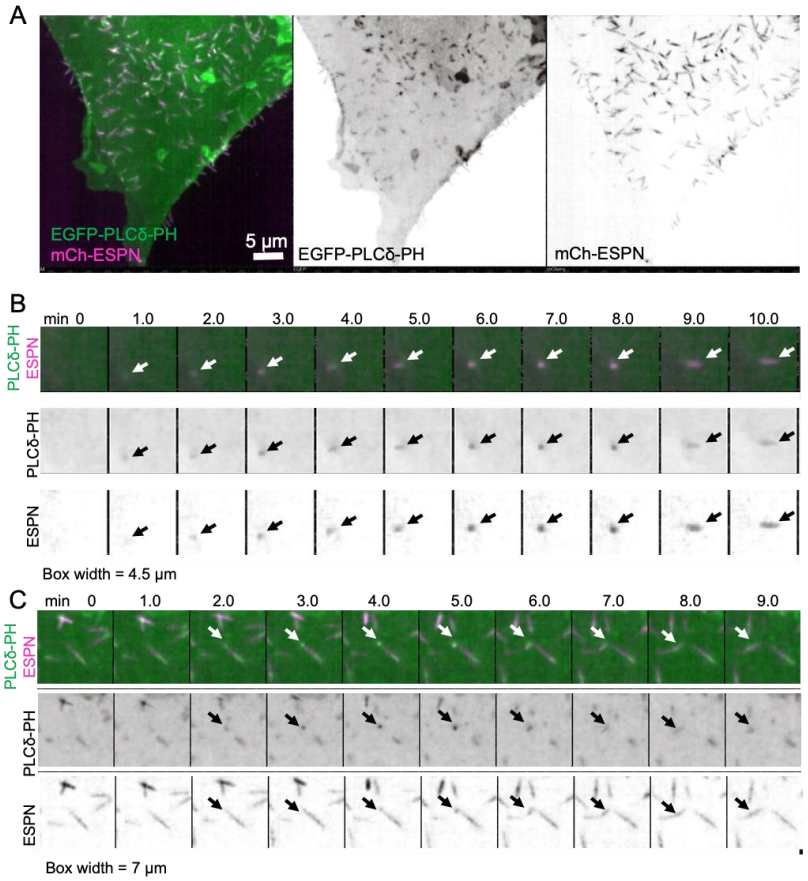

Figure 5-4. The PH domain of PLC-δ targets to sites of microvilli growth. (A) CL4 cell expressing EGFP-PLCδ-PH (B) Instance of EGFP-PLCδ-PH targeting during de novo microvillus growth. (C) Instance of EGFP-PLCδ-PH targeting during daughter microvillus growth.

EPS8 stoichiometry and molecular counting

One fundamental outstanding question in microvilli and stereocilia biogenesis is how the number of filaments per protrusion is determined, as discussed at the end of chapter III. In the case of microvilli, there are an estimated 20-40 actin filaments per protrusion. One hypothesis posits that proteins that localize to the distal tip compartment may allow the cell to “count” the number of filaments per protrusion. As EPS8 is at the tips of all

microvilli, binds directly to barbed ends, and serves to elongate microvilli, we propose it could function in determining the number of actin bundles per protrusion. Puncta intensity analysis of CL4 cells of cells overexpressing EGFP-EPS8 has revealed intensity distributions that are at least bimodal, and that puncta intensity increases with its lifetime, indicating EPS8 puncta undergo maturation during microvilli biogenesis ((Gaeta et al., 2021a), Figure 3-1). EPS8 has been shown to dimerize through its SH3 domain (Kishan et al., 1997), and *in vitro* studies suggest EPS8 binds F-actin with 1:1 stoichiometry (Hertzog et al., 2010), however whether EPS8 acts functionally as a dimer and binds 1:1 with actin filaments during microvilli biogenesis is still unknown. One way we propose to determine the number of EPS8 molecules at the tips of microvilli is to perform stepwise photobleaching analysis of EPS8 puncta. While this analysis can be performed in cells over-expressing GFP-tagged EPS8 molecules (example in Figure 5-5), expression of endogenous, untagged EPS8 could obscure exact counts. Thus, future studies should make use of cell lines with endogenously tagged EPS8, mediated through CRISPR knockin of GFP to the EPS8 N-terminus. Thus, back calculation of the number of photobleaching steps in intensity plots can determine the functional unit of EPS8 at the distal tips of microvilli. In addition to photobleaching experiments, EPS8 mouse KO models can be utilized to characterize the effect of EPS8 loss on the number of actin filaments per microvillus. EPS8 KO leads to shorter microvilli in the intestine (Tocchetti et al., 2010), however close characterization of actin bundle morphology has not been assessed. Thus, future studies should examine whether EPS8 KO leads to a change in the number of actin filaments per core bundle through comparison of WT intestinal microvillus cross sections with those of the EPS8 KO.

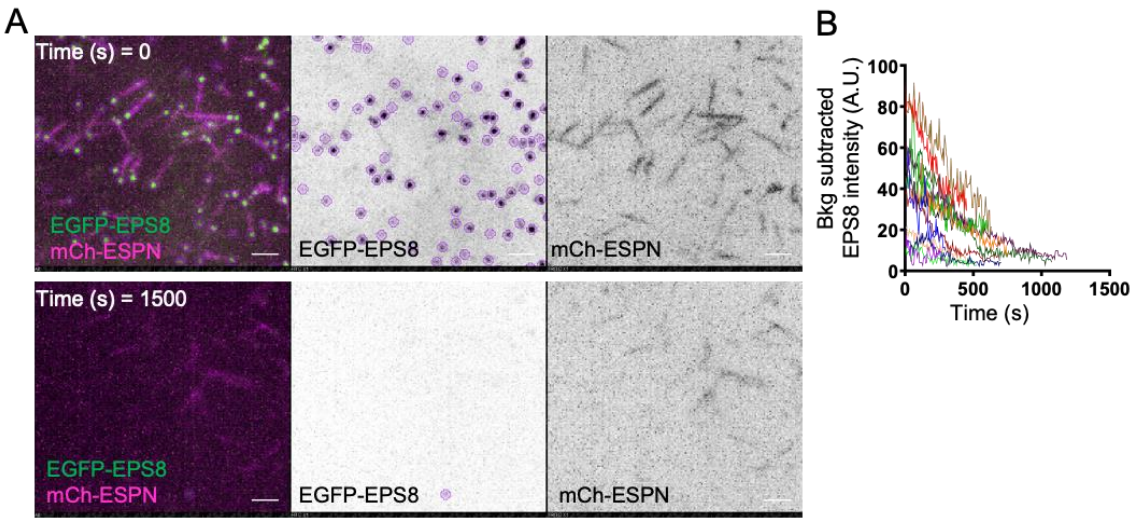

Figure 5-5. Example of microvillus associated EPS8 stepwise photobleaching. (A) CL4 cells expressing EGFP-EPS8 and mCherry-ESPN, subjected to continuous acquisition to promote fluorophore photobleaching. t = 0 (top), t = 1500s (bottom). (B) Representative background subtracted intensity traces of EGFP-EPS8 puncta over time.

Future studies of EPS8 proximal interactors

Using biotin proximity labeling, we have identified EPS8 proximal proteins in polarized epithelial cells, with the goal of further enhancing our understanding of microvilli biogenesis (Chapter IV). Our subsequent study primarily focused on one of the most enriched hits, the unidentified protein KIAA1671. However, other interesting hits arose from this screen, and their roles in microvilli biogenesis should be considered for future study, some of which have already been identified as components of the brush border (McConnell et al., 2011a). We used broadened criteria, exploring other hits that showed 2-fold enrichment in either the EPS-BioID2 or EPS8-13xL-BioID2 conditions compared to the myc-BioID2 control. Preliminary staining in mouse intestinal tissue and exploration of the human protein atlas database (https://www.proteinatlas.org/) was conducted to verify whether additional hits warrant future study for their potential role in

microvilli biogenesis. We thus propose future routes of experimentation for KIAA1671 as well as present preliminary investigations and thoughts on the role of Annexin A2, EPS8L2, zonula occludins-1 (ZO-1), and APC in brush border morphogenesis.

KIAA1671

Sequence analysis reveals KIAA1671 is a primarily disordered protein (Figure 4-2). Interestingly, a subset of intrinsically disordered proteins that take part in multivalent interactions are implicated in phase separation and protein condensate formation (Martin and Holehouse, 2020). Phase separated protein condensates constitute membraneless compartments that can serve as concentrated hubs for biochemical reactions, such as nucleic acid-protein interactions in heterochromatin, and nucleation of microtubules in pericentriolar material (Larson et al., 2017; Li et al., 2018; Woodruff et al., 2017). Indeed, stereocilia distal tip complex proteins Whirlin, Myosin XVa and EPS8 undergo phase separation *in vitro*, suggesting phase separation could play a role in stereocilia morphogenesis, and potentially in the formation distal tip complexes such as those in microvilli and filopodia (Lin et al., 2021). One of the hallmark indicators for a protein undergoing phase separation is the presence of liquid like droplets that undergo fusion, visualized by fluorescence microscopy (Brangwynne et al., 2009). Overexpression of EGFP-KIAA1671 in CL4 cells revealed both a microvillus associated and punctate population (Figure 5-6 A, arrows), with the punctate population of EGFP-KIAA1671 exhibiting fusion behavior (Figure 5-6 B). This fusion behavior in combination with its primarily disordered protein structure suggests KIAA1671 may be undergoing phase separation. To further probe whether KIAA1671 may be forming membraneless condensates, we co-stained W4 cells expressing EGFP-KIAA1671 with the membrane

marker FM-464 to determine whether these puncta are membrane associated. We noted several examples of EGFP-KIAA1671 puncta that did not overlap with the FM464 membrane dye, suggesting that KIAA1671 puncta form are not enveloped by membrane (Figure 5-6 C). Further study is warranted to determine whether this liquid like behavior occurs at endogenous concentrations or is merely a result of protein overexpression. Thus, endogenously tagged cell lines of KIAA1671 cells will be critical tools for making this determination.

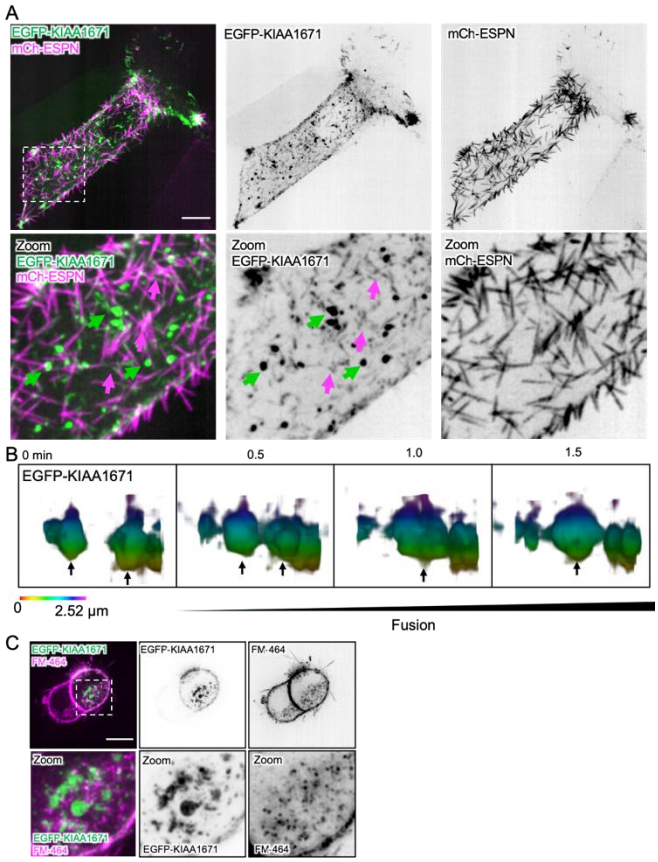

Figure 5-6. KIAA1671 puncta exhibit condensate-like behavior. (A) Overexpression of EGFP-KIAA1671 in CL4 cells. Microvilli actin bundles are marked by mCherry-ESPN. Green arrows denote non-microvilli associated KIAA1671 droplets, and green arrows denote ESPN associated KIAA1671. (B) 3D rendering of EGFP-KIAA1671 puncta undergoing fusion. (C) Overexpression of EGFP-KIAA1671 in W4 cells co stained with FM-464.

AnnexinA2

Annexin A2 is a Ca^{2+} binding protein that also interacts with PI(4,5)P2 and actin, and is implicated in cell polarization and endocytosis (Grieve et al., 2012). These membrane and actin binding properties position it as a potential regulator of brush border morphogenesis. Intestinal staining of Annexin A2 in mouse intestinal tissue shows localization to the subapical terminal web in mouse small intestinal tissue in both the crypt and the villus (Figure 5-7 A and B), as well as the base of the brush border in polarized W4 cells (Figure 5-7 C and D). This localization is anticipated given its interaction with PI(4,5)P2 and implication in polarization and endocytosis. While its function as an actin binding protein is unclear, it is tempting to speculate that Annexin A2 may function to link the brush border membrane to the underlying actin cores, or regulate endocytosis, which occurs at the base between adjacent microvilli.

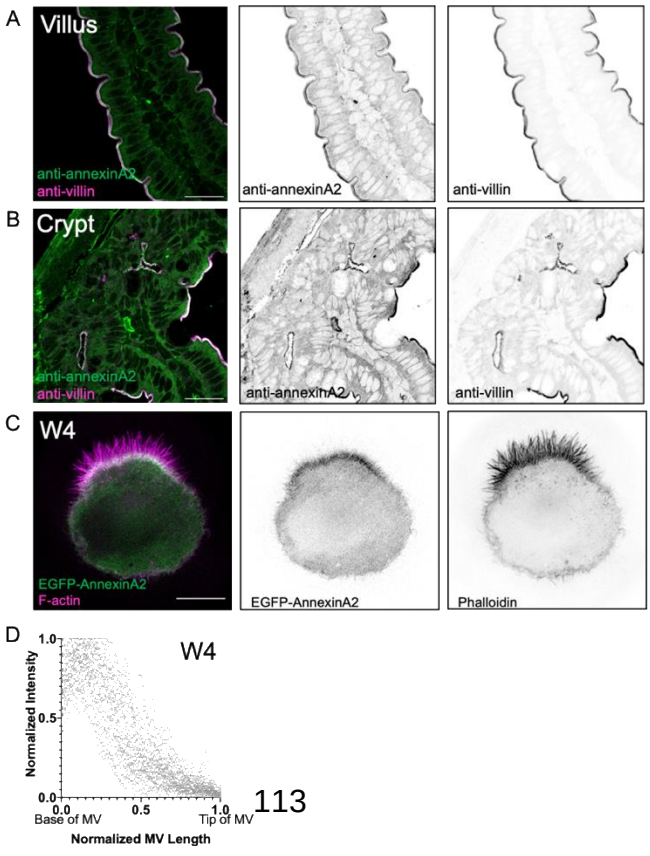

Figure 5-6. Annexin A2 localizes to the apical surface of intestinal epithelial cells. Paraffin embedded tissue. Anti-Annexin A2 (green), anti-villin (magenta)
Endogenous staining of Annexin A2 in mouse intestinal tissue, focusing on the villus (A), and the crypt region (B). (C) Expression of EGFP-Annexin A2 in W4 cells. (D) Line scan analysis of Annexin A2 along the brush border axis in W4 cells. Data from C and D were collected by Julissa Burgos.

To test this, knockout mouse models in combination with TEM could be used to determine if loss of Annexin A2 affects brush border membrane coverage or leads to cytoskeletal defects, similar to Myosin 1-a, Myosin -6 and Pacsin-2 (Hegan et al., 2012; Postema et al., 2019; Tyska et al., 2005). Additionally, as Annexin A2 resides at the opposite end of the microvillus from EPS8, it is possible that EPS8 and Annexin A2 could interact early during the biogenesis of microvilli, similar to EPS8 and KIAA1671. Unfortunately, attempts at imaging AnnexinA2 during microvilli growth using CL4 cells were not fruitful, as EGFP-AnnexinA2 displayed diffuse localization in these cells. Thus, future studies aimed at understanding Annexin A2 at early stages of microvilli biogenesis should utilize endogenous tagging or imaging in human $Caco2_{BBE}$ cells, which may better express Annexin A2.

EPS8L2

EPS8L2 is an EPS8 family protein that targets to the distal tips of stereocilia and has been implicated in stereocilia maintenance and elongation (Furness et al., 2013). However, whether it is involved in microvilli biogenesis is less clear, as previous proteomic studies did not detect EPS8L2 in brush border fractions (McConnell et al., 2011b), although RNA expression is detected in the gut of mouse embryos

(Offenhauser et al., 2004). Staining of mouse intestinal tissue demonstrated EPS8L2 localizes to both the tips and the base of microvilli in mature enterocytes (Figure 5-7). However, overexpression of EGFP-EPS8L2 in W4 cells did not indicate robust distal tip localization (unpublished results). Despite sequence similarity, EPS8 and EPS8L2 have similar but distinct localizations and knockdown phenotypes in stereocilia (Furness et al., 2013), with EPS8 KO mice being profoundly deaf, and EPS8L2 KO mice developing gradual deafness. Additionally, EPS8 displays a preference for the tips of the tallest rows of stereocilia, while EPS8L2 is localized primarily to the shorter rows in the cochlea (Furness et al., 2013). As EPS8L2 is also at the tips of microvilli in intestinal tissue, it is possible EPS8 and EPS8L2 could have overlapping functions in the intestine. EPS8 KO mice exhibit shortened microvilli, however the brush border still forms, indicating a degree of compensation. Future studies should explore whether EPS8L2 can compensate for the loss of EPS8 in mouse intestinal tissue. Additionally, it would be of interest to determine whether EPS8 and EPS8L2 are in complex before and during the growth of microvilli using our CL4 cell culture model, lending insight into their respective roles during apical morphogenesis.

Figure 5-7. EPS8L2 localizes to the tips and the base of microvilli in mouse intestinal tissue. Paraffin embedded tissue. Anti-EPS8L2 (green), anti-villin (magenta).

ZO-1

ZO-1 is a tight junctional protein and marker of the apical surface of epithelial cells, that binds actin and an array of other proteins (Kuo et al., 2022). Due to its multiple interacting partners, it is hypothesized ZO-1 may play a scaffolding role. Thus, it was intriguing to find ZO-1 enriched in EPS8-S/L-BioID2 samples. ZO-1 targets to the subapical cellular junctions beneath the brush border (Odenwald et al., 2018), which contrasts with EPS8 targeting to the distal tips of microvilli. Intriguingly, expression of EGFP-ZO-1 in CL4 cells demonstrated an expected population around the cell periphery, however there was also a population of ZO-1 associated with nascent, actively growing microvilli in the middle of the cell (Figure 5-8). This data presents an exciting possibility that ZO-1 may play a role in the early biogenesis of microvilli. Although ZO-1 is canonically thought of as a tight junctional protein, with primary roles in barrier function, non-canonical roles of ZO-1 have recently been explored, such as its involvement in mitotic spindle orientation (Kuo et al., 2021). As advances in live cell imaging allow for a more wholistic view of protein activity, it will be fascinating to further explore the extent to which ZO-1 is “noncanonically” involved in the biogenesis of microvilli and which domains enable this activity.

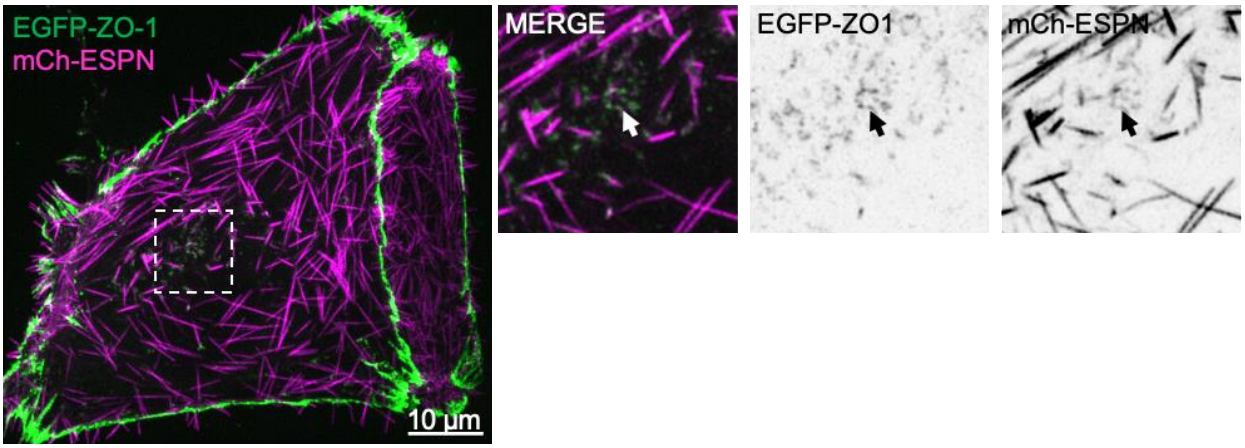

Figure 5-8. ZO-1 localizes to sites of nascent microvilli growth. CL4 cell expressing EGFP-ZO-1 and mCherry-ESPN. Dashed box represents zoom. Arrows denote nascent microvilli. Data acquired by Caroline Cencer.

APC

APC is a well-studied mediator of the Wnt/β-catenin signaling pathway, known for its role in the β-catenin "destruction complex" (Bienz, 2002). Significantly, APC inactivating mutations account for an overwhelming majority of colorectal cancers (Nagase and Nakamura, 1993). Aside from its role in the Wnt pathway, APC has been implicated as an actin filament nucleator, and binds to the formin mDia1 early in actin filament assembly (Breitsprecher et al., 2012; Okada et al., 2010). During actin filament elongation, APC remains associated with the pointed ends, while mDia1 promotes filament elongation and the barbed end, in a "rocket launcher" mechanism (Breitsprecher et al., 2012). Indeed, we drew parallels between APC/mDia1 mediated actin filament polymerization as relevant to the separation of KIAA1671/EPS8 during microvillus elongation, speculating KIAA1671 may possess nucleating activity (chapter IV). As APC is a bona finde actin nucleator, we entertain the possibility that APC could also be nucleating microvilli actin bundles. Interestingly, human protein atlas (HPA)

staining suggests APC could be enriched in the subapical terminal web (Figure 5-9, zoom 2, green arrow). Thus, future studies should focus on validation of APC apical localization in mouse intestinal tissue and cell culture models, as a first step in exploring the nucleating potential of microvilli actin bundles by APC.

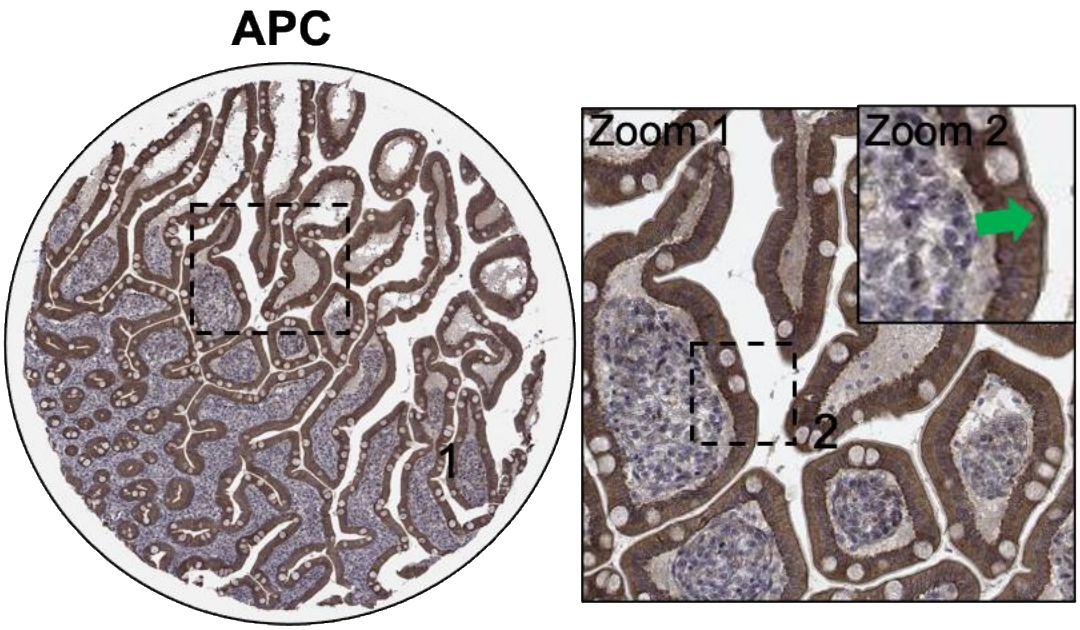

Figure 5-9. HPA staining of APC in human intestinal tissue. Left, large view intestinal cross section. Right, Zooms of cross sections, with zoom 2 focusing on the apical surface.

Conclusion

The studies in this dissertation provide a molecular and temporal framework for the growth of microvilli from the apical surface of epithelial cells. We establish that nascent microvilli are formed both *de novo* as well as templated from existing microvilli, with a fraction of these microvilli also undergoing collapse (Chapter III). With special emphasis on the distal tip targeting proteins, we establish that microvilli actin bundles grow from puncta of EPS8/IRTKS, and that these microvilli are quickly encapsulated and linked to

the plasma membrane. Additionally, taking advantage of the specificity of EPS8 at the distal tips of microvilli and its role during the early stages of microvilli biogenesis, we employed a biotin proximity labeling assay to probe for new molecules involved in microvillus growth and identified KIAA1671 as a novel brush border component implicated in the biogenesis of microvilli (Chapter IV). Future studies highlighted in this section are proposed to elucidate the precise function of EPS8 in microvilli biogenesis and maintenance, and to build a comprehensive understanding of the molecular sequence of events that lead to assembly of microvilli, from the lipid to the protein level.

REFERENCES

Adl, S.M., A.G. Simpson, C.E. Lane, J. Lukes, D. Bass, S.S. Bowser, M.W. Brown, F. Burki, M. Dunthorn, V. Hampl, A. Heiss, M. Hoppenrath, E. Lara, L. Le Gall, D.H. Lynn, H. McManus, E.A. Mitchell, S.E. Mozley-Stanridge, L.W. Parfrey, J. Pawlowski, S. Rueckert, L. Shadwick, C.L. Schoch, A. Smirnov, and F.W. Spiegel. 2012. The revised classification of eukaryotes. *J Eukaryot Microbiol*. 59:429-493.

Akin, O., and R.D. Mullins. 2008. Capping protein increases the rate of actin-based motility by promoting filament nucleation by the Arp2/3 complex. *Cell*. 133:841-851.

Algrain, M., O. Turunen, A. Vaheri, D. Louvard, and M. Arpin. 1993. Ezrin contains cytoskeleton and membrane binding domains accounting for its proposed role as a membrane-cytoskeletal linker. *J Cell Biol*. 120:129-139.

Allen, R.D., J. Metuzals, I. Tasaki, S.T. Brady, and S.P. Gilbert. 1982. Fast axonal transport in squid giant axon. *Science*. 218:1127-1129.

Ameen, N., and G. Apodaca. 2007. Defective CFTR apical endocytosis and enterocyte brush border in myosin VI-deficient mice. *Traffic*. 8:998-1006.

Applewhite, D.A., M. Barzik, S. Kojima, T.M. Svitkina, F.B. Gertler, and G.G. Borisy. 2007. Ena/VASP proteins have an anti-capping independent function in filopodia formation. *Mol Biol Cell*. 18:2579-2591.

Arjonen, A., R. Kaukonen, and J. Ivaska. 2011. Filopodia and adhesion in cancer cell motility. *Cell Adh Migr*. 5:421-430.

Avenarius, M.R., J.F. Krey, R.A. Dumont, C.P. Morgan, C.B. Benson, S. Vijayakumar, C.L. Cunningham, D.I. Scheffer, D.P. Corey, U. Muller, S.M. Jones, and P.G. Barr-Gillespie. 2017. Heterodimeric capping protein is required for stereocilia length and width regulation. *J Cell Biol*. 216:3861-3881.

Baas, A.F., J. Kuipers, N.N. van der Wel, E. Batlle, H.K. Koerten, P.J. Peters, and H.C. Clevers. 2004. Complete Polarization of Single Intestinal Epithelial Cells upon Activation of LKB1 by STRAD. *Cell*. 116:457-466.

Bachmann, C., L. Fischer, U. Walter, and M. Reinhard. 1999. The EVH2 domain of the vasodilator-stimulated phosphoprotein mediates tetramerization, F-actin binding, and actin bundle formation. *J Biol Chem*. 274:23549-23557.

Balla, T. 2013. Phosphoinositides: tiny lipids with giant impact on cell regulation. *Physiol Rev*. 93:1019-1137.

Bartles, J.R., L. Zheng, A. Li, A. Wierda, and B. Chen. 1998. Small espin: a third actin-bundling protein and potential forked protein ortholog in brush border microvilli. *J Cell Biol*. 143:107-119.

Barzik, M., T.I. Kotova, H.N. Higgs, L. Hazelwood, D. Hanein, F.B. Gertler, and D.A. Schafer. 2005. Ena/VASP proteins enhance actin polymerization in the presence of barbed end capping proteins. *J Biol Chem*. 280:28653-28662.

Bear, J.E., T.M. Svitkina, M. Krause, D.A. Schafer, J.J. Loureiro, G.A. Strasser, I.V. Maly, O.Y. Chaga, J.A. Cooper, G.G. Borisy, and F.B. Gertler. 2002. Antagonism between Ena/VASP proteins and actin filament capping regulates fibroblast motility. *Cell*. 109:509-521.

Beer, A.J., J. Gonzalez Delgado, F. Steiniger, B. Qualmann, and M.M. Kessels. 2020. The actin nucleator Cobl organises the terminal web of enterocytes. *Sci Rep*. 10:11156.

Belyantseva, I.A., E.T. Boger, and T.B. Friedman. 2003. Myosin XVa localizes to the tips of inner ear sensory cell stereocilia and is essential for staircase formation of the hair bundle. *Proc Natl Acad Sci U S A*. 100:13958-13963.

Berg, J.S., and R.E. Cheney. 2002. Myosin-X is an unconventional myosin that undergoes intrafilopodial motility. *Nature cell biology*. 4:246-250.

Berryman, M., Z. Franck, and A. Bretscher. 1993. Ezrin is concentrated in the apical microvilli of a wide variety of epithelial cells whereas moesin is found primarily in endothelial cells. *J Cell Sci*. 105:1025-1043.

Bienz, M. 2002. The subcellular destinations of APC proteins. *Nat Rev Mol Cell Biol*. 3:328-338.

Biesova, Z., C. Piccoli, and W.T. Wong. 1997. Isolation and characterization of e3B1, an eps8 binding protein that regulates cell growth. *Oncogene*. 14:233-241.

Bohil, A.B., B.W. Robertson, and R.E. Cheney. 2006. Myosin-X is a molecular motor that functions in filopodia formation. *Proc Natl Acad Sci U S A*. 103:12411-12416.

Brangwynne, C.P., C.R. Eckmann, D.S. Courson, A. Rybarska, C. Hoege, J. Gharakhani, F. Julicher, and A.A. Hyman. 2009. Germline P granules are liquid droplets that localize by controlled dissolution/condensation. *Science*. 324:1729-1732.

Breitsprecher, D., and B.L. Goode. 2013. Formins at a glance. *J Cell Sci*. 126:1-7.

Breitsprecher, D., R. Jaiswal, J.P. Bombardier, C.J. Gould, J. Gelles, and B.L. Goode. 2012. Rocket launcher mechanism of collaborative actin assembly defined by single-molecule imaging. *Science*. 336:1164-1168.

Breitsprecher, D., A.K. Kiesewetter, J. Linkner, C. Urbanke, G.P. Resch, J.V. Small, and J. Faix. 2008. Clustering of VASP actively drives processive, WH2 domain-mediated actin filament elongation. *EMBO J*. 27:2943-2954.

Bretscher, A. 1983. Purification of an 80,000-dalton protein that is a component of the isolated microvillus cytoskeleton, and its localization in nonmuscle cells. *J Cell Biol*. 97:425-432.

Bretscher, A., and K. Weber. 1978. Purification of microvilli and an analysis of the protein components of the microfilament core bundle. *Exp Cell Res*. 116:397-407.

Bretscher, A., and K. Weber. 1979a. Villin: the major microfilament-associated protein of the intestinal microvillus. *Proc Natl Acad Sci U S A*. 76:2321-2325.

Bretscher, A., and K. Weber. 1979b. Villin: the major microfilament-associated protein of the intestinal microvillus. *Proc Natl Acad Sci U S A*. 76:2321-2325.

Bretscher, A., and K. Weber. 1980. Fimbrin, a new microfilament-associated protein present in microvilli and other cell surface structures. *J Cell Biol*. 86:335-340.

Bruce Alberts, A.J., Julian Lewis, Martin Raff, Keith Roberts, and Peter Walter. 2002. MOLECULAR BIOLOGY OF THE CELL, FOURTH EDITION. Norton & Company, Inc.

Bruck, S., T.B. Huber, R.J. Ingham, K. Kim, H. Niederstrasser, P.M. Allen, T. Pawson, J.A. Cooper, and A.S. Shaw. 2006. Identification of a novel inhibitory actin-capping protein binding motif in CD2-associated protein. *J Biol Chem*. 281:19196-19203.

Carlier, M.F., and D. Pantaloni. 1997. Control of actin dynamics in cell motility. *J Mol Biol*. 269:459-467.

Carlton, A.J., J. Halford, A. Underhill, J.Y. Jeng, M.R. Avenarius, M.L. Gilbert, F. Ceriani, K. Ebisine, S.D.M. Brown, M.R. Bowl, P.G. Barr-Gillespie, and W. Marcotti. 2021. Loss of Baiap2l2 destabilizes the transducing stereocilia of cochlear hair cells and leads to deafness. *J Physiol*. 599:1173-1198.

Casaletto, J.B., I. Saotome, M. Curto, and A.I. McClatchey. 2011. Ezrin-mediated apical integrity is required for intestinal homeostasis. *Proc Natl Acad Sci U S A*. 108:11924-11929.

Castagnino, P., Z. Biesova, W.T. Wong, F. Fazioli, G.N. Gill, and P.P. Di Fiore. 1995. Direct binding of eps8 to the juxtamembrane domain of EGFR is phosphotyrosine- and SH2-independent. *Oncogene*. 10:723-729.

Castaneda, N., J. Park, and E.H. Kang. 2021. Regulation of Actin Bundle Mechanics and Structure by Intracellular Environmental Factors. *Front Phys*. 9.

Chang, F., D. Drubin, and P. Nurse. 1997. cdc12p, a protein required for cytokinesis in fission yeast, is a component of the cell division ring and interacts with profilin. *J Cell Biol*. 137:169-182.

Chen, J., R.B. Doctor, and L.J. Mandel. 1994. Cytoskeletal dissociation of ezrin during renal anoxia: role in microvillar injury. *Am J Physiol*. 267:C784-795.

Chereau, D., F. Kerff, P. Graceffa, Z. Grabarek, K. Langsetmo, and R. Dominguez. 2005. Actin-bound structures of Wiskott-Aldrich syndrome protein (WASP)-homology domain 2 and the implications for filament assembly. *Proc Natl Acad Sci U S A*. 102:16644-16649.

Chesarone, M.A., A.G. DuPage, and B.L. Goode. 2010. Unleashing formins to remodel the actin and microtubule cytoskeletons. *Nat Rev Mol Cell Biol*. 11:62-74.

Chinowsky, C.R., J.A. Pinette, L.M. Meenderink, K.S. Lau, and M.J. Tyska. 2020. Nonmuscle myosin-2 contractility-dependent actin turnover limits the length of epithelial microvilli. *Mol Biol Cell*. 31:2803-2815.

Chou, A.M., K.P. Sem, G.D. Wright, T. Sudhaharan, and S. Ahmed. 2014. Dynamin1 is a novel target for IRSp53 protein and works with mammalian enabled (Mena) protein and Eps8 to regulate filopodial dynamics. *J Biol Chem*. 289:24383-24396.

Crawley, S.W., D.A. Shifrin, Jr., N.E. Grega-Larson, R.E. McConnell, A.E. Benesh, S. Mao, Y. Zheng, Q.Y. Zheng, K.T. Nam, B.A. Millis, B. Kachar, and M.J. Tyska. 2014a. Intestinal brush border assembly driven by protocadherin-based intermicrovillar adhesion. *Cell*. 157:433-446.

Crawley, S.W., D.A. Shifrin, Jr., N.E. Grega-Larson, R.E. McConnell, A.E. Benesh, S. Mao, Y. Zheng, Q.Y. Zheng, K.T. Nam, B.A. Millis, B. Kachar, and M.J. Tyska. 2014b. Intestinal brush border assembly driven by protocadherin-based intermicrovillar adhesion. *Cell*. 157:433-446.

Croce, A., G. Cassata, A. Disanza, M.C. Gagliani, C. Tacchetti, M.G. Malabarba, M.F. Carlier, G. Scita, R. Baumeister, and P.P. Di Fiore. 2004. A novel actin barbed-end-capping activity in EPS-8 regulates apical morphogenesis in intestinal cells of Caenorhabditis elegans. *Nat Cell Biol*. 6:1173-1179.

Dent, E.W., and F.B. Gertler. 2003. Cytoskeletal dynamics and transport in growth cone motility and axon guidance. *Neuron*. 40:209-227.

Disanza, A., M.F. Carlier, T.E. Stradal, D. Didry, E. Frittoli, S. Confalonieri, A. Croce, J. Wehland, P.P. Di Fiore, and G. Scita. 2004. Eps8 controls actin-based motility by capping the barbed ends of actin filaments. *Nat Cell Biol*. 6:1180-1188.

Disanza, A., S. Mantoani, M. Hertzog, S. Gerboth, E. Frittoli, A. Steffen, K. Berhoerster, H.J. Kreienkamp, F. Milanesi, P.P. Di Fiore, A. Ciliberto, T.E. Stradal, and G. Scita. 2006. Regulation of cell shape by Cdc42 is mediated by the synergic actin-bundling activity of the Eps8-IRSp53 complex. *Nat Cell Biol*. 8:1337-1347.

Dominguez, R. 2016. The WH2 Domain and Actin Nucleation: Necessary but Insufficient. *Trends Biochem Sci*. 41:478-490.

Dominguez, R., and K.C. Holmes. 2011. Actin structure and function. *Annu Rev Biophys*. 40:169-186.

Edwards, M., A. Zwolak, D.A. Schafer, D. Sept, R. Dominguez, and J.A. Cooper. 2014. Capping protein regulators fine-tune actin assembly dynamics. *Nat Rev Mol Cell Biol*. 15:677-689.

Erdos, G., and Z. Dosztanyi. 2020. Analyzing Protein Disorder with IUPred2A. *Curr Protoc Bioinformatics*. 70:e99.

Faix, J., and K. Rottner. 2022. Ena/VASP proteins in cell edge protrusion, migration and adhesion. *J Cell Sci*. 135.

Falkenburger, B.H., J.B. Jensen, E.J. Dickson, B.C. Suh, and B. Hille. 2010. Phosphoinositides: lipid regulators of membrane proteins. *J Physiol*. 588:3179-3185.

Fazioli, F., L. Minichiello, V. Matoska, P. Castagnino, T. Miki, W.T. Wong, and P.P. Di Fiore. 1993. Eps8, a substrate for the epidermal growth factor receptor kinase, enhances EGF-dependent mitogenic signals. *EMBO J*. 12:3799-3808.

Ferron, F., G. Rebowski, S.H. Lee, and R. Dominguez. 2007. Structural basis for the recruitment of profilin-actin complexes during filament elongation by Ena/VASP. *EMBO J*. 26:4597-4606.

Fievet, B.T., A. Gautreau, C. Roy, L. Del Maestro, P. Mangeat, D. Louvard, and M. Arpin. 2004. Phosphoinositide binding and phosphorylation act sequentially in the activation mechanism of ezrin. *J Cell Biol*. 164:653-659.

Firat-Karalar, E.N., and M.D. Welch. 2011. New mechanisms and functions of actin nucleation. *Curr Opin Cell Biol*. 23:4-13.

Francis, S.P., J.F. Krey, E.S. Krystofiak, R. Cui, S. Nanda, W. Xu, B. Kachar, P.G. Barr-Gillespie, and J.B. Shin. 2015. A short splice form of Xin-actin binding repeat containing 2 (XIRP2) lacking the Xin repeats is required for maintenance of stereocilia morphology and hearing function. *J Neurosci*. 35:1999-2014.

Fritz-Laylin, L.K., M. Riel-Mehan, B.C. Chen, S.J. Lord, T.D. Goddard, T.E. Ferrin, S.M. Nicholson-Dykstra, H. Higgs, G.T. Johnson, E. Betzig, and R.D. Mullins. 2017.

Actin-based protrusions of migrating neutrophils are intrinsically lamellar and facilitate direction changes. *Elife*. 6.

Frost, A., V.M. Unger, and P. De Camilli. 2009. The BAR domain superfamily: membrane-molding macromolecules. *Cell*. 137:191-196.

Furness, D.N., S.L. Johnson, U. Manor, L. Ruttiger, A. Tocchetti, N. Offenhauser, J. Olt, R.J. Goodyear, S. Vijayakumar, Y. Dai, C.M. Hackney, C. Franz, P.P. Di Fiore, S. Masetto, S.M. Jones, M. Knipper, M.C. Holley, G.P. Richardson, B. Kachar, and W. Marcotti. 2013. Progressive hearing loss and gradual deterioration of sensory hair bundles in the ears of mice lacking the actin-binding protein Eps8L2. *Proc Natl Acad Sci U S A*. 110:13898-13903.

Gaeta, I.M., L.M. Meenderink, M.M. Postema, C.S. Cencer, and M.J. Tyska. 2021a. Direct visualization of epithelial microvilli biogenesis. *Curr Biol*. 31:2561-2575 e2566.

Gaeta, I.M., L.M. Meenderink, and M.J. Tyska. 2021b. A protocol for imaging microvilli biogenesis on the surface of cultured porcine kidney epithelial cell monolayers. *STAR Protoc*. 2:100998.

Gassama-Diagne, A., W. Yu, M. ter Beest, F. Martin-Belmonte, A. Kierbel, J. Engel, and K. Mostov. 2006. Phosphatidylinositol-3,4,5-trisphosphate regulates the formation of the basolateral plasma membrane in epithelial cells. *Nat Cell Biol*. 8:963-970.

Goldschmidt-Clermont, P.J., M.I. Furman, D. Wachsstock, D. Safer, V.T. Nachmias, and T.D. Pollard. 1992. The control of actin nucleotide exchange by thymosin beta 4 and profilin. A potential regulatory mechanism for actin polymerization in cells. *Mol Biol Cell*. 3:1015-1024.

Goode, B.L., and M.J. Eck. 2007. Mechanism and function of formins in the control of actin assembly. *Annu Rev Biochem*. 76:593-627.

Gorelik, J., A.I. Shevchuk, G.I. Frolenkov, I.A. Diakonov, M.J. Lab, C.J. Kros, G.P. Richardson, I. Vodyanoy, C.R. Edwards, D. Klenerman, and Y.E. Korchev. 2003. Dynamic assembly of surface structures in living cells. *Proc Natl Acad Sci U S A*. 100:5819-5822.

Granger, B., and R.F. Baker. 1950. Electron microscope investigation of the striated border of intestinal epithelium. *Anat Rec*. 107:423-441.

Grati, M., and B. Kachar. 2011. Myosin VIIa and sans localization at stereocilia upper tip-link density implicates these Usher syndrome proteins in mechanotransduction. *Proc Natl Acad Sci U S A*. 108:11476-11481.

Grega-Larson, N.E., S.W. Crawley, A.L. Erwin, and M.J. Tyska. 2015. Cordon bleu promotes the assembly of brush border microvilli. *Mol Biol Cell*. 26:3803-3815.

Grieve, A.G., S.E. Moss, and M.J. Hayes. 2012. Annexin A2 at the interface of actin and membrane dynamics: a focus on its roles in endocytosis and cell polarization. *Int J Cell Biol*. 2012:852430.

Halet, G. 2005. Imaging phosphoinositide dynamics using GFP-tagged protein domains. *Biol Cell*. 97:501-518.

Hao, J.J., Y. Liu, M. Kruhlak, K.E. Debell, B.L. Rellahan, and S. Shaw. 2009. Phospholipase C-mediated hydrolysis of PIP2 releases ERM proteins from lymphocyte membrane. *J Cell Biol*. 184:451-462.

Hayden, S.M., J.S. Wolenski, and M.S. Mooseker. 1990. Binding of brush border myosin I to phospholipid vesicles. *J Cell Biol*. 111:443-451.

Hegan, P.S., H. Giral, M. Levi, and M.S. Mooseker. 2012. Myosin VI is required for maintenance of brush border structure, composition, and membrane trafficking functions in the intestinal epithelial cell. *Cytoskeleton (Hoboken)*. 69:235-251.

Heintzelman, M.B., and M.S. Mooseker. 1990. Assembly of the brush border cytoskeleton: changes in the distribution of microvillar core proteins during enterocyte differentiation in adult chicken intestine. *Cell motility and the cytoskeleton*. 15:12-22.

Helander, H.F., and L. Fandriks. 2014. Surface area of the digestive tract - revisited. *Scand J Gastroenterol*. 49:681-689.

Hernandez-Valladares, M., T. Kim, B. Kannan, A. Tung, A.H. Aguda, M. Larsson, J.A. Cooper, and R.C. Robinson. 2010. Structural characterization of a capping

protein interaction motif defines a family of actin filament regulators. *Nat Struct Mol Biol*. 17:497-503.

Hertzog, M., F. Milanesi, L. Hazelwood, A. Disanza, H. Liu, E. Perlade, M.G. Malabarba, S. Pasqualato, A. Maiolica, S. Confalonieri, C. Le Clainche, N. Offenhauser, J. Block, K. Rottner, P.P. Di Fiore, M.F. Carlier, N. Volkmann, D. Hanein, and G. Scita. 2010. Molecular basis for the dual function of Eps8 on actin dynamics: bundling and capping. *PLoS Biol*. 8:e1000387.

Hirokawa, N., and J.E. Heuser. 1981. Quick-freeze, deep-etch visualization of the cytoskeleton beneath surface differentiations of intestinal epithelial cells. *J Cell Biol*. 91:399-409.

Hirokawa, N., L.G. Tilney, K. Fujiwara, and J.E. Heuser. 1982. Organization of actin, myosin, and intermediate filaments in the brush border of intestinal epithelial cells. *J Cell Biol*. 94:425-443.

Howe, C.L., and M.S. Mooseker. 1983. Characterization of the 110-kdalton actin-calmodulin-, and membrane-binding protein from microvilli of intestinal epithelial cells. *J Cell Biol*. 97:974-985.

Hudspeth, A.J. 1985. The cellular basis of hearing: the biophysics of hair cells. *Science*. 230:745-752.

Hug, C., P.Y. Jay, I. Reddy, J.G. McNally, P.C. Bridgman, E.L. Elson, and J.A. Cooper. 1995. Capping protein levels influence actin assembly and cell motility in dictyostelium. *Cell*. 81:591-600.

Huttlin, E.L., R.J. Bruckner, J. Navarrete-Perea, J.R. Cannon, K. Baltier, F. Gebreab, M.P. Gygi, A. Thornock, G. Zarraga, S. Tam, J. Szpyt, B.M. Gassaway, A. Panov, H. Parzen, S. Fu, A. Golbazi, E. Maenpaa, K. Stricker, S. Guha Thakurta, T. Zhang, R. Rad, J. Pan, D.P. Nusinow, J.A. Paulo, D.K. Schweppe, L.P. Vaites, J.W. Harper, and S.P. Gygi. 2021. Dual proteome-scale networks reveal cell-specific remodeling of the human interactome. *Cell*. 184:3022-3040 e3028.

Huttlin, E.L., R.J. Bruckner, J.A. Paulo, J.R. Cannon, L. Ting, K. Baltier, G. Colby, F. Gebreab, M.P. Gygi, H. Parzen, J. Szpyt, S. Tam, G. Zarraga, L. Pontano-Vaites, S. Swarup, A.E. White, D.K. Schweppe, R. Rad, B.K. Erickson, R.A. Obar, K.G. Guruharsha, K. Li, S. Artavanis-Tsakonas, S.P. Gygi, and J.W. Harper. 2017. Architecture of the human interactome defines protein communities and disease networks. *Nature*. 545:505-509.

Jacquemet, G., A. Stubb, R. Saup, M. Miihkinen, E. Kremneva, H. Hamidi, and J. Ivaska. 2019. Filopodome Mapping Identifies p130Cas as a Mechanosensitive Regulator of Filopodia Stability. *Curr Biol*. 29:202-216 e207.

Kabsch, W., H.G. Mannherz, D. Suck, E.F. Pai, and K.C. Holmes. 1990. Atomic structure of the actin:DNase I complex. *Nature*. 347:37-44.

Kachar, B., M. Parakkal, M. Kurc, Y. Zhao, and P.G. Gillespie. 2000. High-resolution structure of hair-cell tip links. *Proc Natl Acad Sci U S A*. 97:13336-13341.

Karpov, S.A., and B.S.C. Leadbeater. 1998. Cytoskeleton Structure and Composition in Choanoflagellates. *Journal of Eukaryotic Microbiology*. 45:361-367.

Kazmierczak, P., H. Sakaguchi, J. Tokita, E.M. Wilson-Kubalek, R.A. Milligan, U. Muller, and B. Kachar. 2007. Cadherin 23 and protocadherin 15 interact to form tip-link filaments in sensory hair cells. *Nature*. 449:87-91.

Kelleher, J.F., S.J. Atkinson, and T.D. Pollard. 1995. Sequences, structural models, and cellular localization of the actin-related proteins Arp2 and Arp3 from Acanthamoeba. *J Cell Biol*. 131:385-397.

Kim, D.I., K.C. Birendra, W. Zhu, K. Motamedchaboki, V. Doye, and K.J. Roux. 2014. Probing nuclear pore complex architecture with proximity-dependent biotinylation. *Proc Natl Acad Sci U S A*. 111:E2453-2461.

Kim, D.I., S.C. Jensen, K.A. Noble, B. Kc, K.H. Roux, K. Motamedchaboki, and K.J. Roux. 2016. An improved smaller biotin ligase for BioID proximity labeling. *Mol Biol Cell*. 27:1188-1196.

Kishan, K.V., G. Scita, W.T. Wong, P.P. Di Fiore, and M.E. Newcomer. 1997. The SH3 domain of Eps8 exists as a novel intertwined dimer. *Nat Struct Biol*. 4:739-743.

Korn, E.D., M.F. Carlier, and D. Pantaloni. 1987. Actin polymerization and ATP hydrolysis. *Science*. 238:638-644.

Kovar, D.R., E.S. Harris, R. Mahaffy, H.N. Higgs, and T.D. Pollard. 2006. Control of the assembly of ATP- and ADP-actin by formins and profilin. *Cell*. 124:423-435.

Kuo, W.T., M.A. Odenwald, J.R. Turner, and L. Zuo. 2022. Tight junction proteins occludin and ZO-1 as regulators of epithelial proliferation and survival. *Ann N Y Acad Sci*. 1514:21-33.

Kuo, W.T., L. Zuo, M.A. Odenwald, S. Madha, G. Singh, C.B. Gurniak, C. Abraham, and J.R. Turner. 2021. The Tight Junction Protein ZO-1 Is Dispensable for Barrier Function but Critical for Effective Mucosal Repair. *Gastroenterology*. 161:1924-1939.

Kurochkina, N., and U. Guha. 2013. SH3 domains: modules of protein-protein interactions. *Biophys Rev*. 5:29-39.

Lambrechts, A., A.V. Kwiatkowski, L.M. Lanier, J.E. Bear, J. Vandekerckhove, C. Ampe, and F.B. Gertler. 2000. cAMP-dependent protein kinase phosphorylation of EVL, a Mena/VASP relative, regulates its interaction with actin and SH3 domains. *J Biol Chem*. 275:36143-36151.

Larson, A.G., D. Elnatan, M.M. Keenen, M.J. Trnka, J.B. Johnston, A.L. Burlingame, D.A. Agard, S. Redding, and G.J. Narlikar. 2017. Liquid droplet formation by HP1alpha suggests a role for phase separation in heterochromatin. *Nature*. 547:236-240.

Lee, S.H., F. Kerff, D. Chereau, F. Ferron, A. Klug, and R. Dominguez. 2007. Structural basis for the actin-binding function of missing-in-metastasis. *Structure*. 15:145-155.

Li, Q., M.R. Nance, R. Kulikauskas, K. Nyberg, R. Fehon, P.A. Karplus, A. Bretscher, and J.J. Tesmer. 2007. Self-masking in an intact ERM-merlin protein: an active role for the central alpha-helical domain. *J Mol Biol*. 365:1446-1459.

Li, X.H., P.L. Chavali, R. Pancsa, S. Chavali, and M.M. Babu. 2018. Function and Regulation of Phase-Separated Biological Condensates. *Biochemistry*. 57:2452-2461.

Lin, L., Y. Shi, M. Wang, C. Wang, Q. Lu, J. Zhu, and R. Zhang. 2021. Phase separation-mediated condensation of Whirlin-Myo15-Eps8 stereocilia tip complex. *Cell Rep*. 34:108770.

Maa, M.C., C.Y. Hsieh, and T.H. Leu. 2001. Overexpression of p97Eps8 leads to cellular transformation: implication of pleckstrin homology domain in p97Eps8-mediated ERK activation. *Oncogene*. 20:106-112.

Machesky, L.M., S.J. Atkinson, C. Ampe, J. Vandekerckhove, and T.D. Pollard. 1994. Purification of a cortical complex containing two unconventional actins from Acanthamoeba by affinity chromatography on profilin-agarose. *J Cell Biol*. 127:107-115.

Manor, U., A. Disanza, M. Grati, L. Andrade, H. Lin, P.P. Di Fiore, G. Scita, and B. Kachar. 2011a. Regulation of stereocilia length by myosin XVa and whirlin depends on the actin-regulatory protein Eps8. *Curr Biol*. 21:167-172.

Manor, U., A. Disanza, M.H. Grati, L. Andrade, H. Lin, P.P. Di Fiore, G. Scita, and B. Kachar. 2011b. Regulation of Stereocilia Length by Myosin XVa and Whirlin Depends on the Actin-Regulatory Protein Eps8. *Current Biology*. 21:167-172.

Martin, E.W., and A.S. Holehouse. 2020. Intrinsically disordered protein regions and phase separation: sequence determinants of assembly or lack thereof. *Emerg Top Life Sci*. 4:307-329.

Martin-Belmonte, F., A. Gassama, A. Datta, W. Yu, U. Rescher, V. Gerke, and K. Mostov. 2007. PTEN-mediated apical segregation of phosphoinositides controls epithelial morphogenesis through Cdc42. *Cell*. 128:383-397.

Matoskova, B., W.T. Wong, N. Nomura, K.C. Robbins, and P.P. Di Fiore. 1996. RN-tre specifically binds to the SH3 domain of eps8 with high affinity and confers growth advantage to NIH3T3 upon carboxy-terminal truncation. *Oncogene*. 12:2679-2688.

Mattila, P.K., A. Pykalainen, J. Saarikangas, V.O. Paavilainen, H. Vihinen, E. Jokitalo, and P. Lappalainen. 2007. Missing-in-metastasis and IRSp53 deform PI(4,5)P2-rich membranes by an inverse BAR domain-like mechanism. *J Cell Biol*. 176:953-964.

Mazerik, J.N., and M.J. Tyska. 2012. Myosin-1A targets to microvilli using multiple membrane binding motifs in the tail homology 1 (TH1) domain. *J Biol Chem*. 287:13104-13115.

McConnell, P., M. Mekel, A.G. Kozlov, O.L. Mooren, T.M. Lohman, and J.A. Cooper. 2020. Comparative Analysis of CPI-Motif Regulation of Biochemical Functions of Actin Capping Protein. *Biochemistry*. 59:1202-1215.

McConnell, R.E., A.E. Benesh, S. Mao, D.L. Tabb, and M.J. Tyska. 2011a. Proteomic analysis of the enterocyte brush border. *American Journal of Physiology-Gastrointestinal and Liver Physiology*. 300:G914-G926.

McConnell, R.E., A.E. Benesh, S. Mao, D.L. Tabb, and M.J. Tyska. 2011b. Proteomic analysis of the enterocyte brush border. *Am J Physiol Gastrointest Liver Physiol*. 300:G914-926.

McGrath, J., P. Roy, and B.J. Perrin. 2017. Stereocilia morphogenesis and maintenance through regulation of actin stability. *Semin Cell Dev Biol*. 65:88-95.

Meenderink, L.M., I.M. Gaeta, M.M. Postema, C.S. Cencer, C.R. Chinowsky, E.S. Krystofiak, B.A. Millis, and M.J. Tyska. 2019. Actin Dynamics Drive Microvillar Motility and Clustering during Brush Border Assembly. *Dev Cell*. 50:545-556 e544.

Mejillano, M.R., S. Kojima, D.A. Applewhite, F.B. Gertler, T.M. Svitkina, and G.G. Borisy. 2004. Lamellipodial versus filopodial mode of the actin nanomachinery: pivotal role of the filament barbed end. *Cell*. 118:363-373.

Meszaros, B., G. Erdos, and Z. Dosztanyi. 2018. IUPred2A: context-dependent prediction of protein disorder as a function of redox state and protein binding. *Nucleic Acids Res*. 46:W329-W337.

Millard, T.H., G. Bompard, M.Y. Heung, T.R. Dafforn, D.J. Scott, L.M. Machesky, and K. Futterer. 2005. Structural basis of filopodia formation induced by the IRSp53/MIM homology domain of human IRSp53. *EMBO J*. 24:240-250.

Millard, T.H., J. Dawson, and L.M. Machesky. 2007. Characterisation of IRTKS, a novel IRSp53/MIM family actin regulator with distinct filament bundling properties. *Journal of Cell Science*. 120:1663-1672.

Mogilner, A., and B. Rubinstein. 2005. The physics of filopodial protrusion. *Biophys J*. 89:782-795.

Mongiovi, A.M., P.R. Romano, S. Panni, M. Mendoza, W.T. Wong, A. Musacchio, G. Cesareni, and P.P. Di Fiore. 1999. A novel peptide-SH3 interaction. *EMBO J*. 18:5300-5309.

Mooseker, M.S., T.D. Pollard, and K.A. Wharton. 1982. Nucleated polymerization of actin from the membrane-associated ends of microvillar filaments in the intestinal brush border. *J Cell Biol*. 95:223-233.

Mooseker, M.S., and L.G. Tilney. 1975a. Organization of an actin filament-membrane complex. Filament polarity and membrane attachment in the microvilli of intestinal epithelial cells. *J Cell Biol*. 67:725-743.

Mooseker, M.S., and L.G. Tilney. 1975b. Organization of an actin filament-membrane complex. Filament polarity and membrane attachment in the microvilli of intestinal epithelial cells. *The Journal of Cell Biology*. 67:725-743.

Morales, E.A., C. Arnaiz, E.S. Krystofiak, M. Zanic, and M.J. Tyska. 2022. Mitotic Spindle Positioning (MISP) is an actin bundler that selectively stabilizes the rootlets of epithelial microvilli. *Cell Rep*. 39:110692.

Mullins, R.D., J.A. Heuser, and T.D. Pollard. 1998. The interaction of Arp2/3 complex with actin: nucleation, high affinity pointed end capping, and formation of branching networks of filaments. *Proc Natl Acad Sci U S A*. 95:6181-6186.

Nagase, H., and Y. Nakamura. 1993. Mutations of the APC (adenomatous polyposis coli) gene. *Hum Mutat*. 2:425-434.

Nishimura, Y., S. Shi, F. Zhang, R. Liu, Y. Takagi, A.D. Bershadsky, V. Viasnoff, and J.R. Sellers. 2021. The formin inhibitor SMIFH2 inhibits members of the myosin superfamily. *J Cell Sci*. 134.

Odenwald, M.A., W. Choi, W.T. Kuo, G. Singh, A. Sailer, Y. Wang, L. Shen, A.S. Fanning, and J.R. Turner. 2018. The scaffolding protein ZO-1 coordinates actomyosin and epithelial apical specializations in vitro and in vivo. *J Biol Chem*. 293:17317-17335.

Offenhauser, N., A. Borgonovo, A. Disanza, P. Romano, I. Ponzanelli, G. Iannolo, P.P. Di Fiore, and G. Scita. 2004. The eps8 family of proteins links growth factor stimulation to actin reorganization generating functional redundancy in the Ras/Rac pathway. *Mol Biol Cell*. 15:91-98.

Ohishi, T., H. Yoshida, M. Katori, T. Migita, Y. Muramatsu, M. Miyake, Y. Ishikawa, A. Saiura, S.I. Iemura, T. Natsume, and H. Seimiya. 2017. Tankyrase-Binding Protein TNKS1BP1 Regulates Actin Cytoskeleton Rearrangement and Cancer Cell Invasion. *Cancer Res*. 77:2328-2338.

Ohta, K., R. Higashi, A. Sawaguchi, and K. Nakamura. 2012. Helical arrangement of filaments in microvillar actin bundles. *J Struct Biol*. 177:513-519.

Okada, K., F. Bartolini, A.M. Deaconescu, J.B. Moseley, Z. Dogic, N. Grigorieff, G.G. Gundersen, and B.L. Goode. 2010. Adenomatous polyposis coli protein nucleates actin assembly and synergizes with the formin mDia1. *J Cell Biol*. 189:1087-1096.

Paul, A.S., and T.D. Pollard. 2008. The role of the FH1 domain and profilin in formin-mediated actin-filament elongation and nucleation. *Curr Biol*. 18:9-19.

Pearson, M.A., D. Reczek, A. Bretscher, and P.A. Karplus. 2000. Structure of the ERM protein moesin reveals the FERM domain fold masked by an extended actin binding tail domain. *Cell*. 101:259-270.

Pelaseyed, T., and A. Bretscher. 2018. Regulation of actin-based apical structures on epithelial cells. *J Cell Sci*. 131.

Peña, J.F., A. Alié, D.J. Richter, L. Wang, N. Funayama, and S.A. Nichols. 2016. Conserved expression of vertebrate microvillar gene homologs in choanocytes of freshwater sponges. *EvoDevo*. 7:13.

Perrin, B.J., and J.M. Ervasti. 2010. The actin gene family: function follows isoform. *Cytoskeleton (Hoboken)*. 67:630-634.

Perrin, B.J., K.J. Sonnemann, and J.M. Ervasti. 2010. beta-actin and gamma-actin are each dispensable for auditory hair cell development but required for Stereocilia maintenance. *PLoS Genet*. 6:e1001158.

Peskin, C.S., G.M. Odell, and G.F. Oster. 1993. Cellular motions and thermal fluctuations: the Brownian ratchet. *Biophys J*. 65:316-324.

Pinette, J.A., S. Mao, B.A. Millis, E.S. Krystofiak, J.J. Faust, and M.J. Tyska. 2019. Brush border protocadherin CDHR2 promotes the elongation and maximized packing of microvilli in vivo. *Mol Biol Cell*. 30:108-118.

Pollard, T.D. 1984. Polymerization of ADP-actin. *J Cell Biol*. 99:769-777.

Pollard, T.D. 1986. Rate constants for the reactions of ATP- and ADP-actin with the ends of actin filaments. *J Cell Biol*. 103:2747-2754.

Pollard, T.D., L. Blanchoin, and R.D. Mullins. 2000. Molecular mechanisms controlling actin filament dynamics in nonmuscle cells. *Annu Rev Biophys Biomol Struct*. 29:545-576.

Postema, M.M., N.E. Grega-Larson, L.M. Meenderink, and M.J. Tyska. 2019. PACSIN2-dependent apical endocytosis regulates the morphology of epithelial microvilli. *Mol Biol Cell*. 30:2515-2526.

Postema, M.M., N.E. Grega-Larson, A.C. Neininger, and M.J. Tyska. 2018a. IRTKS (BAIAP2L1) Elongates Epithelial Microvilli Using EPS8-Dependent and Independent Mechanisms. *Curr Biol*.

Postema, M.M., N.E. Grega-Larson, A.C. Neininger, and M.J. Tyska. 2018b. IRTKS (BAIAP2L1) Elongates Epithelial Microvilli Using EPS8-Dependent and Independent Mechanisms. *Curr Biol*. 28:2876-2888 e2874.

Revenu, C., F. Ubelmann, I. Hurbain, F. El-Marjou, F. Dingli, D. Loew, D. Delacour, J. Gilet, E. Brot-Laroche, F. Rivero, D. Louvard, and S. Robine. 2012. A new role for the architecture of microvillar actin bundles in apical retention of membrane proteins. *Molecular biology of the cell*. 23:324-336.

Roman-Fernandez, A., J. Roignot, E. Sandilands, M. Nacke, M.A. Mansour, L. McGarry, E. Shanks, K.E. Mostov, and D.M. Bryant. 2018. The phospholipid PI(3,4)P2 is an apical identity determinant. *Nat Commun*. 9:5041.

Romero, S., C. Le Clainche, D. Didry, C. Egile, D. Pantaloni, and M.F. Carlier. 2004. Formin is a processive motor that requires profilin to accelerate actin assembly and associated ATP hydrolysis. *Cell*. 119:419-429.

Roux, K.J., D.I. Kim, B. Burke, and D.G. May. 2018. BioID: A Screen for Protein-Protein Interactions. *Curr Protoc Protein Sci*. 91:19 23 11-19 23 15.

Roux, K.J., D.I. Kim, M. Raida, and B. Burke. 2012. A promiscuous biotin ligase fusion protein identifies proximal and interacting proteins in mammalian cells. *J Cell Biol*. 196:801-810.

Roy, P., and B.J. Perrin. 2018. The stable actin core of mechanosensory stereocilia features continuous turnover of actin cross-linkers. *Mol Biol Cell*. 29:1856-1865.

Rzadzinska, A.K., M.E. Schneider, C. Davies, G.P. Riordan, and B. Kachar. 2004. An actin molecular treadmill and myosins maintain stereocilia functional architecture and self-renewal. *J Cell Biol*. 164:887-897.

Saarikangas, J., H. Zhao, A. Pykalainen, P. Laurinmaki, P.K. Mattila, P.K. Kinnunen, S.J. Butcher, and P. Lappalainen. 2009. Molecular mechanisms of membrane deformation by I-BAR domain proteins. *Curr Biol*. 19:95-107.

Salles, F.T., R.C. Merritt, Jr., U. Manor, G.W. Dougherty, A.D. Sousa, J.E. Moore, C.M. Yengo, A.C. Dose, and B. Kachar. 2009. Myosin IIIa boosts elongation of stereocilia by transporting espin 1 to the plus ends of actin filaments. *Nat Cell Biol*. 11:443-450.

Sanchez, A.D., T.C. Branon, L.E. Cote, A. Papagiannakis, X. Liang, M.A. Pickett, K. Shen, C. Jacobs-Wagner, A.Y. Ting, and J.L. Feldman. 2021. Proximity labeling reveals non-centrosomal microtubule-organizing center components required for microtubule growth and localization. *Curr Biol*. 31:3586-3600 e3511.

Saotome, I., M. Curto, and A.I. McClatchey. 2004. Ezrin is essential for epithelial organization and villus morphogenesis in the developing intestine. *Dev Cell*. 6:855-864.

Schafer, D.A., M.S. Mooseker, and J.A. Cooper. 1992. Localization of capping protein in chicken epithelial cells by immunofluorescence and biochemical fractionation. *J Cell Biol*. 118:335-346.

Schwander, M., B. Kachar, and U. Muller. 2010. Review series: The cell biology of hearing. *J Cell Biol*. 190:9-20.

Scita, G., P. Tenca, L.B. Areces, A. Tocchetti, E. Frittoli, G. Giardina, I. Ponzanelli, P. Sini, M. Innocenti, and P.P. Di Fiore. 2001. An effector region in Eps8 is responsible for the activation of the Rac-specific GEF activity of Sos-1 and for the proper localization of the Rac-based actin–polymerizing machine. *The Journal of Cell Biology*. 154:1031-1044.

Sebe-Pedros, A., P. Burkhardt, N. Sanchez-Pons, S.R. Fairclough, B.F. Lang, N. King, and I. Ruiz-Trillo. 2013. Insights into the origin of metazoan filopodia and microvilli. *Mol Biol Evol*. 30:2013-2023.

Sekerkova, G., C.P. Richter, and J.R. Bartles. 2011. Roles of the espin actin-bundling proteins in the morphogenesis and stabilization of hair cell stereocilia revealed in CBA/CaJ congenic jerker mice. *PLoS Genet*. 7:e1002032.

Sinnar, S.A., S. Antoku, J.M. Saffin, J.A. Cooper, and S. Halpain. 2014. Capping protein is essential for cell migration in vivo and for filopodial morphology and dynamics. *Mol Biol Cell*. 25:2152-2160.

Skowron, J.F., W.M. Bement, and M.S. Mooseker. 1998. Human brush border myosin-I and myosin-Ic expression in human intestine and Caco-2BBe cells. *Cell Motil Cytoskeleton*. 41:308-324.

Skowron, J.F., and M.S. Mooseker. 1999. Cloning and characterization of mouse brush border myosin-I in adult and embryonic intestine. *J Exp Zool*. 283:242-257.

Specian, R.D., and M.R. Neutra. 1981. The surface topography of the colonic crypt in rabbit and monkey. *Am J Anat*. 160:461-472.

Svitkina, T.M., E.A. Bulanova, O.Y. Chaga, D.M. Vignjevic, S. Kojima, J.M. Vasiliev, and G.G. Borisy. 2003. Mechanism of filopodia initiation by reorganization of a dendritic network. *J Cell Biol*. 160:409-421.

Swanson, J.A. 2014. Phosphoinositides and engulfment. *Cell Microbiol*. 16:1473-1483.

Taylor, R., A. Bullen, S.L. Johnson, E.M. Grimm-Gunter, F. Rivero, W. Marcotti, A. Forge, and N. Daudet. 2015. Absence of plastin 1 causes abnormal maintenance of hair cell stereocilia and a moderate form of hearing loss in mice. *Hum Mol Genet*. 24:37-49.

Theillet, F.X., L. Kalmar, P. Tompa, K.H. Han, P. Selenko, A.K. Dunker, G.W. Daughdrill, and V.N. Uversky. 2013. The alphabet of intrinsic disorder: I. Act like a Pro: On the abundance and roles of proline residues in intrinsically disordered proteins. *Intrinsically Disord Proteins*. 1:e24360.

Tilney, L.G., and R.R. Cardell. 1970. Factors controlling the reassembly of the microvillous border of the small intestine of the salamander. *J Cell Biol*. 47:408-422.

Tilney, L.G., D.A. Cotanche, and M.S. Tilney. 1992a. Actin filaments, stereocilia and hair cells of the bird cochlea. VI. How the number and arrangement of stereocilia are determined. *Development*. 116:213-226.

Tilney, L.G., D.J. Derosier, and M.J. Mulroy. 1980. The organization of actin filaments in the stereocilia of cochlear hair cells. *J Cell Biol*. 86:244-259.

Tilney, L.G., M.S. Tilney, and D.J. DeRosier. 1992b. Actin filaments, stereocilia, and hair cells: how cells count and measure. *Annu Rev Cell Biol*. 8:257-274.

Tocchetti, A., C.B. Soppo, F. Zani, F. Bianchi, M.C. Gagliani, B. Pozzi, J. Rozman, R. Elvert, N. Ehrhardt, B. Rathkolb, C. Moerth, M. Horsch, H. Fuchs, V. Gailus-Durner, J. Beckers, M. Klingenspor, E. Wolf, M. Hrabe de Angelis, E. Scanziani, C. Tacchetti, G. Scita, P.P. Di Fiore, and N. Offenhauser. 2010. Loss of the actin remodeler Eps8 causes intestinal defects and improved metabolic status in mice. *PLoS One*. 5:e9468.

Turunen, O., T. Wahlstrom, and A. Vaheri. 1994. Ezrin has a COOH-terminal actin-binding site that is conserved in the ezrin protein family. *J Cell Biol*. 126:1445-1453.

Tyska, M.J., A.T. Mackey, J.D. Huang, N.G. Copeland, N.A. Jenkins, and M.S. Mooseker. 2005. Myosin-1a is critical for normal brush border structure and composition. *Mol Biol Cell*. 16:2443-2457.

Uhlik, M.T., B. Temple, S. Bencharit, A.J. Kimple, D.P. Siderovski, and G.L. Johnson. 2005. Structural and evolutionary division of phosphotyrosine binding (PTB) domains. *J Mol Biol*. 345:1-20.

van Dongen, J.M., W.J. Visser, W.T. Daems, and H. Galjaard. 1976. The relation between cell proliferation, differentiation and ultrastructural development in rat intestinal epithelium. *Cell Tissue Res*. 174:183-199.

Vignjevic, D., S. Kojima, Y. Aratyn, O. Danciu, T. Svitkina, and G.G. Borisy. 2006. Role of fascin in filopodial protrusion. *J Cell Biol*. 174:863-875.

Vignjevic, D., D. Yarar, M.D. Welch, J. Peloquin, T. Svitkina, and G.G. Borisy. 2003. Formation of filopodia-like bundles in vitro from a dendritic network. *J Cell Biol*. 160:951-962.

Viswanatha, R., P.Y. Ohouo, M.B. Smolka, and A. Bretscher. 2012. Local phosphocycling mediated by LOK/SLK restricts ezrin function to the apical aspect of epithelial cells. *J Cell Biol*. 199:969-984.

Wayt, J., and A. Bretscher. 2014. Cordon Bleu serves as a platform at the basal region of microvilli, where it regulates microvillar length through its WH2 domains. *Mol Biol Cell*. 25:2817-2827.

Wear, M.A., A. Yamashita, K. Kim, Y. Maeda, and J.A. Cooper. 2003. How capping protein binds the barbed end of the actin filament. *Curr Biol*. 13:1531-1537.

Weck, M.L., S.W. Crawley, C.R. Stone, and M.J. Tyska. 2016. Myosin-7b Promotes Distal Tip Localization of the Intermicrovillar Adhesion Complex. *Curr Biol*. 26:2717-2728.

Wegner, A. 1982. Treadmilling of actin at physiological salt concentrations. An analysis of the critical concentrations of actin filaments. *J Mol Biol*. 161:607-615.

Welling, L.W., and D.J. Welling. 1975. Surface areas of brush border and lateral cell walls in the rabbit proximal nephron. *Kidney Int*. 8:343-348.

Wells, A.L., A.W. Lin, L.Q. Chen, D. Safer, S.M. Cain, T. Hasson, B.O. Carragher, R.A. Milligan, and H.L. Sweeney. 1999. Myosin VI is an actin-based motor that moves backwards. *Nature*. 401:505-508.

Woodruff, J.B., B. Ferreira Gomes, P.O. Widlund, J. Mahamid, A. Honigmann, and A.A. Hyman. 2017. The Centrosome Is a Selective Condensate that Nucleates Microtubules by Concentrating Tubulin. *Cell*. 169:1066-1077 e1010.

Yamagishi, A., M. Masuda, T. Ohki, H. Onishi, and N. Mochizuki. 2004. A novel actin bundling/filopodium-forming domain conserved in insulin receptor tyrosine kinase substrate p53 and missing in metastasis protein. *J Biol Chem*. 279:14929-14936.

Yamashita, A., K. Maeda, and Y. Maeda. 2003. Crystal structure of CapZ: structural basis for actin filament barbed end capping. *EMBO J*. 22:1529-1538.

Yang, C., L. Czech, S. Gerboth, S. Kojima, G. Scita, and T. Svitkina. 2007. Novel roles of formin mDia2 in lamellipodia and filopodia formation in motile cells. *PLoS Biol*. 5:e317.

Yang, C., and T. Svitkina. 2011. Filopodia initiation: focus on the Arp2/3 complex and formins. *Cell Adh Migr*. 5:402-408.

Yang, D.C., K.M. Blair, and N.R. Salama. 2016. Staying in Shape: the Impact of Cell Shape on Bacterial Survival in Diverse Environments. *Microbiol Mol Biol Rev*. 80:187-203.

Yoshida, S., T. Fukutomi, T. Kimura, H. Sakurai, R. Hatano, H. Yamamoto, K. Mukaisho, T. Hattori, H. Sugihara, and S. Asano. 2016. Comprehensive proteome analysis of brush border membrane fraction of ileum of ezrin knockdown mice. *Biomed Res*. 37:127-139.

Zampini, V., L. Ruttiger, S.L. Johnson, C. Franz, D.N. Furness, J. Waldhaus, H. Xiong, C.M. Hackney, M.C. Holley, N. Offenhauser, P.P. Di Fiore, M. Knipper, S. Masetto, and W. Marcotti. 2011. Eps8 regulates hair bundle length and functional maturation of mammalian auditory hair cells. *PLoS Biol*. 9:e1001048.

Zhao, H., A. Pykalainen, and P. Lappalainen. 2011. I-BAR domain proteins: linking actin and plasma membrane dynamics. *Curr Opin Cell Biol*. 23:14-21.

Zhu, H., M. Li, R. Zhao, M. Li, Y. Chai, Z. Zhu, Y. Yang, W. Li, Z. Xie, X. Li, K. Lei, X. Li, and G. Ou. 2022. In situ structure of intestinal apical surface reveals nanobristles on microvilli. *Proc Natl Acad Sci U S A*. 119:e2122249119.

Zwaenepoel, I., A. Naba, M.M. Da Cunha, L. Del Maestro, E. Formstecher, D. Louvard, and M. Arpin. 2012. Ezrin regulates microvillus morphogenesis by promoting distinct activities of Eps8 proteins. *Molecular biology of the cell*. 23:1080-1094.